AD_____

Award Number: W81XWH-06-1-0484

TITLE: Simulations to Evaluate Accuracy and Patient Dose in Neutron-Stimulated, Emission-Computed Tomography (NSECT) for Diagnosis of Breast Cancer

PRINCIPAL INVESTIGATOR: Anuj J. Kapadia

CONTRACTING ORGANIZATION: Duke University
                                                     Durham, NC 27708

REPORT DATE: April 2008

TYPE OF REPORT: Annual Summary

PREPARED FOR: U.S. Army Medical Research and Materiel Command
                         Fort Detrick, Maryland 21702-5012

DISTRIBUTION STATEMENT: Approved for Public Release;
                                         Distribution Unlimited

REPORT DOCUMENTATION PAGE

Form Approved
OMB No. 0704-0188

Public reporting burden for this collection of information is estimated to average 1 hour per response, including the time for reviewing instructions, searching existing data sources, gathering and maintaining the data needed, and completing and reviewing this collection of information. Send comments regarding this burden estimate or any other aspect of this collection of information, including suggestions for reducing this burden to Department of Defense, Washington Headquarters Services, Directorate for Information Operations and Reports (0704-0188), 1215 Jefferson Davis Highway, Suite 1204, Arlington, VA 22202-4302. Respondents should be aware that notwithstanding any other provision of law, no person shall be subject to any penalty for failing to comply with a collection of information if it does not display a currently valid OMB control number. **PLEASE DO NOT RETURN YOUR FORM TO THE ABOVE ADDRESS.**

1. REPORT DATE 01-04-2008	2. REPORT TYPE Annual Summary	3. DATES COVERED 31 Mar 2007 – 30 Mar 2008

4. TITLE AND SUBTITLE

Simulations to Evaluate Accuracy and Patient Dose in Neutron-Stimulated, Emission-Computed Tomography (NSECT) for Diagnosis of Breast Cancer

5a. CONTRACT NUMBER

5b. GRANT NUMBER
W81XWH-06-1-0484

5c. PROGRAM ELEMENT NUMBER

6. AUTHOR(S)

Anuj J. Kapadia

Email: anuj.kapadia@duke.edu

5d. PROJECT NUMBER

5e. TASK NUMBER

5f. WORK UNIT NUMBER

7. PERFORMING ORGANIZATION NAME(S) AND ADDRESS(ES)

Duke University
Durham, NC 27708

8. PERFORMING ORGANIZATION REPORT NUMBER

9. SPONSORING / MONITORING AGENCY NAME(S) AND ADDRESS(ES)
U.S. Army Medical Research and Materiel Command
Fort Detrick, Maryland 21702-5012

10. SPONSOR/MONITOR'S ACRONYM(S)

11. SPONSOR/MONITOR'S REPORT NUMBER(S)

12. DISTRIBUTION / AVAILABILITY STATEMENT
Approved for Public Release; Distribution Unlimited

13. SUPPLEMENTARY NOTES
Original contains colored plates: ALL DTIC reproductions will be in black and white.

14. ABSTRACT We are developing a tomographic technique called Neutron Stimulated Emission Computed Tomography (NSECT) for early detection of breast cancer. NSECT is sensitive to metabolic changes in trace element concentrations that are seen in tumors at very early stages of development. Detecting and measuring these element concentrations has the potential to detect breast cancer very early. Using neutrons as the imaging radiation leads to significant concerns about patient dose due to their higher weighting factor. While preliminary experiments show that it is possible to perform NSECT scans with patient dose comparable to mammography, one of the key aspects of successful clinical translation is to deliver the minimum dose possible. This project aims at evaluating the effects of NSECT dose-reduction techniques on the accuracy of detecting breast cancer. Four dose-reduction techniques are under evaluation: reducing neutron flux; reducing spatial projections; reducing angular positions; and using multiple detectors. As separate evaluation of each factor using experimental studies is prohibitively time consuming, these evaluations are performed using Monte-Carlo simulations as a feasible alternative. In the first year of the study, we developed a Monte Carlo simulation of the NSECT tomographic scanning system in GEANT4 along with phantoms of benign and malignant breast tissue. The simulated system has now been used to generate simulated data from NSECT scans of the benign and malignant breast. The simulations have been tested and validated against experimentally acquired data from several different types of phantoms. Tomographic images are reconstructed using a maximum-likelihood algorithm, which has been used to generate diagnostic images of a single-element disease model based on iron distribution. These results demonstrate that NSECT has the ability to detect cancer-marking elements in the breast at reasonable levels of patient dose. Work is now underway to determine the efficacy of the system in differentiation benign and malignant tissue and analyzing the effects of dose-reduction techniques on system accuracy.

15. SUBJECT TERMS
Neutron, spectroscopy, NSECT, breast, tomography, imaging, MLEM, Monte Carlo simulation, Geant4.

16. SECURITY CLASSIFICATION OF:			17. LIMITATION OF ABSTRACT	18. NUMBER OF PAGES	19a. NAME OF RESPONSIBLE PERSON USAMRMC
a. REPORT U	b. ABSTRACT U	c. THIS PAGE U	UU	100	19b. TELEPHONE NUMBER *(include area code)*

Standard Form 298 (Rev. 8-98)
Prescribed by ANSI Std. Z39.18

Table of Contents

INTRODUCTION

Breast cancer is the leading type of cancer to affect women all over the world. In the United States alone, breast cancer is expected to account for 32% of all new cancer cases among women. The American Cancer Society has estimated that 184,450 new cases of breast cancer will be detected in 2008, and 40,930 of these will result in death [1]. Early detection has proved to be the most effective technique to increase survival rates for this disease. Screening x-ray mammography is presently the only FDA approved screening tool for early detection of breast cancer. While it has proved to be effective, screening mammography has several limitations in trying to detect masses and spiculations in mammograms. First, it requires that the mammograms have good contrast, which is often difficult to achieve in women with dense breasts. Second, it uses an anatomic approach in trying to identify abnormalities in mammograms, making it essential that the abnormality be developed enough to show masses and calcifications clearly. This development usually comes at advanced stages of tumor growth. Finally, it has limitations in classifying detected abnormalities as benign or malignant. Several artificial intelligence tools, developed to classify detected lesions as benign or malignant have been investigated, but none have been FDA approved yet. These tools, such as computer aided diagnosis (not to be confused with the FDA approved computer aided detection systems now available), make their decisions based on morphological features such as shape, size, texture, etc. While they are fairly effective in classifying a detected lesion as benign or malignant, their dependence on analyzing an already visible lesion reduces their decision-making ability for lesions in very early stages of development.

To overcome these limitations, we are developing a technique that is sensitive to metabolic changes seen in malignant tumors during very early developmental stages. Various experiments conducted on trace elements in the human body have shown that malignant tumors exhibit changes in trace elements concentrations during early stages of development [2-7]. Quantifying these element concentrations, such as those of rubidium, cesium, aluminum and antimony, could potentially enable diagnosis of breast cancer at very early stages much before the tumor grows large enough to be detected by existing imaging techniques.

Principle

Our technique, called Neutron Stimulated Emission Computed Tomography (NSECT), uses a spectroscopic approach to analyze changes in element concentrations at molecular levels in breast tissue [8-10]. NSECT analyzes spectral information obtained from inelastic scattering between a neutron and a target atomic nucleus to identify the atom and determine its concentration in the tissue. Neutrons striking a stable atomic nucleus stimulate it to emit gamma radiation which is unique to that element. Measuring the energy and quantity of the emitted radiation allows direct determining of the emitting element concentration. Ratios of trace element concentrations detected can then be used to classify the tissue as benign or malignant. Our preliminary data suggests that this technique has great potential in developing into an effective screening tool for early diagnosis of breast cancer.

Using neutrons as the imaging radiation leads to significant concerns about patient dose. At the energies we propose, neutrons are known to damage the body 10 times more than x-rays. Reducing patient dose is a critical task in making NSECT feasible as a diagnostic technique for breast cancer. Our preliminary experiments show that it is possible to achieve an effective patient dose of about 15 mSv, which is comparable to the typical dose from an abdominal CT scan. This is possible because though individual neutrons cause more tissue damage than x-rays, it takes an immensely smaller number of neutrons to create an NSECT image, than x-rays to create a CT image. A primary objective of this project is to reduce dose further to allow NSECT to be more easily accepted as a screening tool.

Reducing patient dose in NSECT will be accompanied by a reduction in detection accuracy. This project aims at evaluating the trade-offs between patient dose and accuracy in NSECT, for 4 proposed dose-reduction techniques, and determine the minimal values of patient dose for which accuracy in the system remains high enough to effectively diagnose breast cancer.

The 4 different techniques proposed for dose-reduction in NSECT are a) neutron flux reduction, b) reduction in projection spatial sampling, c) reduction in angular sampling (fewer angles), and d) using multiple detectors. The first 3 techniques will reduce dose by reducing the amount of radiation incident on the body, while using multiple detectors will extract maximum information from the incident radiation. It is very difficult to evaluate the effects of each of these techniques individually using experimental NSECT studies, as these studies, which are at present performed in a nuclear accelerator lab, are prohibitively time consuming. We propose to approach this experiment using Monte-Carlo simulations as an alternative.

BODY

Of the proposed specific aims, tasks 1, 2 and 3 were completed in Year 1:

> **Task 1: Build a Monte Carlo simulation of the tomographic scanning system using GEANT4**
> (Months 1-10)
> **Status:** This task has been completed exactly as proposed.

> **Task 2: Build GEANT4 phantoms for benign and malignant breast tissue based on element concentrations reported in various experimental studies.** (Months 11-12)
> **Status:** This task has been completed exactly as proposed.

> **Task 3: Integrate simulations built in tasks 1 and 2 into a single module to allow simulation of a complete NSECT patient scan from patient irradiation to spectrum acquisition.** (Months 11-12)
> **Status:** This task has been completed exactly as proposed.

Progress of the tasks completed in Year 2 is described below.

Task 4: Determine element concentrations from simulated gamma spectra using spectral analysis and compare with pre-defined concentration levels in simulated phantom. Months (13-15)

Status: This task has been completed as proposed.

The breast phantom simulations built in tasks 1-3 were used to obtain quantitative estimates of the concentration differences in the benign and malignant breast. The results, described in [11] and corroborated by the experimental measurements in [9], demonstrated that with the currently available instrumentation hardware, NSECT has the detection sensitivity to identify concentration changes between benign and malignant tissue. Table 1 below shows the elemental composition of the normal and malignant breast tissue simulated in GEANT4. The corresponding gamma spectrum obtained for this sample is shown in Figure 1. As can be observed in the spectrum, statistically significant differences were observed primarily for three elements – ^{81}Br, ^{87}Rb and ^{133}Cs. While several other elements were also observed in the gamma spectra, these three elements demonstrated maximum statistical detection accuracy for identifying malignant tissue.

Figure 2 shows experimentally acquired spectra from (a) benign and (b) malignant breast tissue specimens obtained from biopsy. The three elements noted above, ^{81}Br, ^{87}Rb and ^{133}Cs, were observed to exhibit significant concentration differences between the two specimens, thereby confirming the results of the simulation experiments.

These two studies led to the publication of two manuscripts in peer-reviewed journals - references [9, 11].

	Normal (%)	Malignant (%)
Oxygen	61.429	61.429
Carbon	22.857	22.857
Hydrogen	12.649	12.510
Nitrogen	2.571	2.571
Chlorine	1.98E-2	2.15E-2
Sodium	1.85E-2	2E-2
Potassium	8.94E-2	1.96E-2
Iron	9.8E-3	7.85E-3
Calcium	8.29E-3	1.13E-2
Zinc	1.17E-3	1.14E-3
Bromine	7.07E-4	6.55E-4
Aluminum	6.67E-4	5.7E-4
Rubidium	5.98E-4	5.84E-4
Manganese	3.88E-5	3.16E-5
Cobalt	2.06E-5	1.98E-5
Cesium	3.27E-7	3.6E-7

Table 1: Breast tissue composition for normal and malignant models (from [11]). The percentages were calculated by first converting dry weights to wet weights.

Figure 1. Gamma spectrum obtained from the simulated breast samples, normal and malignant, acquired with 10 million neutron events. Statistically significant differences were observed for three elements – ^{81}Br, ^{87}Rb and ^{133}Cs. While several other elements were also observed in the gamma spectra, these three elements demonstrated maximum statistical detection accuracy. (Figure from [11]).

(a) Benign Breast   (b) Malignant Breast

Figure 2. Gamma energy spectrum from (a) benign and (b) malignant breast samples showing energy peaks for several potential elements identified. Gamma peaks are seen for ^{72}Ge and ^{74}Ge from the germanium detector. Peaks with multiple potential element matches are labeled accordingly. Statistically significant differences are observed for the three elements observed in the simulated results– ^{81}Br, ^{87}Rb and ^{133}Cs. (Figure from [9]).

6

The concentration differences observed in the breast spectra in Figures 1 and 2 show variations of microgram quantities, which require an improvement in quantification accuracy for accurate detection of malignant tumors. In order to identify the detection limit and accuracy of NSECT, a single-element disease model has been selected to allow the quantification process to be systematically performed by changing only a single variable. The disease model of choice is of iron-overload in the liver, chosen for two main reasons: (a) the disorder is characterized by changes of a single element (iron) in the diseased tissue, and (b) liver tissue has the same organ weighting factor as the breast (i.e. 0.5), thereby allowing the dose-evaluation experiments to be generally translated to the breast.

The liver model is simulated as shown in Figure 3, comprising a torso chamber, liver chamber and high iron-concentration lesions in the liver.

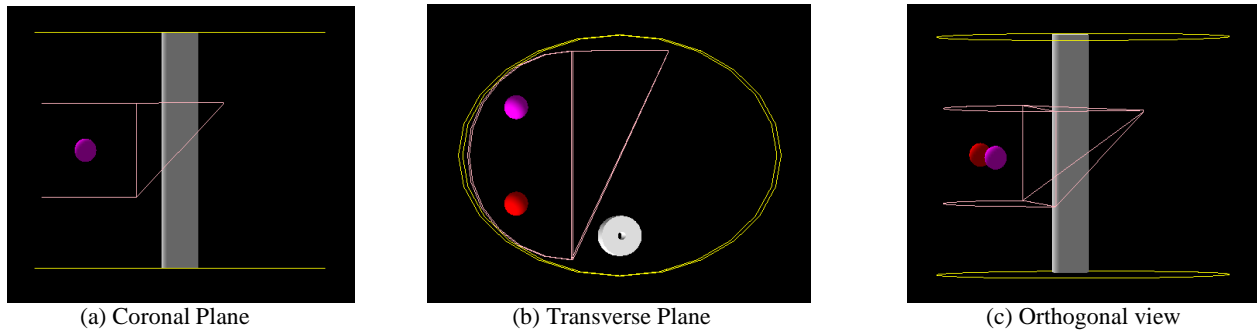| (a) Coronal Plane | (b) Transverse Plane | (c) Orthogonal view |

Figure 3. GEANT4 simulation of the liver iron overload sample. The outline of the torso is marked by the yellow lines. The liver is shown as a pink outline with two high concentration spherical lesions inside. Each lesion contains a different concentration of iron. The spine is visible as a white cylindrical tube. (Figure from [12]).

The liver phantom was scanned with the simulation developed in Tasks 1-3 to generate a spectrum from iron as shown in Figure 4 below.
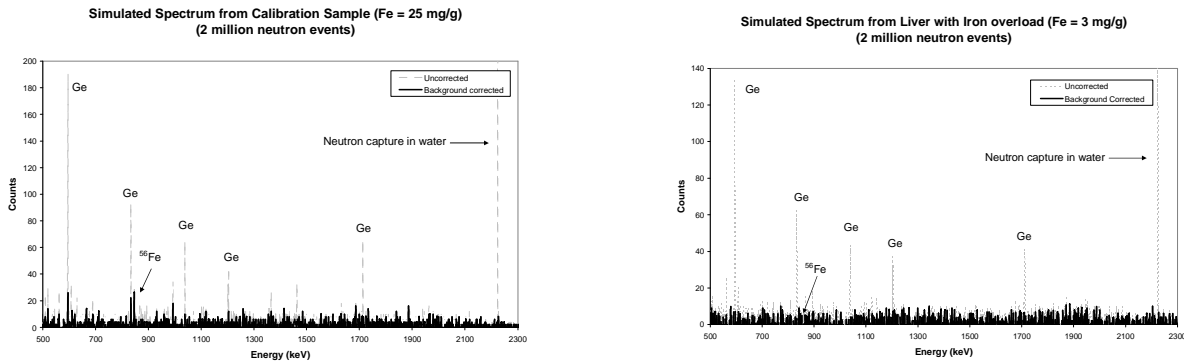

Figure 4. Simulated gamma spectrum from (a) calibration sample (Fe = 25 mg/g) and (b) liver with iron overload (Fe =3 mg/g) with background correction. The background corrected spectrum is shown as a solid black line while the original uncorrected spectrum appears as a gray dotted line. Peaks for germanium and neutron capture on hydrogen are significantly reduced through sample-out subtraction, while the signal peak from iron at 847 keV remains unchanged. (Figure from [12]).

Specialized algorithms were designed for spectral analysis and tested using experimental spectra from nuclear laboratory experiments. These algorithms were used for the following functions in spectral analysis and have been described in the references mentioned: (a) Scatter background Correction [9, 11, 13], (b) Energy peak identification [9, 11, 14], and (c) Compton Background Correction [9, 14].

The experiments performed in this task led to the publication of 4 peer-reviewed manuscripts [9, 11, 13, 15] and 3 conference proceedings [16-18].

Task 5: Reconstruct tomographic images using MLEM reconstruction algorithms. (Months 16-20)

Status: This task has been completed as proposed.

Tomographic images were generated using the liver iron overload phantom described in Task 4 and reconstructed using a maximum likelihood expectation maximization (MLEM) algorithm for emission tomography with Poisson counting [19]. Reconstructed images are shown in Figure 5 below.

(a) Simulated sample   (b) Reconstructed Image (iron)   (c) Reconstructed image (carbon)
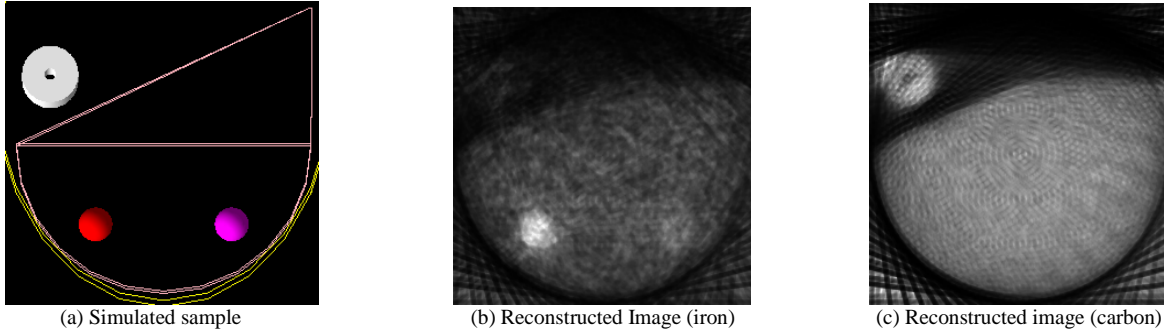
Figure 5. Comparison of the simulated liver iron overload sample with the corresponding reconstructed image for (b) iron and (c) carbon. The distribution of intensities in the reconstructed image is found to be in agreement with the distribution of iron and carbon in the original sample. (Figure from [12]).

The reconstruction algorithm was tested and validated against experimentally acquired data from a phantom of solid iron and solid copper, shown in Figure 6. The spectral acquisition in GEANT4 is shown in Figure 7.

(a) Physical Sample   (b) Simulated Sample

Figure 6. Composite iron-copper tomographic sample used for validation of the MLEM reconstruction algorithm. The sample is made up of copper (outer, vertical bars) and iron (inner, diagonal bars) arranged like the letter N. Each bar measures 6mm in thickness, 60mm in height and 24mm in depth. The sample was simulated in GEANT 4 as shown in (b). (Figure from [12]).

(a) Sample aligned at the initial position of zero degree   (b) Sample rotated clockwise through 22.5 degrees
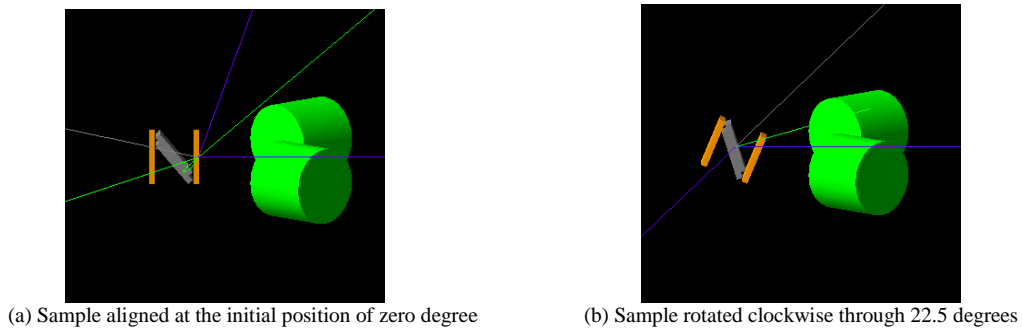
Figure 7. GEANT4 tomography simulation for the composite iron-copper tomographic sample. The two views show the sample rotated through 22.5 degrees. The orange bars correspond to copper, grey bars to iron, and the green cylinders show HPGe detectors. The blue lines correspond to incident and scattered neutrons while green lines correspond to gamma rays created through inelastic scatter. (Figure from [12]).

Figure 8 shows the corresponding images generated for the iron-copper sample. Figure 9 shows a line profile comparing the simulated and experimental data, validating the efficacy of the reconstruction algorithm.

(a) Simulated   (b) Experimental
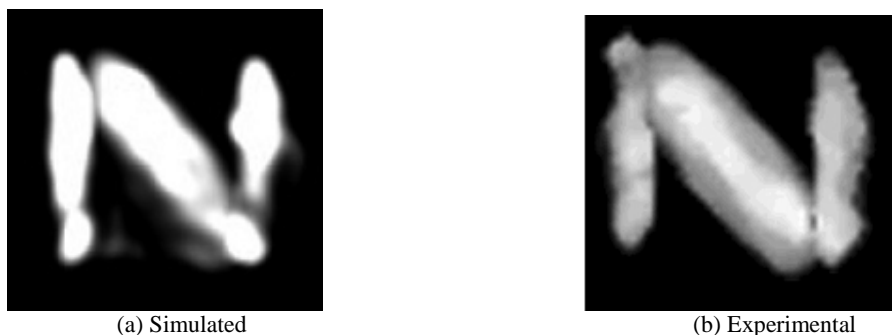
Figure 8. Reconstructed images from simulated and experimental acquisition of the iron-copper sample. (Figures from [15, 20]).
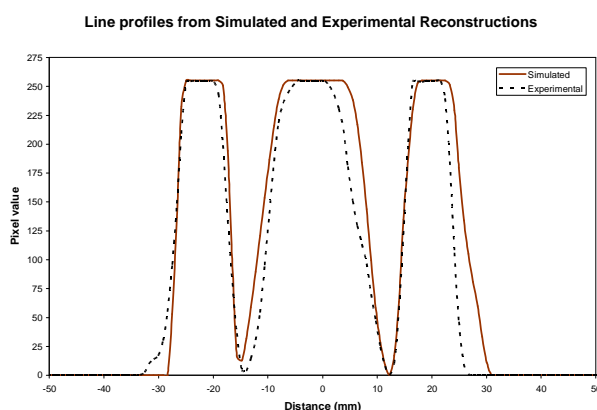

Figure 9. Line profile of the intensity distribution through the simulated and experimentally reconstructed images. At half max, the width of the left and right copper regions is seen to be 10 mm and 9 mm in the simulated image, and 9 mm and 8 mm in the experimental image. The width of iron is seen to be 18.5 mm in the simulated image and 17 mm in the experimental image. (Figure from [12]).

Task 6: Evaluate simulation performance by comparing simulated gamma spectrum for multi-element control samples with experimental data from identical real samples. (Months 21-36)
    a) Evaluate and optimize detector performance to match experimental data.
    b) Evaluate and optimize beam geometry and flux to match experimental acquisition.

Status: This task has been performed in part, and is currently under way.

The simulation developed and tested in tasks 1-5 was validated against experimentally obtained spectra from several single-element samples and multi-element samples. The different elements and the corresponding spectral images and figure numbers are listed below.
Figure 10: Thin iron sample. Figure 11: Composite sample – Fe + NaCl + KCl + H_2O. Figure 12: Mixed iron-copper sample. The experimental spectra for all samples were acquired using the neutron beam scanning facilities at the Triangle Universities Nuclear Laboratory (TUNL). All of the samples demonstrated excellent match between simulated and experimental spectra, with errors ranging from 3% to 15% for different element peaks.
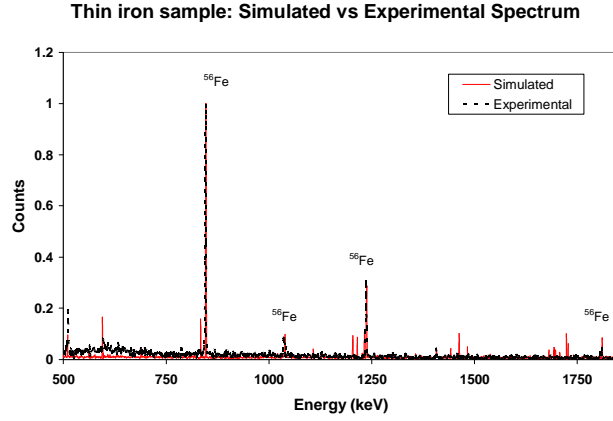
Thin iron sample: Simulated vs Experimental Spectrum

Figure 10. Comparison of simulated and experimental gamma spectrums for a natural iron sample in air. The simulated spectrum is shown as a solid red line, while the experimental spectrum is depicted by an overlaid dotted black line. Energy peaks corresponding to the 4 most prominent excited states in ^{56}Fe can be seen at 847 keV, 1039 keV, 1238 keV and 1811 keV.

Fe + NaCl + KCl solution in water: Simulated vs Experimental Spectrum
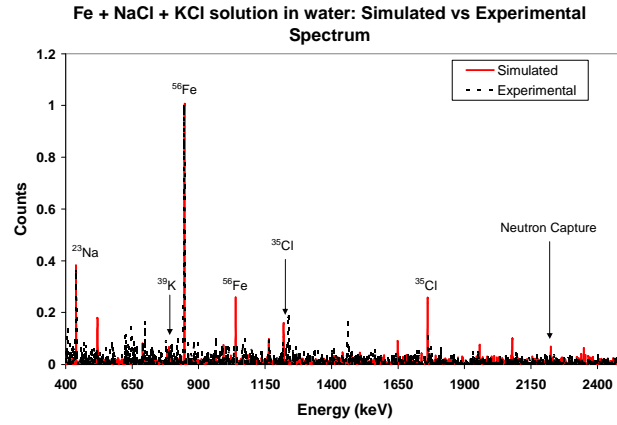

Figure 11. Comparison of simulated and experimental normalized gamma spectrums for the Fe, NaCl and KCl composite sample. The simulated spectrum is shown as a solid red line, while the experimental spectrum is depicted by an overlaid dotted black line. Energy peaks corresponding to all 4 elements are seen in the spectrums.
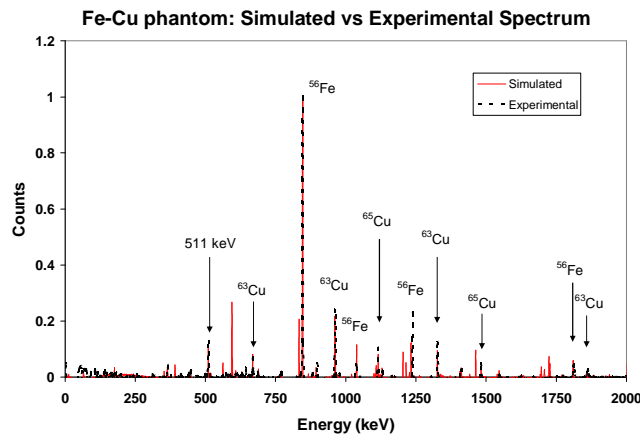
Fe-Cu phantom: Simulated vs Experimental Spectrum

Figure 12. Comparison of simulated and experimental normalized gamma spectrums for the iron-copper tomography sample. Gamma spectrums from all projections are added to form this composite spectrum. The simulated spectrum is shown as a solid red line, while the experimental spectrum is depicted by an overlaid dotted black line. Energy peaks are identified for several gamma lines in both elements.

Task 7: Evaluate patient dose from the NSECT simulation software, considering cumulative neutron and gamma effects with appropriate quality factors for particle type (neutrons/gamma) and weighting factors for tissue type (breast). (Months 21-36)

Status: This task has been performed in part and is currently under way.

A preliminary dose calculation technique has been developed and implemented to calculate the total patient dose from cumulative neutron and gamma effects. This technique has been described in [15] and has been used to calculate patient dose for breast and liver scans as shown below.

The total energy deposited in the target organ (absorbed energy) is measured using the GEANT4 simulation. The absorbed energy is then converted to absorbed dose by factoring in the volume, mass and density of the organ. The absorbed dose is then converted to an equivalent dose by taking into account the radiation weighting factor for neutrons (10) and the organ weighting factor for the breast and liver (0.5 for both). An example of dose calculation from [15] is shown in Table 2 below. For each of these experiments, the observed doses for liver and breast scans were well below 1 mSv.

	Breast	Liver
Energy absorbed = number of neutrons $\times$ energy deposited	1×10^6 neutrons $\times$ 3.74 MeV/ neutron $\times$ 1.6×10^{-13} J MeV^{-1} = **5.98×10^{-7} J**	1×10^6 neutrons $\times$ 5.38 MeV/ neutron $*$ 1.6×10^{-13} J MeV^{-1} = **8.61×10^{-7} J**
Exposure volume	10 cm^3	30 cm^3
Density	1.2 g cm^{-3}	1.2 g cm^{-3}
Mass	0.012 kg	0.036 kg
Absorbed dose = energy absorbed per kg of exposed tissue	5.98×10^{-7} J/0.012 kg = **4.98×10^{-5} Gray (J kg^{-1})**	8.61×10^{-7} J/0.036 kg = **2.39×10^{-5} Gray (J kg^{-1})**
Equivalent dose = Absorbed Dose $\times$ particle weighting factor	4.98×10^{-5} Gray $\times$ 10 = **0.498 mSv**	2.39×10^{-5} Gray $\times$ 10 = **0.239 mSv**

Table 2. Dose calculation for breast and liver scans (from [15]).

Task 8: Evaluate efficacy of the system in differentiating benign and malignant tissue through ROC analysis. (Months 24-36)
Status: This task is currently under way.

Task 9: Investigate trade-offs between accuracy and patient dose for NSECT dose-reduction techniques. (Months 26-36)
Status: This task is currently under way.

KEY RESEARCH ACCOMPLISHMENTS

- The entire NSECT acquisition system has been simulated using the Geant4 environment, which makes it possible to continue system evaluation and development without requiring a neutron beam. The simulation includes gamma detectors, phantoms for benign and malignant breast tissue, and phantoms for liver iron overload.
- Spectral data has been obtained from benign and malignant breast biopsy specimens as well as from several single-element and multi-element control phantoms for validation of the Geant4 simulations.
- The GEANT4 simulation has been tested and validated against experimental data and is now ready to be used for further breast specimen evaluations.
- A reconstruction algorithm has been designed, tested and verified against experimental spectral data, and has been used to generate tomographic images of the liver iron-overload phantom.

REPORTABLE OUTCOMES

The following conference proceedings and manuscripts have been attached in the appendix section.

1. Floyd CE, Sharma AC, Bender JE, **Kapadia AJ**, Xia JQ, Harrawood BP, Tourassi GD, Lo JY, Kiser MR, Crowell AS, Pedroni RS, Macri RA, Tajima S, and Howell CR, "Neutron Stimulated Emission Computed Tomography: Background Corrections," *Nuclear Instruments and Methods in Physics Research Section B*, vol. 254, pp. 329 - 336, 2007.

2. Sharma AC, Harrawood BP, Bender JE, Tourassi GD, **Kapadia AJ**, "Neutron Stimulated Emission Computed Tomography: a Monte Carlo simulation approach," *Physics in Medicine and Biology*, vol. 52, pp. 6117-31, 2007.
(Featured in "*Physics in Medicine and Biology Highlights of 2007*")

3. Bender JE, **Kapadia AJ**, Sharma AC, Tourassi GD, Harrawood BP, and Floyd CE, "Breast cancer detection using Neutron Stimulated Emission Computed Tomography: prominent elements and dose requirements," *Medical Physics,* vol. 34, pp. 3866-3871, 2007.

4. **Kapadia AJ**, Harrawood BP, Tourassi GD, " A Geant4 Simulation for Iron Overload Detection using NSECT," *Proceedings of IEEE Nuclear Science Symposium, Medical Imaging Conference 2007,* vol. 6, pp 4604–4607.

5. **Kapadia AJ**, Sharma AC, Bender JE, Tourassi GD, Howell CR, Crowell AS, Kiser MR, Harrawood BP, Pedroni RS, and Floyd CE, "Neutron Stimulated Emission Computed Tomography for Diagnosis of Breast Cancer," *IEEE Transactions on Nuclear Science*, vol. 55(1), pp .501 – 509, 2008.

6. Floyd CE, **Kapadia AJ**, Bender JE, Sharma AC, Xia JQ, Harrawood BP, Tourassi GD, Lo JY, Crowell AS, and Howell CR, "Neutron Stimulated Emission Computed Tomography of a Multi-Element Phantom," *Physics in Medicine and Biology*, vol 53. pp 2313-2326, 2008.

7. **Kapadia AJ**, Tourassi GD, Sharma AC, Crowell AS, Kiser MR, Howell CR, "Experimental detection of iron overload in liver through neutron stimulated emission spectroscopy," *Physics in Medicine and Biology,* vol 53, pp 2633-2649, 2008.

8. **Kapadia AJ**, Harrawood BP, Tourassi GD, "GEANT4 simulation of NSECT for detection of iron overload in the liver," *Proceedings of the 2008 SPIE Symposium on Medical Imaging*, vol. 6913, pp. 691309.

9. **Kapadia AJ**, Harrawood BP, Tourassi GD, "Validation of a GEANT4 simulation of neutron stimulated emission computed tomography," *Proceedings of the 2008 SPIE Symposium on Medical Imaging,* vol. 6913, pp. 69133H.

CONCLUSION

We have simulated the NSECT acquisition system using the Geant4 Monte Carlo simulation environment, tested and validated it against experimental data, and demonstrated the efficacy of the simulation in a biological application for detection of iron in the liver. The simulation tool will allow further development and system evaluation using easily accessible computing resources. Focus is now being centered on improving quantification accuracy for breast cancer detection and on evaluating the trade-off between accuracy as patient dose is reduced.

REFERENCES

[1]   ACS, "Cancer Facts and Figures 2008," American Cancer Society, Atlanta 2008.

[2]   A. Garg, V. Singh, et al., "An elemental correlation study in cancerous and normal breast tissue with successive clinical stages by neutron activation analysis," *Biological Trace Element Research,* vol. 46, pp. 185-202, 1994 1994.

[3]   H. Mussalo-Rauhamaa, S. Piepponen, J. Lehto, R. Kauppila, and O. Auvinen, "Cu, Zn, Se and Mg concentrations in breast fat of Finnish breast cancer patients and healthy controls," *Trace Elements in Medicine,* vol. 10, pp. 13-15, 1993.

[4]   K.-H. Ng, D. Bradley, and L.-M. Looi, "Elevated trace element concentrations in malignant breast tissues," *British Journal of Radiology,* vol. 70, pp. 375-382, 1997.

[5]   K.-H. Ng, S.-H. Ong, D. A. Bradley, and L.-M. Looi, "Discriminant analysis of normal and malignant breast tissue based upon INAA investigation of elemental concentration," *Appl. Radiat. Isot.,* vol. 48, pp. 105-109, 1997.

[6]   S. Rizk and H. Sky-Peck, "Comparison between concentrations of trace elements in normal and neoplastic human breast tissue," *Cancer Research,* vol. 44, pp. 5390-5394, 1984.

[7]   M. Yaman, D. Atici, S. Bakirdere, and I. Akdeniz, "Comparison of trace metal concentrations in malign and benign human prostate," *J. Med. Chem.,* vol. 48, pp. 630-634, 2005.

[8]   C. E. Floyd, J. E. Bender, A. C. Sharma, A. J. Kapadia, J. Q. Xia, B. P. Harrawood, G. D. Tourassi, J. Y. Lo, A. S. Crowell, and C. R. Howell, "Introduction to neutron stimulated emission computed tomography," *Physics in Medicine and Biology,* vol. 51, pp. 3375-3390, 2006

[9]   A. J. Kapadia, A. C. Sharma, J. E. Bender, G. D. Tourassi, C. R. Howell, A. S. Crowell, M. R. Kiser, B. P. Harrawood, and C. E. Floyd, "Neutron Stimulated Emission Computed Tomography for Diagnosis of Breast Cancer," *IEEE Trans Nuc Sci,* vol. 55, pp. 501 - 509, 2008.

[10]   A. J. Kapadia, A. C. Sharma, G. D. Tourassi, J. E. Bender, A. S. Crowell, M. R. Kiser, C. R. Howell, and C. E. Floyd, "Neutron Stimulated Emission Computed Tomography (NSECT) for Early Detection of Breast Cancer," in *IEEE Nuclear Science Symposium, Medical Imaging Conference*, San Diego, CA, 2006, pp. 3928-3931.

[11]   J. E. Bender, A. J. Kapadia, A. C. Sharma, G. D. Tourassi, B. P. Harrawood, and C. E. Floyd, "Breast cancer detection using Neutron Stimulated Emission Computed Tomography: prominent elements and dose requirements," *Med Phys,* vol. 34, pp. 3866-3871, 2007.

[12]   A. J. Kapadia, "Accuracy and Patient Dose in Neutron Stimulated Emission Computed Tomography for Diagnosis of Liver Iron Overload: Simulations in GEANT4," in *Biomedical Engineering*. vol. PhD Durham, NC: Duke University, 2007.

[13]   C. E. Floyd, A. C. Sharma, J. E. Bender, A. J. Kapadia, J. Q. Xia, B. P. Harrawood, G. D. Tourassi, J. Y. Lo, M. R. Kiser, A. S. Crowell, R. S. Pedroni, R. A. Macri, S. Tajima, and C. R. Howell, "Neutron Stimulated Emission Computed Tomography: Background Corrections," *Nuclear Instruments and Methods in Physics Research Section B,* vol. 254, pp. 329 - 336, 2007.

[14]   A. J. Kapadia, G. D. Tourassi, A. C. Sharma, A. S. Crowell, M. R. Kiser, and C. R. Howell, "Experimental detection of iron overload in liver through neutron stimulated emission spectroscopy," *Phys Med Biol,* vol. 53, pp. 2633-2649, 2008.

[15]   A. C. Sharma, B. P. Harrawood, J. E. Bender, G. D. Tourassi, and A. J. Kapadia, "Neutron stimulated emission computed tomography: a Monte Carlo simulation approach," *Phys Med Biol,* vol. 52, pp. 6117-31, Oct 21 2007.

[16]   A. J. Kapadia, B. P. Harrawood, and G. D. Tourassi, "Validation of a GEANT4 simulation of neutron stimulated emission computed tomography," in *SPIE Symposium on Medical Imaging*, San Diego, CA, 2008, p. 69133H.

[17]   A. J. Kapadia, B. P. Harrawood, and G. D. Tourassi, "GEANT4 simulation of NSECT for detection of iron overload in the liver," in *SPIE Symposium on Medical Imaging*, San Diego, CA, 2008, p. 691309.

[18] A. J. Kapadia, A. C. Sharma, B. P. Harrawood, and G. D. Tourassi, "GEANT4 simulation of an NSECT system for iron overload detection," in *IEEE Nuclear Science Symposium, Medical Imaging Conference*, Honolulu, HI, 2007, pp. 4604 - 4607.

[19] K. Lange and R. Carson, "EM reconstruction Algorithms for Emission and Transmission Tomography," *Journal of Computer Assisted Tomography,* vol. 8, pp. 306-316, 1984.

[20] C. E. Floyd, A. J. Kapadia, J. E. Bender, A. C. Sharma, J. Q. Xia, B. P. Harrawood, G. D. Tourassi, J. Y. Lo, A. S. Crowell, M. R. Kiser, and C. R. Howell, "Neutron Stimulated Emission Computed Tomography of a Multi-Element Phantom," *Phys Med Biol,* vol. 53, pp. 2313-2326, 2008.

Neutron stimulated emission computed tomography: Background corrections

Carey E. Floyd Jr. [a,b,c], Amy C. Sharma [a,b,*], Janelle E. Bender [a,b], Anuj J. Kapadia [a,b], Jessie Q. Xia [a,b], Brian P. Harrawood [b], Georgia D. Tourassi [b], Joseph Y. Lo [a,b,c], Matthew R. Kiser [d], Alexander S. Crowell [d], Ronald S. Pedroni [e], Robert A. Macri [g], Shigeyuki Tajima [f], Calvin R. Howell [c,d]

[a] *Department of Biomedical Engineering, Duke University, Durham, NC 27708, United States*
[b] *Duke Advanced Imaging Laboratories, Department of Radiology, Duke University, Durham, NC 27708, United States*
[c] *Medical Physics Graduate Program, Duke University, Durham, NC 27708, United States*
[d] *Department of Physics and Triangle Universities Nuclear Laboratory, Duke University, Durham, NC 27708, United States*
[e] *North Carolina A&T State University, Greensboro, NC, United States*
[f] *Department of Physics, University of Virginia, Charlottesville, VA, United States*
[g] *Lawrence Livermore National Laboratory, Livermore, CA, United States*

Received 25 August 2006; received in revised form 8 November 2006
Available online 12 January 2007

Abstract

Neutron stimulated emission computed tomography (NSECT) is an imaging technique that provides an in-vivo tomographic spectroscopic image of the distribution of elements in a body. To achieve this, a neutron beam illuminates the body. Nuclei in the body along the path of the beam are stimulated by inelastic scattering of the neutrons in the beam and emit characteristic gamma photons whose unique energy identifies the element. The emitted gammas are collected in a spectrometer and form a projection intensity for each spectral line at the projection orientation of the neutron beam. Rotating and translating either the body or the beam will allow a tomographic projection set to be acquired. Images are reconstructed to represent the spatial distribution of elements in the body. Critical to this process is the appropriate removal of background gamma events from the spectrum. Here we demonstrate the equivalence of two background correction techniques and discuss the appropriate application of each.
© 2006 Elsevier B.V. All rights reserved.

PACS: 82.80; 87.57; 87.64.−t; 25.40.−Fg

Keywords: Neutrons; Gamma-ray spectroscopy; Background corrections; Image quality; Biomedical imaging

1. Introduction

This Section will describe the physical concepts behind NSECT, followed by a description of the problem posed by the unwanted detection of background gamma events. Section 2 will describe two techniques for estimating and reducing this background. Section 3 will show spectra to illustrate the effect of implementing these techniques. Section 4 will present a comparison of the two background correction techniques along with suggestions for where each would be appropriate to use.

1.1. Physical concepts of NSECT

In previous papers, we have introduced neutron stimulated emission computed tomography (NSECT) as a new

---

* Corresponding author. Address: DAILabs, 2424 Erwin Rd, Suite 302, Durham, NC 27705, United States. Tel.: +1 919 684 1440; fax: +1 919 684 1491.
 E-mail address: anc4@duke.edu (A.C. Sharma).

approach for biological spectroscopy and imaging [1,2]. NSECT provides spectroscopy by stimulating nuclei in the sample by inelastic scattering of fast neutrons. The stimulated nuclei emit characteristic gamma rays that are collected in a gamma spectrometer. Each neutron beam position defines a line of integration of the emitted gammas that are associated with known elements. By translating and rotating the beam with respect to the body, a set of tomographic projections is obtained. These projections are reconstructed for each element that is acquired in the spectrum to provide a spatial map of the elements in the body.

While similar in concept to gamma emission computed tomography (ECT), NSECT does not image radioactive pharmaceuticals but instead stimulates the emission of gammas from stable isotopes. NSECT requires different performance from the imaging technology than ECT. For all elements of interest, the emitted gammas have energies ranging from less then 300 keV to greater than 6000 keV. These energies are higher than those typically used in nuclear medicine and thus standard gamma cameras with lead collimation cannot provide sufficient energy or spatial resolution. In addition, the detection efficiency of these gamma cameras is too low for efficient imaging. For these reasons, we chose to use high purity germanium (HPGe) detectors that have excellent energy resolution within the NSECT range. HPGe detectors with sufficient detection efficiency do not report spatial information and so the spatial position of a single projection path is defined by the neutron beam position.

1.2. Unwanted background

Background events in the detected spectra introduce errors in the quantitative accuracy of the detected number of gamma photons acquired from the scattering sample. This results in an error in the estimation of the concentration of the elements in the reconstructed volumes. The background radiation is non-uniform over the energy spectrum and thus cannot be corrected by a simple offset. There are several potential sources of background in these experiments: beam uncorrelated photons, beam correlated events and detector dependent background.

Beam uncorrelated photons will be from the decay of radioactive materials in the detector area. These materials may be naturally radioactive (such as ^{40}K) or may have become radioactive with a long half-life from extensive exposure to a particle beam (such as metal in the beam transport system and the deuterium gas cell). Photon events from these sources will be random in time and somewhat continuous.

Beam correlated events consists of short half-life radioactive materials, scattered photons and photons emitted from slow neutron capture. Photons emitted by materials that have become radioactive from exposure to the beam but which have short half-lives will be correlated with the beam flux itself. Many times, gamma photons created

through inelastic scattering of neutrons in the sample are emitted along a path that initially does not intersect with the detector. These gammas can scatter off of some object in the experimental target area and arrive in the detector. These events will be offset in arrival time from those events where the gamma travels directly to the detector. While the neutrons used in these experiments are fast with energies of several MeV, many of these fast neutrons will scatter from light materials such as protons in plastics and water and thus become moderated down to thermal energies after many collisions. The gammas emitted from slow neutron capture reactions can have energies of many MeV and thus can contribute to background over the entire energy spectrum. One example is the capture of thermal neutrons by ^{23}Na such as is found in NaI detectors. The ^{23}Na nucleus captures a neutron to become ^{24}Na which is unstable and decays by emitting 1.4 and 2.8 MeV gamma photons. This will contribute a large background in NaI detectors if they are used in the presence of thermal neutrons. The thermal neutron flux is correlated with the beam.

Detector dependant background comes in two forms. The first appears as discrete lines in the spectrum. These are caused when a photon with greater than 1022 keV of energy creates an electron–positron pair in the detector and one or both of these products escapes from the detector. Since each carries 511 keV of energy, these events appear as spectral lines that are displaced by 511 keV for a single escape and 1022 keV for a double escape. The second appears as a continuous background that increases at the lower energy region of the spectrum. This is due to photons that Compton scatter in the detector and then either the photon or the scattered electron escape. Since the energy transferred in a Compton collision is a continuous distribution, the offset due to these events is continuous also. Every source of photons will contribute some of this background to the energy channels below it and so the effect compounds at lower energy channels.

In summary, backgrounds can be considered to be of three classes: beam-uncorrelated photons (long half-life radioactive decay), beam-correlated events (short half-life radioactive decay, scattered, slow capture) and detector dependant events (electron escape, Compton scatter). In this work, we consider two techniques for estimating and compensating for these backgrounds. Each technique is sensitive to all classes of backgrounds.

2. Methods

The methods for NSECT data acquisition have been described previously [1,2] and only a brief overview will be presented here. For these experiments, a square pulsed beam, 7 mm on each side, of 7.5 MeV neutrons were produced from a pulsed beam of deuterons through the 2H(d,n)3He reaction. The deuterium target was a 5 cm long gas cell containing 100 psig of deuterium gas. The neutrons passed through the end of the gas cell and through a copper channel collimator that passed through

a 2 m thick shield wall. The wall shielded the detectors from the large flux of gammas produced in the 2H(d,n)3He reaction. The pulsed, collimated neutron beam emerged from the collimator to illuminate the scattering sample. Those nuclei along the neutron beam path in the scattering sample which interacted inelastically with the incident neutrons emitted characteristic gamma photons which were detected in HPGe detectors positioned at 135 deg on either side of the neutron beam and at a distance of 20 cm from the center of the scattering sample. These detectors were equipped with anti-Compton shields composed of BGO and NaI scintillators coupled to photomultiplier tubes. If a gamma were to Compton scatter in the primary detector and be captured in the shield, the coincidence of the two events would cause the event in the HPGe detector to be rejected. The HPGe detectors respond to gammas by producing a current pulse that is proportional to the energy of the detected photon. These signals were digitized and stored in the acquisition computer event by event along with the time of flight (TOF) for the event. This list-mode storage allowed the timing windows to be adjusted off line to optimize the acquisition after the experiment. To measure the TOF, the pulses in the deuteron beam were detected just before the gas cell and were used to start a clock to time the flight of the neutrons from the gas cell to the scattering sample along with the time of flight of the emitted gammas to the spectrometer. The energy gain of the detectors was calibrated using radioactive sources with known energy levels: ^{137}Cs and ^{22}Na. Gain and analog-to-digital-converter (ADC) ranges were set to give about 1 keV per channel and the exact calibration was calculated from the spectral channels of the calibration peaks. While NSECT has the capability to identify elements that produce gamma radiation between 300 and 6000 keV, the gamma emissions investigated in this study had energies below 2000 keV. Thus, the calibration of the detectors with ^{22}Na and ^{137}Cs was adequate for this experiment.

The iron samples used in these experiments were in the form of a rectangular solid 6 mm thick, 30 mm wide, and 60 mm tall. All were of natural density.

Two background correction techniques are evaluated herein. In the first, a Sample-In spectrum was acquired with the scattering sample in the neutron beam. The sample was then removed from the beam and an additional Sample-Out spectrum was acquired. To correct for background the two spectra are normalized to the same incident neutron flux and the Sample-Out spectrum is subtracted from the Sample-In spectrum to produce a background-corrected spectrum. In the second technique, TOF is used to restrict the spectrum of useable photon incident events to a window of time (True acceptance window) for which the arrival of the photon is consistent with the required time of flight for the neutron to reach the sample and for the emitted photon to reach the detector. This leaves some background in the form of photons from random sources whose time of arrival accidentally corresponds to the True acceptance window. This background is estimated by mea-

suring incident events in a window of the same time length but outside the True acceptance window time. The events in such a window correspond to the amount of background that would have occurred in the True acceptance window. These are subtracted to achieve a background corrected spectrum. In Section 3, spectra are shown that correspond to these different background estimates and to the different correction techniques.

3. Results

The first background radiation to consider is due to naturally radioactive materials in the detector region. Fig. 1 shows a spectrum acquired with sample removed and with the beam off. This spectrum was acquired overnight (about 8 h) and demonstrates the structure and magnitude of the beam uncorrelated naturally radioactive background in the region of the detector.

An example of a Sample-In, Sample-Out energy spectrum is shown in Fig. 2. The Sample-In spectra (solid line) was obtained by illuminating a phantom constructed of natural iron (94% ^{56}Fe, 6% ^{54}Fe) with a beam of 7.5 MeV neutrons. The sample was removed from the beam and the Sample-Out spectra (dashed line) was obtained by counting for an equivalent number of incident neutrons. Note the large magnitude of the background at gamma energies below 600 keV. The background measured using this technique includes beam uncorrelated photons that are emitted from naturally occurring radioactivity in the experimental area (Fig. 1) as well as beam correlated photons that are generated by the neutron beam interacting with objects other than the target and slow neutron capture. All of these sources of background would be present in a clinical imaging environment. Fig. 3 depicts the Sample-In spectra minus the Sample-Out spectra (as shown in Fig. 2).

The second form of background correction was implemented by computing the likely TOF between the production of the neutron pulse and the detection of an associated scattered photon. This is done for a known neutron velocity, distance from neutron source to sample, speed of light for the gamma and the distance from the sample to the gamma detector. The number of incident events at each time (TOF spectrum) is shown in Fig. 4. Examining the TOF spectrum, it is evident that there is a large peak between ~170 and 200 ns, the True acceptance window. There were also a number of gamma detections at times that were well outside this True time window. The gate for the True acceptance window that had believable flight times is shown as a thickened line over the peak. A gate for a False window was set for accidental photons. This gate occurs in a time region corresponding to non-physical neutron and gamma velocities and was set to an equivalent time width as that of the True acceptance window (also shown as a thickened line in Fig. 4).

The energy spectrum for events falling within the Accidental gate is shown in Fig. 5. As can be seen, there is some
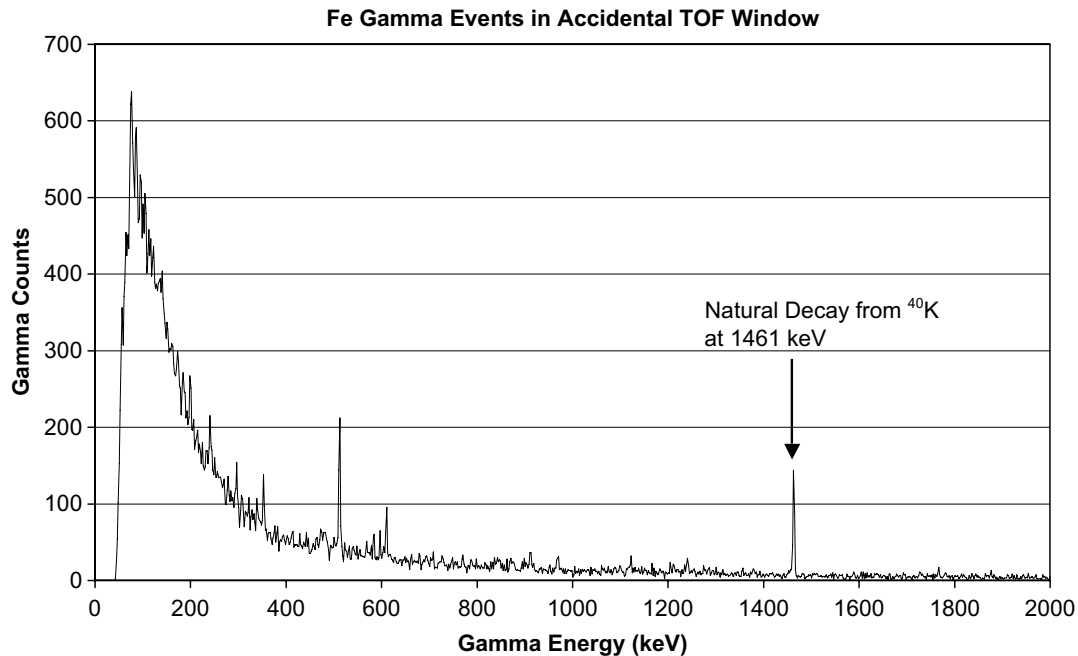
Fe Gamma Events in Accidental TOF Window

Fig. 1. Spectrum acquired with no beam and no sample to estimate the background photon incidents in the room from radioactive sources not associated with the sample. This spectrum was acquired over a time of several hours to demonstrate the shape and relative size of this background.
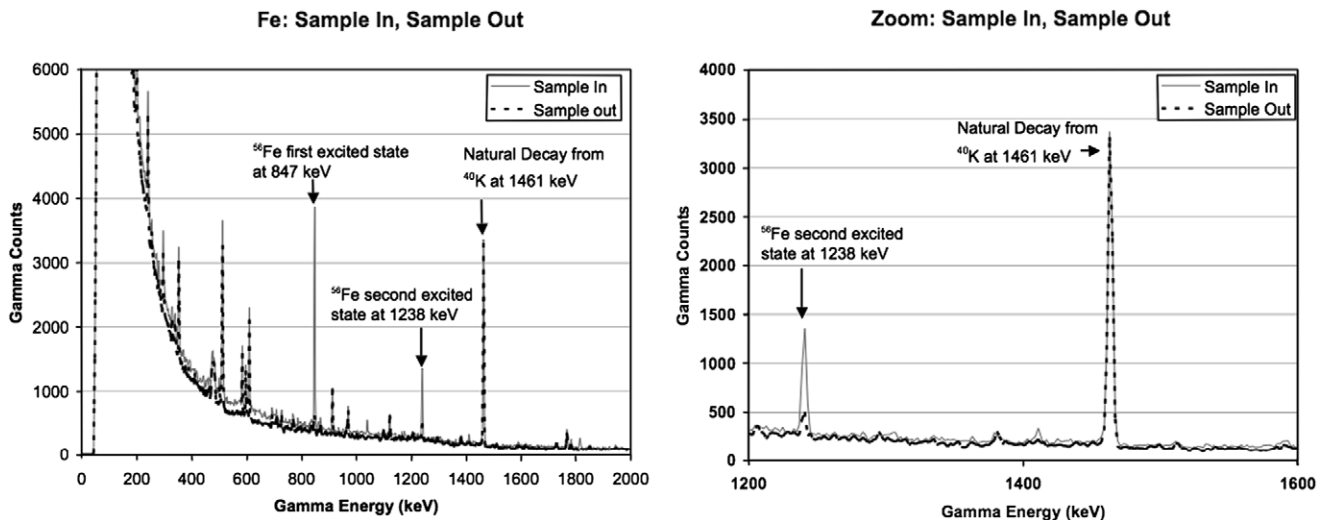

Fig. 2. Energy spectrum from iron sample. Two spectra are shown: the solid grey curve is the sample in the beam and the dashed curve is the sample removed from the beam to estimate the beam-correlated background. The left figure is a complete spectrum from 0 to 2000 keV, while the right figure zooms in on 1400–1600 keV. In the figure at right it is clear that the second excited state in ^{56}Fe is present only in the Sample-In spectrum while the natural decay line from ^{40}K is present in both spectra.

structure to the spectra. The peaks correspond to naturally radioactive gamma emissions from objects near the detector.

After the energy events corresponding to the accidental TOF window are subtracted from the energy events corresponding to the true TOF window, the corrected energy spectrum is computed as shown in Fig. 6.

To illustrate that the TOF and sample subtraction methods are equivalent for estimating the background-free spec-

trum, Fig. 7 shows a comparison the two background estimates.

The equivalence of these techniques for estimating the background is evident from Fig. 7. The difference in the two background spectra is because the Sample-Out spectrum was acquired for a longer time and the two spectra were normalized for plotting. Subtraction of the estimated background results in the excellent energy spectrum shown in Fig. 6 where the signal to background ratio for the first
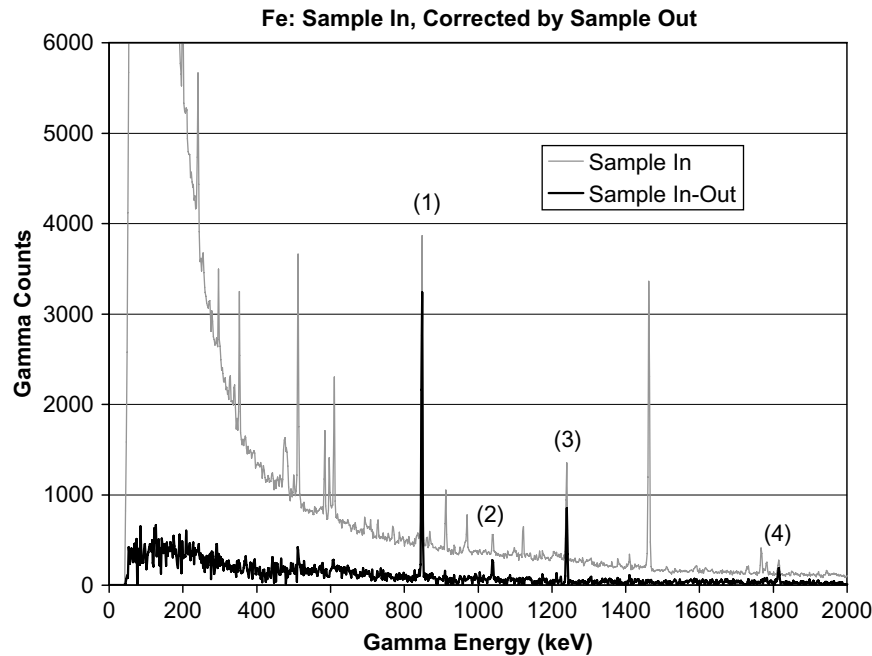
Fig. 3. Experimental spectrum from a thin iron sample. The grey line is the initial spectrum collected and the black line is the same spectrum background corrected by subtracting a Sample-Out spectrum. Four gamma peaks from ^{56}Fe are clearly identified: (1) at 847 keV is the gamma from the transition from the first excited state to the ground state; (2) at 1038 keV is the gamma from the transition from the 7th excited state at 3123 keV down to the 2nd excited state at 2085 keV; (3) at 1238 keV is the gamma from the transition from the 2nd excited state at 2085 keV down to the 1st excited state at 847 keV and (4) at 1811 keV is the gamma for the transition from the 3rd excited state at 2658 keV down to the 1st excited state at 847 keV. Note the complete removal of the background gammas from the decay of ^{40}K at 1461 keV.
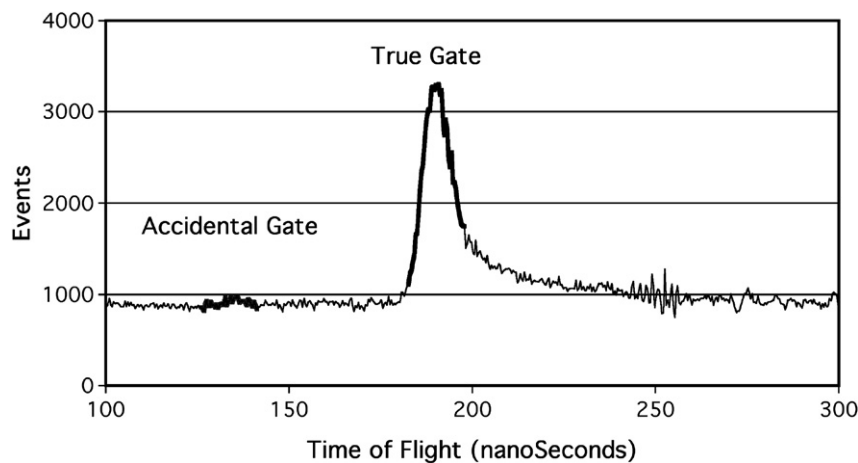

Fig. 4. Time of flight (TOF) spectrum showing a peak for gamma events with a time window correlated with the neutron beam pulse (True Gate) and time window set for non-physical flight times (Accidental Gate). Events falling within the Accidental Gate are not correlated with the neutron pulse.

excited state in ^{56}Fe at 847 keV is about 33:1 compared to a ratio of only 8:1 in the uncorrected spectrum of Fig. 2.

4. Discussion

Two techniques for background correction of spectra acquired using the NSECT technique have been described and have been shown to be equivalent. The TOF technique is more convenient for laboratory experiments where acquisition geometries and parameters are changed fre-

quently and the acquisition of separate backgrounds using the Sample-Out technique would cost valuable acquisition time. The Sample-Out technique is more appropriate to the clinical environment where the acquisition geometry and parameters do not often change and could be performed at the beginning of the day in a manner similar to the way gamma camera uniformity measurements are currently performed in clinical nuclear medicine imaging divisions. Also, the additional hardware required for the TOF implementation would add considerable complexity and cost.

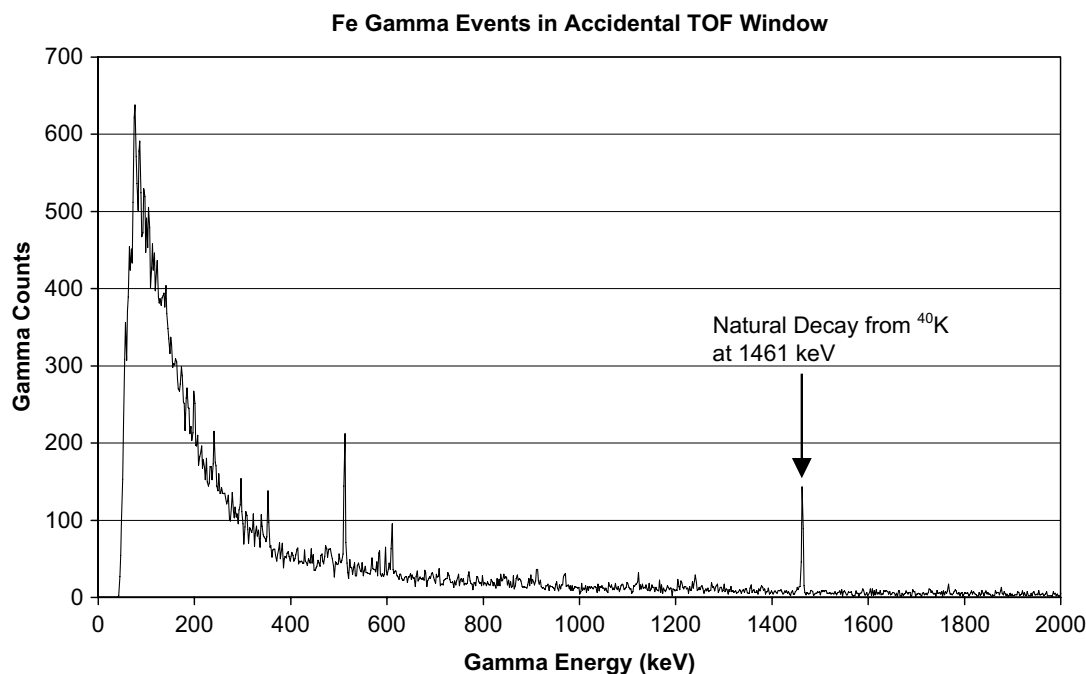**Fe Gamma Events in Accidental TOF Window**

Fig. 5. The energy spectrum for those time uncorrelated events detected within the accidental TOF gate window. The structure is due to radioactive decay of isotopes near the detector.
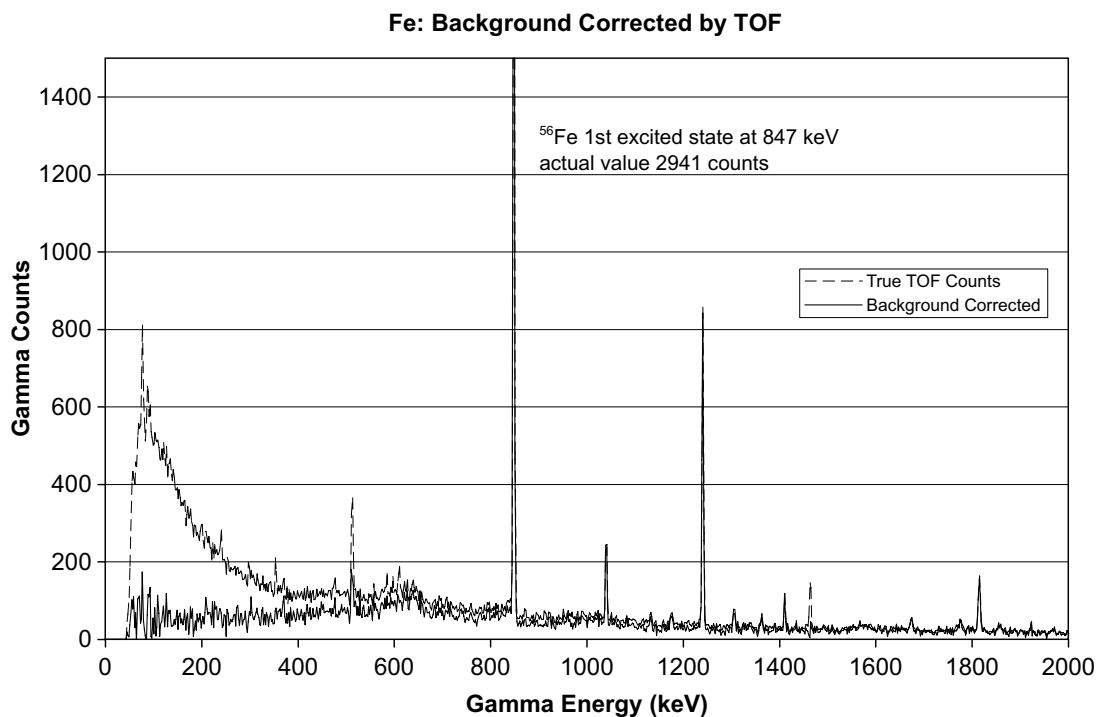
Fe: Background Corrected by TOF

Fig. 6. The energy spectra for the events arriving in the true TOF window (dashed line), and the same spectrum after background correction (solid line) resulting from subtracting the events arriving in the accidental window.

In theory, both the Sample-Out technique and the TOF technique would adequately measure beam uncorrelated background; however, measurement of beam correlated background would be different between the two techniques. The Sample-Out technique measures all events that occur while the neutron beam is firing regardless of the TOF. With the TOF windowing, events are only counted during a certain time window. Beam correlated events may change in number depending on the TOF. But, it appears that the background radiation measured by both techniques is
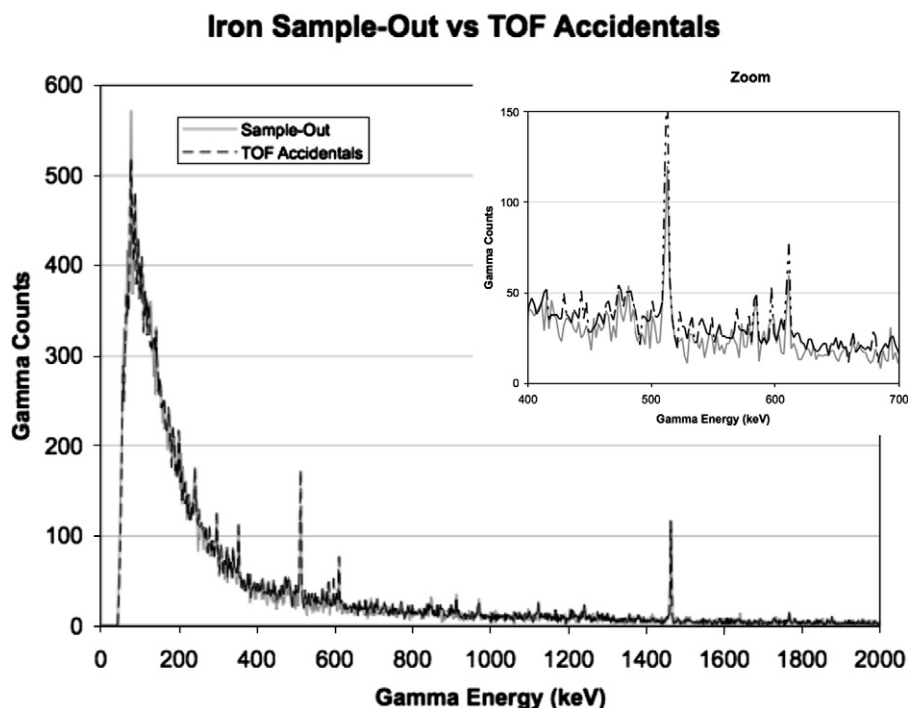
Fig. 7. A comparison of the background acquired with the sample removed (Sample-Out: Solid Line) and the background acquired as events with time of flight (TOF) in the accidental window (TOF Accidentals: dashed line). It is clear that both techniques provide equivalent estimates of the background and that either a Sample-Out measurement or a TOF technique will provide excellent background correction. The inset zooms in on counts collected in the energy range of 400–700 keV.

similar, rendering the differences insignificant. Neither technique can adequately correct for detector dependant background as both electron escape and Compton scatter increase with increased gamma photons. These increase when a sample is present during the proper TOF interval; therefore, this increase cannot be recreated without a sample. A small number of events occurring during the proper TOF with a sample present are background that cannot be filtered out regardless of technique. This is indeed a small amount of background events as both techniques greatly improve SNR.

In spectral analysis, true peaks are typically identified with a certain statistical certainty. Care must be taken to propagate the counting errors during each step in the background correction process; thereby, ensuring the accuracy of both the counting statistics and peak identification. This is achieved in software by maintaining a data set that includes both the spectral information (counts at each energy level) and its corresponding statistical uncertainty. Each time the spectral data is modified in the background correction process, its corresponding uncertainty must be updated as well. This update propagates the counting error through the entire background correction process. Enough initial data must be obtained so that the increase in counting caused by the data manipulation error does not overwhelm the benefits gained by background reduction.

NSECT has potential for a broad range of application in both medical and biological research by providing a three-dimensional map of the spatial distribution of all elements (with the exception of H and He) in a subject from one scan. There are no fundamental physical limitations to the detection sensitivity or spatial resolution of NSECT although there may be considerable technological challenges as we strive for high sensitivity at high spatial resolution.

Several potential applications for NSECT were identified in a previous work [2] including: cancer detection (based on previous work where a change in elemental concentration was associated with malignancy [3–27]), measurements of iron overload in the liver (important for thalassemia patients; sickle cell patients at risk for stroke; individuals with hemochromatosis mutations, and for other patients who receive chronic blood transfusions [28]), and small animal imaging. The demonstration of successful background reduction provided by the current work is an important fist step toward realizing each of these applications.

5. Conclusion

In conclusion, we have demonstrated excellent potential for NSECT as a spectroscopic imaging technique. Several sources of gamma backgrounds have been identified and corrections have been implemented. Corrected spectra for NSECT projection acquisition from single-element phantoms have been presented. The equivalence of the two background correction techniques demonstrates that adequate background correction can be efficiently conducted in the laboratory using the TOF technique and can be

performed effectively in the clinical setting using the Sample-Out technique.

References

[1] C.E. Floyd Jr., C.R. Howell, B.P. Harrawood, A.S. Crowell, A.J. Kapadia, R. Macri, J.Q. Xia, R. Pedroni, J.E. Bowsher, M.R. Kiser, G.D. Tourassi, W. Tornow, R. Walter, Neutron stimulated emission computed tomography of stable isotopes, Proc. SPIE 5568 (2004) 248.

[2] C.E. Floyd Jr., J.E. Bender, A.C. Sharma, A.J. Kapadia, J.Q. Xia, B.P. Harrawood, G.D. Tourassi, J.Y. Lo, A.S. Crowell, C.R. Howell, Introduction to neutron stimulated emission computed tomography, Phys. Med. Biol. 51 (2006) 3375.

[3] A. Danielsen, E. Steinnes, A study of some selected trace elements in normal and cancerous tissue by neutron activation analysis, J. Nucl. Med. 11 (6) (1970) 260.

[4] I.L. Mulay, R. Roy, B.E. Knox, N.H. Suhr, W.E. Delaney, Trace-metal analysis of cancerous and noncancerous human tissues, J. Natl. Cancer Inst. 47 (1) (1971) 1.

[5] K. Geraki, M.J. Farquharson, D.A. Bradley, Concentrations of Fe, Cu and Zn in breast tissue: a synchrotron XRF study, Phys. Med. Biol. 47 (2002) 2327.

[6] H. Mussalo-Rauhamaa, S. Piepponen, J. Lehto, R. Kauppila, O. Auvinen, Cu, Zn, Se and Mg concentrations in breast fat of Finnish breast cancer patients and healthy controls, Trace Elem. Med. 10 (1993) 13.

[7] K.-H. Ng, D. Bradley, L.-M. Looi, Elevated trace element concentrations in malignant breast tissues, Brit. J. Radiol. (1997) 375.

[8] S. Rizk, H. Sky-Peck, Comparison between concentrations of trace elements in normal and neoplastic human breast tissue, Cancer Res. 44 (1984) 5390.

[9] P. Santoliquido, H. Southwick, J. Olwin, Trace metal levels in cancer of the breast, Surg. Gynecol. Obstet. 142 (1976) 65.

[10] E.J. Margalioth, J.G. Schenker, M. Chevion, Copper and zinc levels in normal and malignant tissues, Cancer 52 (5) (1983) 868.

[11] H. Kubo, S. Hashimoto, A. Ishibashi, Simultaneous determinations of Fe, Cu, Zn, and Br concentrations in human tissue sections, Med. Phys. 3 (4) (1976) 204.

[12] P. Ghadirian, P. Maisonneuve, C. Perret, G. Kennedy, P. Boyle, D. Krewski, A. Lacroix, A case-control study of toenail selenium and cancer of the breast, colon, and prostate, Cancer Detect. Prev. 24 (4) (2000) 305.

[13] I. Kato, A.M. Dnistrian, M. Schwartz, P. Toniolo, K. Koenig, R.E. Shore, A. Zeleniuch-Jacquotte, A. Akhmedkhanov, E. Riboli, Iron intake, body iron stores and colorectal cancer risk in women: A nested case-control study, Int. J. Cancer 80 (5) (1999) 693.

[14] R.L. Nelson, F.G. Davis, E. Sutter, L.H. Sobin, J.W. Kikendall, P. Bowen, Body iron stores and risk of colonic neoplasia, J. Natl. Cancer Inst. 86 (6) (1994) 455.

[15] K.Q. Xiao, W.J. Henderson, Electron microscopy microanalysis and quantitative detection of trace elements in carcinoma of the colon [Article in Chinese: from translated abstract], Zhonghua Bing Li Xue Za Zhi 21 (3) (1992) 142.

[16] W.P. Banner, J.J. DeCosse, Q.H. Tan, M.S. Zedeck, Selective distribution of selenium in colon parallels its antitumor activity, Carcinogenesis 5 (12) (1984) 1543.

[17] G.C. Gregoriadis, N.S. Apostolidis, A.N. Romanos, T.P. Paradellis, A comparative study of trace elements in normal and cancerous colorectal tissues, Cancer 52 (3) (1983) 508.

[18] J.O. Ogunlewe, D.N. Osegbe, Zinc and cadmium concentrations in indigenous blacks with normal, hypertrophic, and malignant prostate, Cancer 63 (7) (1989) 1388.

[19] Z. Chirulescu, C. Chiriloiu, A. Suciu, R. Pirvulescu, N. Gh, Variations of zinc, calcium and magnesium in normal subjects and in patients with neoplasias, Med. Int. 25 (4) (1987) 257.

[20] Z.M. Bataineh, I.H. Bani Hani, J.R. Al-Alami, Zinc in normal and pathological human prostate gland, Saudi Med. J. 23 (2) (2002) 218.

[21] M. Brys, A.D. Nawrocka, E. Miekos, C. Zydek, M. Foksinski, A. Barecki, Krajewska, Zinc and cadmium analysis in human prostate neoplasms, Biol. Trace Elem. Res. 59 (1–3) (1997) 145.

[22] V.Y. Zaichick, T.V. Sviridova, S.V. Zaichick, Zinc in the human prostate gland: Normal, 3hyperplastic and cancerous, Int. Urol. Nephrol. 29 (5) (1997) 565.

[23] R. Wennrich, H. Dittrich, Investigations of trace elements in metastases and primary carcinoma of the prostate, Feustel Urol. Res. 17 (2) (1989) 107.

[24] I. Romics, L. Katchalova, Spectrographic determination of zinc in the tissues of adenoma and carcinoma of the prostate, Int. Urol. Nephrol. 15 (2) (1983) 171.

[25] A. Feustel, R. Wennrich, D. Steiniger, P. Klauss, Zinc and cadmium concentration in prostatic carcinoma of different histological grading in comparison to normal prostate tissue and adenofibromyomatosis (BPH), Urol. Res. 10 (6) (1982) 301.

[26] F.K. Habib, G.L. Hammond, I.R. Lee, J.B. Dawson, M.K. Mason, P.H. Smith, Y.K. Stitch Sr., A.G. Meade, E.P. Rack, A.J. Blotcky, Metal–androgen interrelationships in carcinoma and hyperplasia of the human prostate, J. Endocrinol. 71 (1) (1976) 133.

[27] E.A. Platz, K.J. Helzlsouer, S.C. Hoffman, J.S. Morris, C.K. Baskett, G.W. Comstock, Prediagnostic toenail cadmium and zinc and subsequent prostate cancer risk, Prostate 52 (4) (2002) 288.

[28] G.M. Brittenham, D.G. Badman, Noninvasive measurement of iron: Report of an NIDDK workshop, Blood 101 (1) (2003) 15.

Neutron stimulated emission computed tomography: a Monte Carlo simulation approach

A C Sharma[1,2]**, B P Harrawood**[2]**, J E Bender**[1]**, G D Tourassi**[2] **and A J Kapadia**[1,2]

[1] Department of Biomedical Engineering, Duke University, 136 Hudson Hall, Durham, NC 27708, USA
[2] Duke Advance Imaging Labs, Department of Radiology, 2424 Erwin Rd, Suite 302, Durham, NC 27705, USA

E-mail: anc4@duke.edu (A C Sharma)

Abstract

A Monte Carlo simulation has been developed for neutron stimulated emission computed tomography (NSECT) using the GEANT4 toolkit. NSECT is a new approach to biomedical imaging that allows spectral analysis of the elements present within the sample. In NSECT, a beam of high-energy neutrons interrogates a sample and the nuclei in the sample are stimulated to an excited state by inelastic scattering of the neutrons. The characteristic gammas emitted by the excited nuclei are captured in a spectrometer to form multi-energy spectra. Currently, a tomographic image is formed using a collimated neutron beam to define the line integral paths for the tomographic projections. These projection data are reconstructed to form a representation of the distribution of individual elements in the sample. To facilitate the development of this technique, a Monte Carlo simulation model has been constructed from the GEANT4 toolkit. This simulation includes modeling of the neutron beam source and collimation, the samples, the neutron interactions within the samples, the emission of characteristic gammas, and the detection of these gammas in a Germanium crystal. In addition, the model allows the absorbed radiation dose to be calculated for internal components of the sample. NSECT presents challenges not typically addressed in Monte Carlo modeling of high-energy physics applications. In order to address issues critical to the clinical development of NSECT, this paper will describe the GEANT4 simulation environment and three separate simulations performed to accomplish three specific aims. First, comparison of a simulation to a tomographic experiment will verify the accuracy of both the gamma energy spectra produced and the positioning of the beam relative to the sample. Second, parametric analysis of simulations performed with different user-defined variables will determine the best way to effectively model low energy neutrons in tissue, which is a concern with the high hydrogen content in biological tissue. Third, determination of

the energy absorbed in tissue during neutron interrogation in order to estimate the dose. Results from these three simulation experiments demonstrate that GEANT4 is an effective simulation platform that can be used to facilitate the future development and optimization of NSECT.

1. Introduction

This paper describes the use of the GEANT4 (Agostinelli *et al* 2003) toolkit to develop Monte Carlo simulations of a new, non-destructive, spectroscopic imaging technique, neutron stimulated emission computed tomography (NSECT) (Floyd *et al* 2004, 2006, 2007, Kapadia 2007). NSECT uses a beam of high-energy neutrons (2–10 MeV) to stimulate the nuclei of the elements within a sample. Through inelastic scatter, these nuclei are excited and then decay rapidly, each emitting their own characteristic gamma ray. Analysis of the emitted gamma spectrum allows identification of the elements within the sample. Elemental concentration images can be reconstructed by collecting separate gamma spectra from multiple neutron interrogation lines within the sample. This tomographic method is similar to first-generation CT techniques (Kapadia 2007).

The logistics of securing a neutron beam source and the time-consuming nature of performing experiments make the development of a simulation environment a desirable design methodology for NSECT. Monte Carlo computer simulations permit the modeling of nuclear interactions and offer a valuable tool for the rapid design, development and testing of NSECT materials, techniques and configurations. The GEANT4 toolkit's main design purpose is the simulation of high-energy particles interacting with matter in high energy physics applications. It was selected for NSECT Monte Carlo simulations primarily because its design encompasses NSECT's domain of interest: high-energy neutron interactions in matter. GEANT4 offers many features such as geometry visualization, adjustments to the model at runtime, and user control over tracking particles and reporting interactions. The GEANT4 toolkit is a collection of C++ class libraries and the GEANT4 Neutron Data Libraries (G4NDL) (Agostinelli *et al* 2003).

This paper will first describe the GEANT4 simulation environment created to model the NSECT spectral interrogation and imaging process. It will then describe three models developed in this environment: an 'N' phantom comprised of independent sections of iron and copper, and two biological tissue models, one of the breast and one of the liver. Finally, three simulations involving these models will be described: (i) a simulation to mimic an NSECT experiment and verify the simulation environment, (ii) a simulation to determine appropriate handling of neutron interaction with hydrogen-rich tissue and (iii) a simulation to determine energy deposited in tissue to estimate the radiation dose. These simulations will be used to address the following modeling issues: the relative motion between the beam line and the sample, the effective modeling of very low energy neutrons in tissue (where hydrogen scatter is a concern) and the measuring of energy deposited in the tissue during neutron interrogation.

2. Methods

2.1. GEANT4 environment

A GEANT4 simulation environment is established by writing C++ applications and objects that are linked with GEANT4 libraries (CERN). We have established a common GEANT4
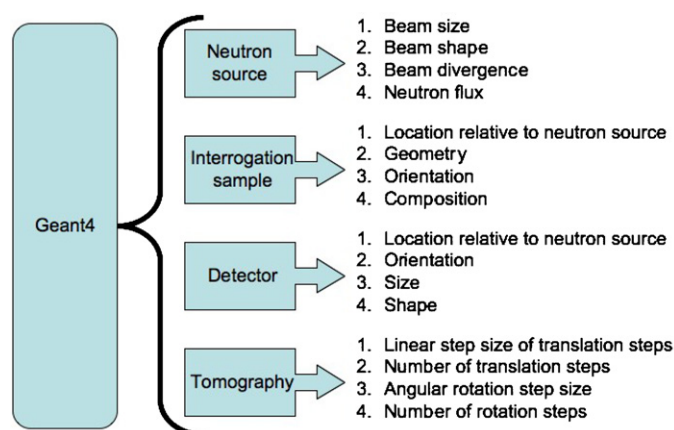
Figure 1. User-defined variables necessary to describe the experimental simulation.

C++ code base that all NSECT simulation applications utilize and build upon. This base model includes the fundamental framework of the C++ code that may be reused from one simulation to another. Additionally, the physical processes which are modeled, such as elastic and inelastic neutron scattering, are the same for each application.

A flexible framework has been built atop this base code that allows the user to simulate an NSECT experimental design. This framework includes a neutron source, a sample to be interrogated and a high purity germanium (HPGe) detector. The sample can be rotated and translated in order to simulate tomographic acquisitions. The parameters typically specified by the user are outlined in figure 1.

The first experiment described herein is a tomographic simulation. These simulations are accomplished in the following manner. All logical volumes, modeling constructs designed to hold an object or material for a model, are assigned an angle about the vertical axis and a displacement along the horizontal axis. Along with these values, step sizes are assigned so that the tomographic experiment can be implemented by specifying the integer angular step and the integer lateral step. These are specified through the Messenger class, which is a class that allows the modification of model parameters during a simulation run. To achieve tomographic reconstruction each sample can be translated through X steps at Y number of angles. These commands are input into the simulation at runtime and rebuilding is not necessary for each configuration.

Simulations involving models of biological tissue present a problem as tissue contains an abundance of hydrogen. Hydrogen nuclei have a high probability of elastically scattering with an energetic neutron. The elastic scattering depletes the neutron's energy without emitting energy in the form of photons. As initially configured, GEANT4 has no default lower energy limit on the tracking of a neutron. In hydrogen rich environments (such as a simulation of neutron interactions with biological tissue) some neutrons continue to scatter elastically with hydrogen nuclei many thousands of times until their energy becomes less than an electron volt and they are eventually captured by a nucleus or escape from the simulation world. While this is an accurate representation of the neutron's behavior, a large fraction of the simulation time is devoted to these low energy neutron events that are of little interest to NSECT research. For example, in one simulation that tracked 1 million incident neutrons, the tracking of a single neutron as it slowly lost energy scattering from hydrogen more than doubled the simulation time.
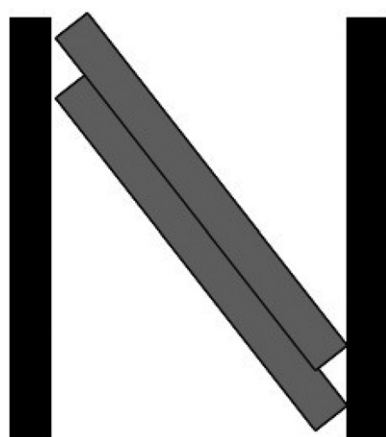
Figure 2. The '*N*' phantom made from bars of copper (black) and iron (gray).

GEANT4 includes user-defined input variables that provide a mechanism to limit the tracking of particles in any of the model's logical volumes with the logical volume's SetUserLimit method. This method allows limits to be imposed on particles tracked within the specified volume based on one of the following four parameters: track length, time, kinetic energy, or remaining range. The latter two limits are applicable only to charged particles. To limit the tracking of neutrons the GEANT4 documentation recommends the selection of a time constraint and the second experiment described herein was conducted to determine an acceptable setting for this variable (CERN).

Of note, the GEANT4 framework needs only to be compiled once. Models are built with the GEANT4 release 4.6.1 using the Gnu C++ compiler built by Apple for OSX. Environment settings are then specified as input variables at the beginning of a simulation run. All calculations present herein are performed on a Macintosh G5 class computer running the OSX operating system. Additionally, a correction was made to the G4NDL cross sectional tables for Chlorine. What should have been a numerical value in the table was incorrectly published as 'not a number' (NaN). This is a known problem with the table and we followed the GEANT4 online user forum's suggestions (CERN 2007) and replaced the 'NaN' with a value of 0.0 that is consistent with neighboring values.

2.2. Experimental model environments

Three experimental models were developed for use in simulating various NSECT experiments: an 'N' phantom made of copper and iron, a biological model of the breast and a biological model of the liver. For all experiments described below the HPGe detector is modeled as a solid cylinder of germanium, 8 cm in diameter and 10 cm long.

2.2.1. The 'N' phantom environment. The 'N' phantom application is designed to simulate the experimental conditions used to tomographically image a multi-element phantom with NSECT (Kapadia 2007). The simulated 'N' phantom is modeled as four rectangular solids corresponding to the four bars used in the physical phantom. Each rectangle is 0.3 cm thick, 6.0 cm long and 2.5 cm wide. The four bars are arranged into the shape of the letter 'N' as shown in figure 2. The two upright legs are constructed of copper, and the diagonal legs are constructed of iron. Both elements are modeled in their naturally occurring isotopic ratio.
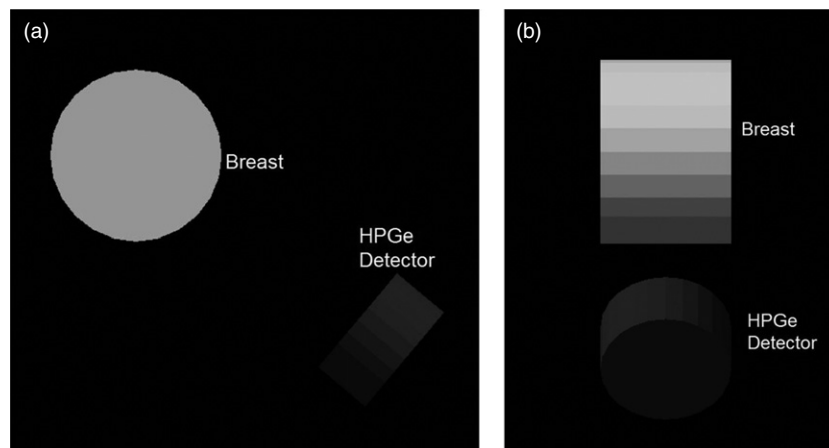
Figure 3. View 1 (a) and view 2 (b) of the breast phantom.
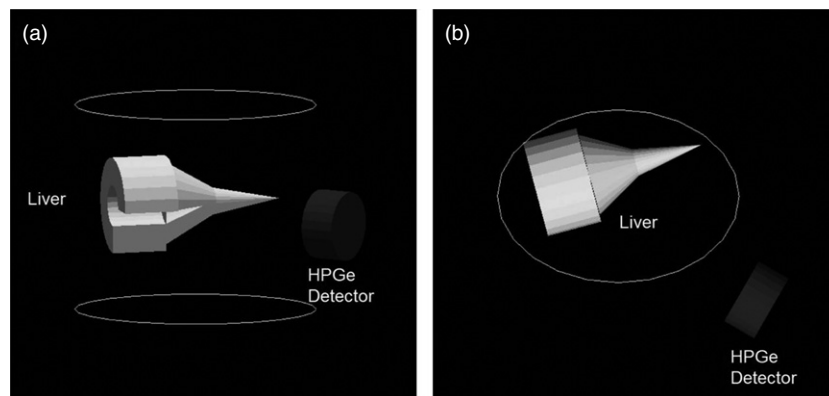
Figure 4. Coronal view (a) and transverse view (b) of the liver phantom.

This phantom was then placed in a GEANT4 model world consisting of a neutron source that emits 7.5 MeV neutrons and an HPGe detector. The beam is modeled as a square profile with no beam divergence. The HPGe detector is located 14 cm from the 'N' phantom off axis from the beam line at 45° within the plane defining a trans-axial slice of the phantom (see figures 5 and 6). All dimensions were set to mimic the actual experimental setup.

2.2.2. The biological model environments. Two different applications were created to simulate NSECT imaging on biological tissue, a breast model and a liver model. The primary use of the breast model was to determine the absorbed energy in order to estimate the absorbed dose. To simplify these dose calculations that depend on exposure volume, the breast is modeled simply as a cylinder 14.0 cm in diameter and 10.0 cm long. It is placed in a GEANT4 world with a neutron source where the neutron energy could be specified at runtime, and an HPGe detector. Figures 3(a) and 3(b) depict two views of the breast model environment geometry.

The geometric design for the liver model is more complex and is formed from one cylinder and two truncated cones (see figures 4(a) and (b)). One quarter of the volume of this assembly

Table 1. Component table for the breast and liver. Tissue density: 1.200 g cm^{-3}.

Element	Breast fractional mass (%)	Liver fractional mass (%)
O	61.43	61.43
C	22.86	22.86
H	9.88	9.62
N	2.57	2.57
Ca	1.43	0.01
P	1.11	1.11
K	0.20	0.99
S	0.20	0.79
Na	0.14	0.24
Cl	0.14	0.28
Mg	0.025	0.06
Fe	0.007	0.02
F	0.004	
Zn	0.003	0.01
Si	0.003	
Cu		0.02

is then removed to more accurately model the shape of the human liver in the region of the spleen. This cut-out can be seen in figure 4(a). In all figures the white ellipses show the outline of the trunk of the body.

The elemental composition by weight for the breast and liver tissue used in the above models is shown in table 1 (Floyd *et al* 2006, NIST 2007, Bender *et al* 2007).

In GEANT4, the model developer specifies the atomic weight and number for each element, and then the percentage of each element within the sample. For this model, naturally occurring isotopic abundances were used for each element. The densities of the organs were artificially enhanced from the actual density of 1.02 g cm^{-3} to 1.2 g cm^{-3} to increase the gamma yield. The implications of this density increase are addressed in the discussion section.

2.3. Simulation experiments

2.3.1. The 'N' phantom experiment. Using the 'N' phantom environment the following experiment was conducted to mimic the tomographic acquisition of the physical phantom in a nuclear laboratory described in Kapadia (2007). In this experiment, a 7.5 MeV neutron beam was created from an accelerated deuteron beam through the 2H(d,n)3He reaction and was collimated to be 7 mm square. The sample rested on a stage which was translated and rotated across the beam line to acquire tomographic projections. There were 11 translation stage stops at intervals of 8 mm, at each of which there were eight rotations at intervals of 22.5°. This resulted in a total of 88 projection sets. All 88 experimental projections were also simulated in the GEANT4 environment.

Gamma production in the sample was measured in the germanium crystal detector. Out of all the gamma rays produced in the sample due to inelastic scattering of a neutron with a target nucleus, only a small fraction will enter the HPGe detector. Of these gammas entering the crystal, only a fraction will deposit their energy into the detector through one or more interactions in the germanium crystal. The total energy deposited per gamma is the sum of the deposited energy from each of these interactions. This information was used to generate a gamma emission energy spectrum of the sample at each projection.
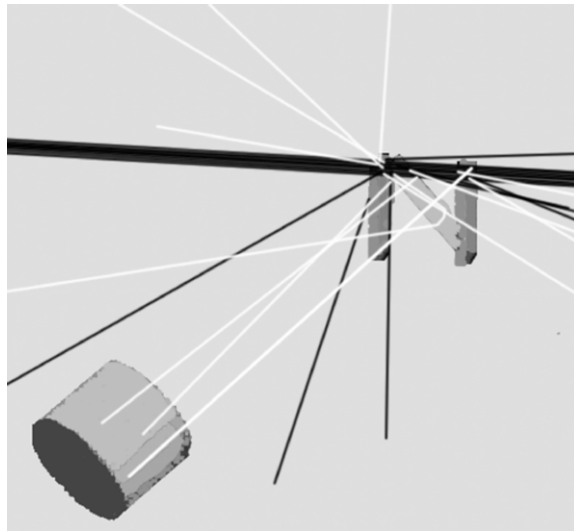
Figure 5. Graphic output of GEANT4 depicting one projection of the simulated tomography experiment using the 'N' phantom.

2.3.2. User-defined limits experiment. To determine an appropriate time limit (in ns) for tracking the lifetime of the neutrons, we examined five output variables (runtime, number of neutrons affected by the cap, number of detector events, energy deposited in the detector and energy deposited in the target) for simulations of 1 million neutron histories for six different neutron lifetime cutoffs (20, 100, 200, 500, 1000 and 2000 ns). This simulation was performed in all three environments outlined above as each phantom had different concentrations of hydrogen, a primary contributor to neutron inelastic scattering.

2.3.3. Estimate of the radiation dose. Simulations were conducted on the two biological models to determine the amount of energy absorbed in the target. This value was then used to obtain a dose estimate. Each simulation consisted of 1 million incident neutrons at 7.5 MeV contained in a 1 cm square beam with a square profile. Energy deposited in the sample due to both neutron and other secondary interactions (such as gamma absorption) was reported for each incident neutron and appropriate dose calculations were then performed.

3. Results

3.1. 'N' Phantom

Our first simulation successfully simulated the tomography experiment. Figures 5 and 6 show the phantom at three different projection orientations from the tomography simulation.

In figures 5 and 6, neutrons are represented by black tracks, gammas by white tracks, and the detector by a shaded cylinder. The neutron beam (solid dark lines) enters from the left. The 'N' phantom in the upper right corner is shown with the outer copper pieces shaded dark gray and the inner iron pieces shaded lighter gray. As can be seen, most incident neutrons do not interact with the sample and simply pass through the phantom (solid dark lines exiting to the right of the figure). Some neutrons scatter elastically and emerge at new angles. Neutrons
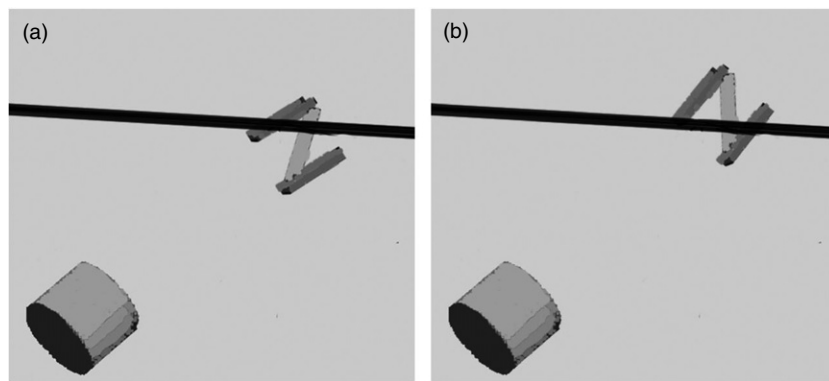
Figure 6. The phantom at the second (a) and third (b) of three different projection orientations. As seen here, most neutrons pass through the phantom without any interactions.
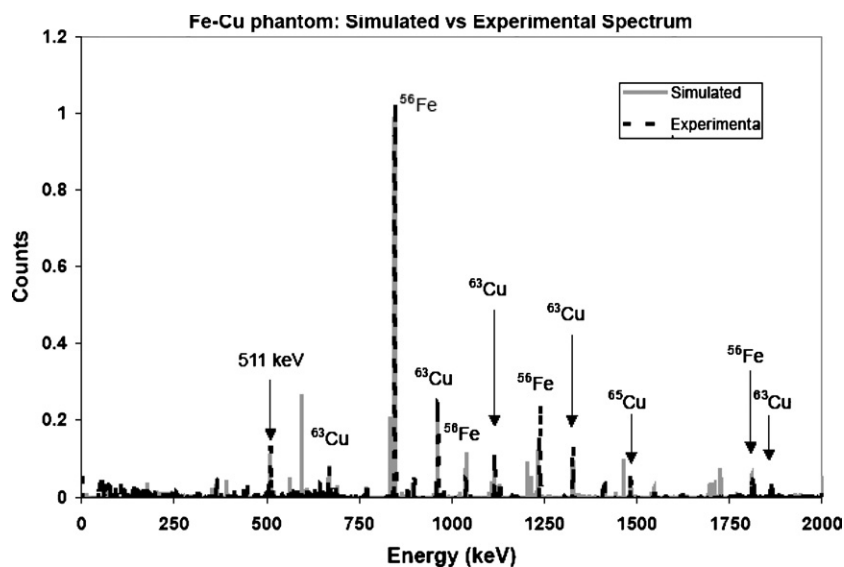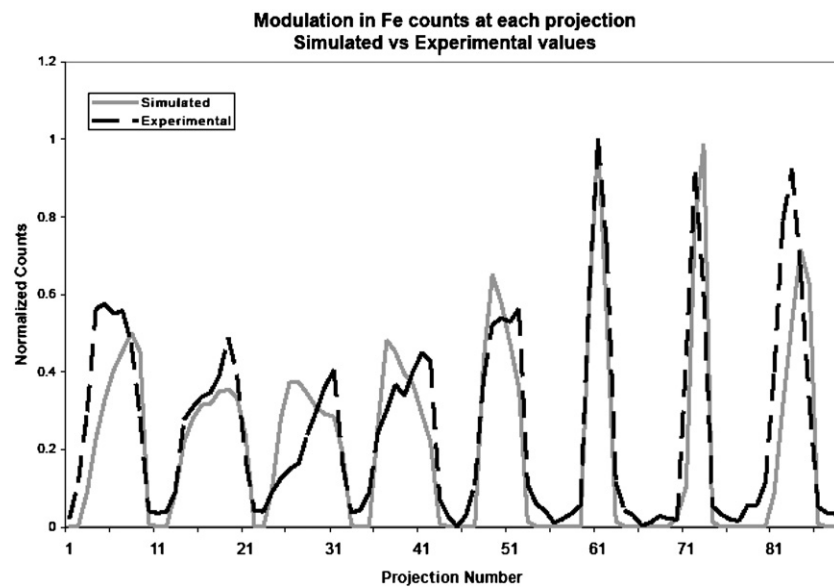

Figure 7. Comparison of experimental and simulated spectra for the 'N' phantom.

of interest to NSECT scatter inelastically and produce gammas (white tracks). A fraction of these gammas are then stopped in the detector.

Figure 7 shows a comparison between the experimental spectra from the tomographic acquisition of the iron and copper phantom (dashed black line) and the GEANT4 simulation of the same experiment (solid gray line). There is very good agreement between the two spectra for gamma energies above 500 keV and was achieved on the first run of the simulation. This agreement provides convincing evidence that the GEANT4 simulations are accurately representing the experimental conditions including the majority of the sources of gamma backgrounds for energies above 511 keV (Kapadia 2007).

Additionally, a plot of the number of iron and copper counts at each projection was compiled to determine if the simulation environment was translating and rotating the sample as expected. Figure 8 is a comparison between the simulation and experiment for the iron

Figure 8. Comparison of Fe counts achieved at all projections for the experimental and simulated data.

Figure 9. Reconstructed simulated data. Left: copper, center: iron, right: combined copper and iron reconstructions.

counts obtained at each projection. While the peaks are not completely overlapping, the shape of the data is consistent. Some variation between the simulated and experimental setup is expected because the experimental setup is prone to minor positioning errors originating from the finite precision of the translation stage. In reality translation is only as good as the translation and rotation stages that are being used, while in simulation, translation is perfect. What is important is that the modulation trend in the number of gamma events is consistent between the experimental and simulated data.

The simulated data were then reconstructed using the maximum likelihood expectation maximization (MLEM) algorithm (Lange and Carson 1984) which was used to reconstruct the original experimental data described in Kapadia (2007). Figure 9 shows the resulting image after attenuation correction (Kapadia and Floyd 2005). The 'N' shape is clear and consistent with the shape of the phantom. Both the modulation profile and match in reconstructed
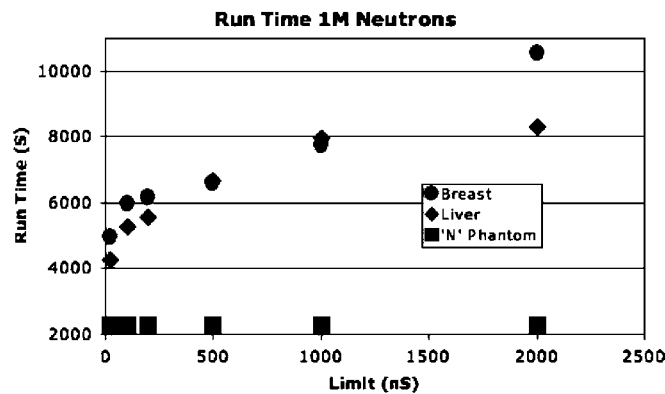
Figure 10. Monte Carlo runtime as a function of neutron lifetime cutoff limit for the three different phantoms. ●– breast phantom. ◆– liver phantom. ■– 'N' phantom.

images confirm that a different part of the phantom is being interrogated at each projection, and therefore the phantom is being translated through the beam.

3.2. User-defined limits

The second simulation determined the effect of user-defined limits on five different aspects of an NSECT simulation. The first aspect examined was runtime as a function of user-selected cutoff on the neutron lifetime. The results are shown in figure 10, where a sharply decreasing runtime for the breast and liver models is observed as the cutoff is lowered below 100 ns.

As expected, little effect from cutoff time was seen for the hydrogen-lacking 'N' phantom model, and as the cutoff was raised to 2000 ns, the runtimes increase in the hydrogen-rich biological models. While the minimum runtime would occur at a cutoff time that is less than the time needed for neutrons to interact with the target, this would eliminate all reactions of interest. Therefore, the following four parameters must be considered when choosing an optimal cutoff time.

The second aspect examined was the fraction of incident neutrons whose lifetimes were truncated by the user limit. The results are presented in figure 11. As expected, the fraction was high for short cutoff lifetimes and then becomes asymptotically constant for longer times.

Again, no effect is seen for the hydrogen-lacking 'N' phantom. This fraction would have a maximum value of 1.0 when the cutoff time was less than that necessary for the neutrons to interact with the target.

The third aspect examined was the effect of user-defined limits on the number of detected events (shown in figure 12). As gamma detection follows Poisson counting statistics, the counting error in these measurements is the standard counting error for Poisson distributions, which is the square root of the number of events detected. For each of the data points, these errors are within the size of the figure markers.

As expected, there is a sharp decrease in detected events as the cutoff time becomes shorter and the number of events becomes asymptotic as the cutoff time grows.

The fourth aspect analyzed was the impact of the cutoff time on the energy deposited in the detector (shown in figure 13). It is difficult to discern any pattern as the results are variable depending on the type of tissue, especially below 1000 ns. The error in measuring the energy deposited depends on the energy resolution of the detector, which is less than 1% FWHM at 7.5 MeV. This error is within the confines of the figure marker.

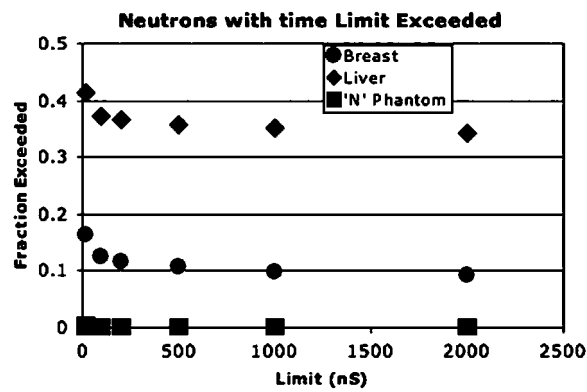**Figure 11.** Number of neutrons that were terminated as a result of their exceeding the user-defined cutoff on the neutron lifetime plotted as a function of the cutoff limit.
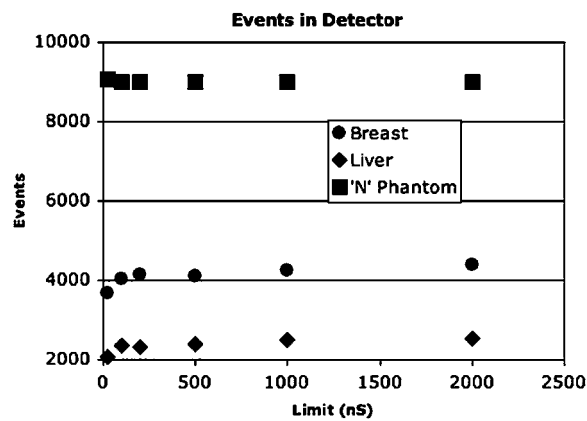

Figure 12. Number of detected events in the HPGe detector as a function of the cutoff on the neutron lifetime.
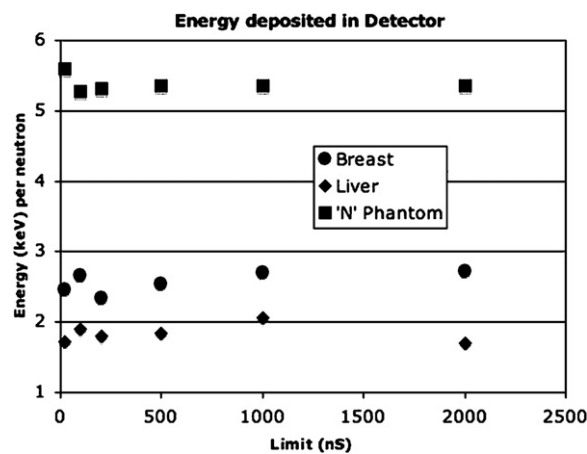

Figure 13. Energy deposited in the detector as a function of the cutoff on the neutron lifetime.
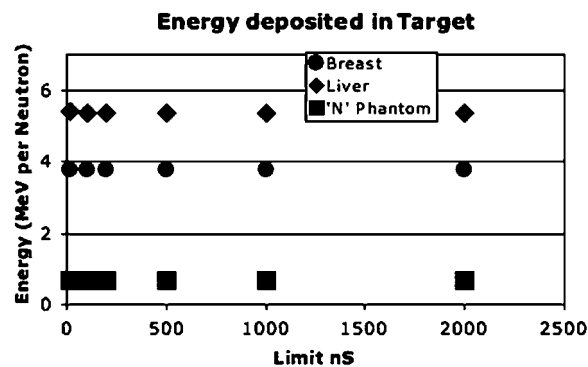
Figure 14. Energy deposited in the target volume as a function of the cutoff on the neutron lifetime.

For both figures 12 and 13 there would be no events or energy deposited in the detector if the cutoff limit was shorter than the time necessary for neutrons to interact in the target and stimulate a gamma event.

The final aspect examined was the dependence of the energy deposited in the target as a function of the cutoff time (shown in figure 14).

This figure shows no impact over the range of cutoff values considered and there was no change in the energy deposited in the sample as the time was varied from 20 to 2000 ns. Therefore, the smallest lifetime cutoff of 20 ns is enough time for the neutrons to reach, interact and deposit their energy in the sample. Because all energy is deposited in the sample within a small timeframe, limiting the neutron tracking lifetime should not affect the measurement of energy deposited in the sample. Only the non-instantaneous measurement of detected events and energy in the detector will be affected by the neutron lifetime cutoff (figures 12 and 13).

Based on the above data we have chosen to run our simulations with a cutoff time limit of 1000 ns. This choice will be further explained in the discussion section.

3.3. Estimate of the radiation dose

The third simulation was to measure the total energy deposited in the sample and use this value to calculate the absorbed dose to the breast and liver. Based on the results from the second experiment, the energy deposited in the target per 7.5 MeV incident neutron is 3.74 MeV for the breast and 5.38 MeV for the liver (see figure 14). 82% of the incident neutrons were seen to interact in the breast while 93% were seen to interact in the liver. From this data the total energy absorbed in the breast and the liver was calculated for 1 million incident neutrons. Using the total energy absorbed and the exposed volume of tissue we calculate the absorbed dose to the breast and liver. To calculate the equivalent dose, the absorbed dose is multiplied by the particle weighting factor for neutrons (10 at 7.5 MeV) (Turner 2004). For the breast, the equivalent dose was calculated to be 0.498 mSv. The same computation for liver found an equivalent dose of 0.239 mSv. Table 2 shows the complete calculations. Note that these dose calculations are limited to the target organs only, not the entire body.

4. Discussion

In order to design a functional NSECT system, a valid simulation environment must be developed. Due to the logistics surrounding the neutron beam source and the long experimental

Table 2. Equivalent dose to the breast and liver.

	Breast	Liver
Energy absorbed = number of neutrons × energy deposited	1×10^6 neutrons × 3.74 MeV/ neutron × 1.6×10^{-13} J MeV^{-1} = **5.98×10^{-7} J**	1×10^6 neutrons × 5.38 MeV/ neutron ∗ 1.6×10^{-13} J MeV^{-1} = **8.61×10^{-7} J**
Exposure volume	10 cm^3	30 cm^3
Density	1.2 g cm^{-3}	1.2 g cm^{-3}
Mass	0.012 kg	0.036 kg
Absorbed dose = energy absorbed per kg of exposed tissue	5.98×10^{-7} J/0.012 kg = **4.98×10^{-5} Gray (J kg^{-1})**	8.61×10^{-7} J/0.036 kg = **2.39×10^{-5} Gray (J kg^{-1})**
Equivalent dose = Absorbed Dose × particle weighting factor	4.98×10^{-5} Gray × 10 = **0.498 mSv**	2.39×10^{-5} Gray × 10 = **0.239 mSv**

times, it is not practical to develop a system by experimentation alone. A simulation environment allows more rapid development and iteration on new ideas and setups.

This paper demonstrates that the GEANT4 simulation environment successfully addresses three major concerns of modeling NSECT: positioning of the beam line relative to the sample, effective modeling of low energy neutrons in hydrogen rich tissue and measuring the absorbed energy to quantify the dose.

The first simulation demonstrated successful modeling of the tomographic experimental NSECT interrogation of the 'N' phantom. Due to the complexity of the Monte Carlo method, the GEANT4 toolkit and the model, it is prudent to validate the simulations with experimental data. The simulated spectra were in close agreement with experimentally acquired spectra. This result indicates that GEANT4 can successfully model the gamma radiation due to neutron inelastic scattering and the subsequent detection of the gammas in the HPGe detector crystal. Additionally, the simulated tomographic runs achieved similar modulation in the energy spectrum as that of the experiment, indicating that the model was able to produce a neutron beam of expected width and successfully translate the phantom through this beam. This simulation allowed comparison of both the spectral results and the tomographic results. It also demonstrated the toolkit's ability to generate legitimate gamma energy spectra and to simulate the relative position between the beam line and the sample.

The second simulation was performed to develop a solution for a challenge presented by simulation of biological tissue. Neutrons in a hydrogen rich environment are sometimes slowed through elastic scatter and continue to 'drift' within the tissue sample for very long computation times making the simulation far too slow to be feasible. A GEANT4 modeling feature allows the limiting of tracking time for a neutron and the imposition of tracking limitations in order to increase the speed of the simulation. In order to determine the effect of these cutoff times, a parametric analysis was performed on all three models and an appropriate time limit was determined.

The results of the user-defined time limit experiments have led us to choose a limit of 1000 ns. Implementation of this limit decreased the runtime of the code in general by a factor of over 2 and in one extreme case runtime was decreased from over a week down to 2 h. Initially it may seem reasonable to consider cutoff values less then 1000 ns as the cutoff appears to have little impact on energy deposited in the target (figure 14). For example, dropping the cutoff from 1000 ns to 100 ns would decrease the runtime by up to 30% (from 8000 s to 5500 s). However, the energy deposited in the detector appears somewhat unstable for cutoff values less than 500 ns (figure 13). Additionally, a primary limitation for interpreting the spectra from these simulations is the small number of detected events, and as the cutoff

time is shortened there is a slight decrease in the number of events in the detector (figure 12). For the above reasons, the cutoff should be kept as high as practical (1000 ns).

It is important to note that the measure of energy deposited in the target did not change based on the cutoff time (figure 14). This finding bolsters confidence that, regardless of the chosen cutoff time, the dose calculations will remain constant. This is important because a major benefit of simulations is the ability to determine the dose in the interrogated tissue.

In the third and final simulation both the breast and liver models were interrogated to determine energy deposited in tissue samples during an NSECT imaging exposure. This quantity was then used to determine the radiation dose to a specific organ that results from a typical NSECT interrogation of biological tissue. Both dose levels were below 1 mSv, which is the dose delivered by a standard two-view mammogram. To decrease simulation time, experiments in this study are performed with an artificially enhanced tissue density. An artificially enhanced tissue density results in a larger number of neutron scattering events per incident neutrons, and therefore fewer incident neutrons are needed to generate a significant number of gamma rays in the energy spectrum. In reality, with normal tissue density, a larger number of incident neutrons would be necessary to generate a significant number of counts at spectral energy peaks. However, while increasing the number of incident neutrons from 1 to 10 million would increase the dose by a factor of 10, the dose would increase to approximately 5 mSv, which is more than a mammogram but less than a chest CT (approximately 20 mSv).

5. Conclusion

This paper has demonstrated that the GEANT4 simulation environment produces accurate gamma spectra and effectively models tomographic translations by mimicking an NSECT experiment. A limit on neutron tracking has been determined that does not affect integral simulation results and this limit has been used in a simulation environment to determine the neutron dose. The data presented herein not only demonstrate the successful modeling of the NSECT experimental acquisition environment, but also indicate that GEANT4 is an adequate Monte Carlo toolkit for NSECT simulation. Given this powerful tool for simulating the NSECT environment, rapid development of NSECT as a biomedical investigational tool is envisioned.

Acknowledgments

References

Agostinelli S *et al* 2003 Geant4—a simulation toolkit *Nucl. Instrum. Methods* A **506** 250–303
Bender J, Kapadia A J, Sharma A C, Tourassi G D, Harrawood B P and Floyd C E 2007 Breast cancer detection using neutron stimulated emission computed tomography: prominent elements and dose requirements *Med. Phys.* **34** at press
CERN GEANT4 available from: http://geant4.web.cern.ch/geant4/
CERN 2007 GEANT4 HyperNews Forums. In: http://geant4-hn.slac.stanford.edu:5090/Geant4-HyperNews/index
Floyd C, Bender J E, Sharma A C, Kapadia A J, Xia J Q, Harrawood B P, Tourassi G D, Lo J Y, Crowell A S and Howell C R 2006 Introduction to neutron stimulated emission computed tomography *Phys. Med. Biol.* **51** 3375–90
Floyd C E *et al* 2004 Neutron stimulated emission computed tomography of stable isotopes *Proc. SPIE* **5368** 248–54

Floyd C *et al* 2007 Neutron stimulated emission computed tomography: background corrections *Nucl. Instrum. Methods* B **254** 329–36

Kapadia A J 2007 Accuracy and patient dose in neutron stimulated emission computed tomography for diagnosis of liver iron overload: simulations in GEANT4 *Doctoral Dissertation* Duke University

Kapadia A and Floyd C E 2005 An attenuation correction technique to correct for neutron and gamma attenuation in the reconstructed image of a neutron stimulated emission computed tomography (NSECT) system *Proc. SPIE* **5745** 737–43

Lange K and Carson R 1984 EM reconstruction algorithms for emission and transmission tomography *J. Comput. Assist. Tomogr.* **8** 306–16

NIST 2007 *Database of Natural Matrix Reference Materials: Bovine Liver* (National Institute of Standards and Technology)

Turner J 2004 *Atoms, Radiation, and Radiation Protection* (Strauss: Wiley)

Breast cancer detection using neutron stimulated emission computed tomography: Prominent elements and dose requirements

Janelle E. Bender,[a] Anuj J. Kapadia, and Amy C. Sharma
Department of Biomedical Engineering and Duke Advanced Imaging Laboratories, Department of Radiology, Duke University, Durham, North Carolina 27708

Georgia D. Tourassi and Brian P. Harrawood
Duke Advanced Imaging Laboratories, Department of Radiology, Duke University, Durham, North Carolina 27708

Carey E. Floyd, Jr.
Department of Biomedical Engineering and Duke Advanced Imaging Laboratories, Department of Radiology, Duke University, Durham, North Carolina 27708

Neutron stimulated emission computed tomography (NSECT) is being developed to noninvasively determine concentrations of trace elements in biological tissue. Studies have shown prominent differences in the trace element concentration of normal and malignant breast tissue. NSECT has the potential to detect these differences and diagnose malignancy with high accuracy with dose comparable to that of a single mammogram. In this study, NSECT imaging was simulated for normal and malignant human breast tissue samples to determine the significance of individual elements in determining malignancy. The normal and malignant models were designed with different elemental compositions, and each was scanned spectroscopically using a simulated 2.5 MeV neutron beam. The number of incident neutrons was varied from 0.5 million to 10 million neutrons. The resulting gamma spectra were evaluated through receiver operating characteristic (ROC) analysis to determine which trace elements were prominent enough to be considered markers for breast cancer detection. Four elemental isotopes (^{133}Cs, ^{81}Br, ^{79}Br, and ^{87}Rb) at five energy levels were shown to be promising features for breast cancer detection with an area under the ROC curve (A_Z) above 0.85. One of these elements—^{87}Rb at 1338 keV—achieved perfect classification at 10 million incident neutrons and could be detected with as low as 3 million incident neutrons. Patient dose was calculated for each gamma spectrum obtained and was found to range from between 0.05 and 0.112 mSv depending on the number of neutrons. This simulation demonstrates that NSECT has the potential to noninvasively detect breast cancer through five prominent trace element energy levels, at dose levels comparable to other breast cancer screening techniques. © *2007 American Association of Physicists in Medicine.* [DOI: 10.1118/1.2775669]

Key words: Monte Carlo, neutrons, tomography, gamma-ray spectroscopy, breast cancer

I. INTRODUCTION

Neutron stimulated emission computed tomography (NSECT) is a new technique being developed to noninvasively image the elemental composition of tissues within the human body.[1–3] When a high-energy fast neutron (2.5–5 MeV) inelastically scatters off an atomic nucleus, the nucleus is excited, and a gamma ray is emitted. The energy of the gamma is characteristic of the atomic nucleus with which it interacted. By analyzing the energy levels of the emitted gammas when a sample is bombarded with many neutrons, the elemental composition can be determined.

Many studies have shown there to be a difference in the elemental composition of normal, benign, and malignant tissue in humans for a large variety of cancers, including breast cancer,[4–8] prostate cancer,[9] and glioblastoma multiforme.[10] To determine compositional differences, these studies have required invasive methods such as biopsy. The NSECT technique has the potential to measure these differences nonin-

vasively, *in vivo*, with a reduced dose compared to four-view screening mammography.[2]

NSECT has the potential to evolve into a powerful, low-dose screening or diagnostic technology for breast cancer. Numerous studies using x-ray fluorescence (XRF)[6,11] and neutron activation analysis (NAA)[8,12] have shown increased concentrations of trace elements in malignant breast tissue compared to adjacent normal tissue. One XRF study showed that there were elevated levels of Fe, Cu, Zn, and K in human breast tumor tissue when compared to healthy breast tissue.[11] This study utilized fluorescence emitted from the elements in *ex vivo* breast tissue samples with a synchrotron-based system. In XRF, tissue samples remain intact and there is direct quantification of the elements, but the system necessitates the use of biopsied tissue. Another study found that malignant breast tissue has significantly higher concentrations of 12 trace elements (Al, Br, Ca, Cl, Co, Cs, Fe, K, Mn, Na, Rb, and Zn) when compared to adjacent normal breast tissue.[12] This study employed NAA, an invasive and destruc-

tive technique, which typically involves freeze-drying of excised breast tissue.[13] Because measurements were made on dried tissue, a wet-to-dry ratio had to be implemented in order to convert values to ones relevant in intact breast tissue. Additionally, NAA renders the interrogated sample radioactive. While NAA is high in sensitivity, it lacks the ability to be translated to a low-dose _in vivo_ method.

We present NSECT as an imaging modality that has the potential to be translated to the clinic, due to its noninvasive nature. NSECT is intended to provide tomographic projections by scanning a sample with a high-energy fast neutron beam, formed via the $d(d,n)^3$He fusion reaction. We have already demonstrated spectroscopic acquisition over a broad energy range that encompasses many elements of interest for biological imaging.[1] The present study uses Monte Carlo simulations and receiver operating characteristic (ROC) analysis to investigate the performance of different elements in differentiating malignant and normal breast tissue at appreciably low-dose levels, in accordance with the As Low As Reasonably Achievable (ALARA) concept and at levels used in currently approved screening techniques. Before evaluations can be performed on anatomic models of the breast containing lesions and nodules with trace element concentration differences, it must be tested whether it is possible to detect any trace element concentration changes in the presence of all the scatter noise generated by the tissue. Hence this study is restricted to single projection spectra of models of bulk breast tissue to investigate the feasibility of NSECT in trace element quantification to detect breast cancer.

II. METHODS

II.A. Monte Carlo simulations

Monte Carlo simulations were designed using GEANT4.[14] Bulk breast tissue was modeled as an ellipsoid 10 cm × 6 cm × 5 cm. Two high-purity germanium (HPGe) detectors[15] were modeled as cylinders of 5.32 g/cm³ density germanium with 12 cm diameter and 5 cm height. The two HPGe detectors flanked the breast tissue and were separated by 11.6 cm. The neutron source was modeled in GEANT4 as a fast neutron (2.5 MeV) beam of 1 cm² area with a square profile, which was directed incident upon bulk breast tissue. See Fig. 1 for a schematic of the GEANT4 setup.

In the case of neutron inelastic scattering, the nucleus is excited and emits a characteristic gamma ray. GEANT4 determines the direction of the emitted gamma, which may then be deposited in one of the two gamma detectors. The gamma ray energy deposited in each detector was tabulated to form a gamma spectrum showing energy levels and corresponding gamma counts, or intensity. The energy was then matched to the element with which the neutron had an interaction, which was deduced using a lookup table from the Evaluated Nuclear Data Files (ENDF) database.[16]

Breast tissue was modeled as either being normal or malignant, with elemental compositions[12] as seen in Table I. Despite a broad distribution of concentrations in the malignant specimens from the study in which these values were derived, the authors were able to see significantly higher
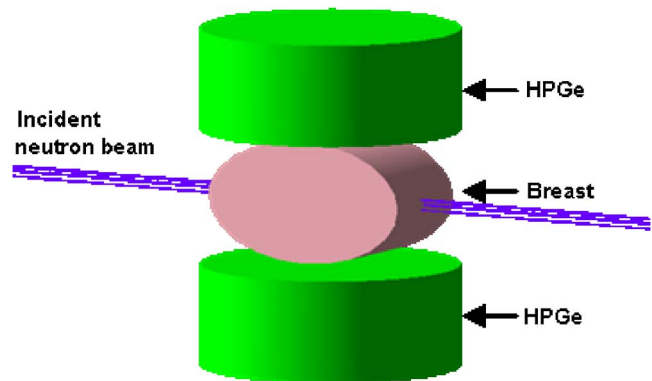

FIG. 1. GEANT4 setup. Two HPGe detectors flank the breast tissue. Incoming neutrons strike at the face of the breast.

concentrations of all elements in the freeze-dried malignant specimens in comparison with the normal ones. The normal breast tissue was modeled with a density of 0.93 g/cm³, and the malignant breast tissue was modeled with a density of 1.058 g/cm³, which correspond to adipose tissue and masses, respectively.[17] Over 99% of the breast tissue is comprised of O, C, H, and N so we used a neutron energy (2.5 MeV) low enough to avoid excitation of O, C, and N. The 2.5 MeV was also high enough to excite the trace elements of interest. We did see neutron capture on H, which was easily distinguishable. The remainder of the peaks can be attributed to excitations from the trace elements, which are of interest because they can be linked to malignancy.

One hundred simulations of 10 million incident neutrons were run on both the normal and malignant models. For each simulation, a new random seed was generated, which was different between the malignant and normal runs, so that the runs were uncorrelated. Additionally, 100 runs each of 0.5

TABLE I. Breast tissue composition for normal and malignant models. The percentages were calculated by first converting dry weights to wet weights.

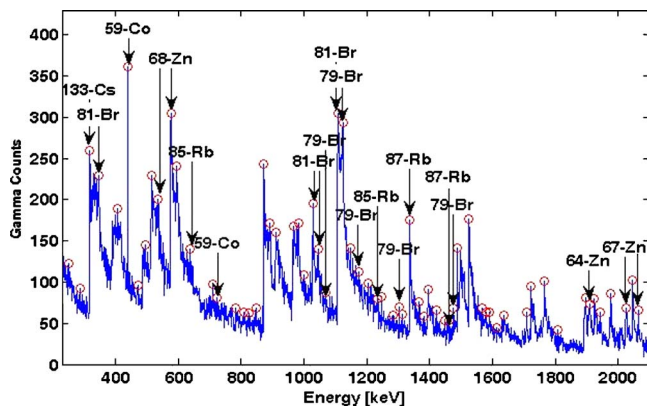|	Normal (%)	Malignant (%)
Oxygen	61.429	61.429
Carbon	22.857	22.857
Hydrogen	12.649	12.510
Nitrogen	2.571	2.571
Chlorine	1.98E−1	2.15E−1
Sodium	1.85E−1	2E−1
Potassium	8.94E−2	1.96E−1
Iron	9.8E−3	7.85E−3
Calcium	8.29E−3	1.13E−2
Zinc	1.17E−3	1.14E−3
Bromine	7.07E−4	6.55E−4
Aluminum	6.67E−4	5.7E−4
Rubidium	5.98E−4	5.84E−4
Manganese	3.88E−5	3.16E−5
Cobalt	2.06E−5	1.98E−5
Cesium	3.27E−7	3.6E−7

FIG. 2. Spectrum of 10 million incident neutrons from the normal breast model. The circles represent energy levels at which the counts exceeded 40 and at which the counts exceeded all counts in a ±10 keV window. Labels are provided for those peaks that matched elements found in the modeled breast tissue.

million, 1 million, 2 million, 3 million, and 5 million incident neutrons were produced. This yielded a total of 600 spectral scans per tissue type.

II.B. Peak-identification algorithm

For each output file, the energies in keV were tabulated to yield spectra of gamma energy and corresponding gamma intensity. The first task was to determine whether or not the intensity at a specific energy could be considered a peak in the spectrum. To be called a peak, three criteria had to be met: (1) the peak had to exceed a set minimum count level, (2) the peak had to be larger than all other peaks in a specified window, and (3) the peak energy had to match to one of the elements in the breast tissue model. The minimum peak height was set to be 40 counts, which exceeded the underlying noise throughout the energy range (0–2500 keV). An iterative technique was used to optimize the window width. Window widths were varied form ±2 to ±20 keV, and the number of detected peaks was correlated with the number of expected peaks in the simulated spectra. The best results were seen for a window width of ±10 keV. The element that the characteristic energy represented was determined using the ENDF tables. Figure 2 shows an example of the peak-identification technique for one of the runs of 10 million incident neutrons. The circles mark the energies that fit the first two criteria, and the labels note the corresponding element if the peak fit the third criterion.

The process of peak identification was performed on output files from the 100 normal and 100 malignant simulations for the 10 million incident neutrons level. Peak identification was performed only for the highest incident neutron level as a best-case scenario to identify peaks that could be detected in the breast tissue.

II.C. ROC analysis

The detectability index was the area under the binormal ROC curves, or A_z. The significance of a peak at lower levels of incident neutrons was determined by monitoring the

degradation in the area under the ROC curve for that peak as the number of incident neutrons was reduced. In order for a specific energy peak to be used in the ROC analysis, more than 50 of the 100 files for each case (normal or malignant) had to register the given peak. The purpose of this criterion was to focus only on the peaks found in the majority of each tissue model. Note that as long as more than half of the files registered the peak, the counts for all files were entered for ROC analysis. The ROC analysis was conducted for each of the matched energies using the counts for that energy level from all 100 runs for normal and 100 runs for malignant as the input data to the software, ROCKIT.[18] ROCKIT uses maximum likelihood estimation to fit a binormal ROC curve to continuously distributed data and/or categorical data.[19] There were two categories for the ROC analysis: "actually negative" and "actually positive," which respectively correspond to normal and malignant status.

Because ROC analysis was performed on a moderately small sample size ($n=200$), it was expected that A_z estimates would have a relatively large variance. To ensure that the peaks selected had good discriminatory ability, we applied a minimum threshold of $A_z=0.85$.

II.D. Dose calculations

One of the primary concerns with any potential clinical imaging technique is the absorbed patient dose. The dose was calculated for each run as follows. Using a separate Monte Carlo simulation with the same parameters and setup as described in Sec. II A, the average energy due to both neutron and other secondary interactions deposited in the breast tissue per 2.5 MeV incident neutron was determined to be 1.4 MeV.[9] As the neutrons irradiated a 10 cm^3 volume of tissue, corresponding to a neutron beam surface of 1 cm^2 over a 10 cm depth, the total irradiated mass could be calculated using the density of the breast tissue. This was then converted into the absorbed dose, $D_{T,R}$, in a tissue or organ T due to radiation R, measured in J/kg or Sv. The equivalent dose, $H_{T,R}$, was then calculated as in Eq. (1), where ω_R is the radiation weighting factor. For neutrons with energy between 2 and 20 MeV, $\omega_R=10$ (Ref. 20). The effective dose, E, to the breast tissue was calculated using Eq. (2), where ω_T is the tissue weighting factor, which for breast is equal to 0.05 (Ref. 21).

$$H_{T,R}= \omega_R \cdot D_{T,R}, \tag{1}$$

$$E= \omega_T \cdot H_{T,R}. \tag{2}$$

Using the method described above, the effective dose was estimated to be 1.12E-8 mSv/neutron.

III. RESULTS

For the 100 normal tissue runs of 10 million incident neutrons, 28 energy levels were found to be peaks in over half of the runs. For the 100 corresponding malignant runs, 30 energy levels were designated as peaks in over half of the runs. These energy levels were queried in the ENDF tables; eight levels in the normal model and ten levels in the malignant

TABLE II. Number of energy levels and corresponding elemental matches for both the normal and malignant models. A checkmark indicates the matches were found in over half of the output files. The number in parentheses is the number of output files that had a match out of the total 100 files.

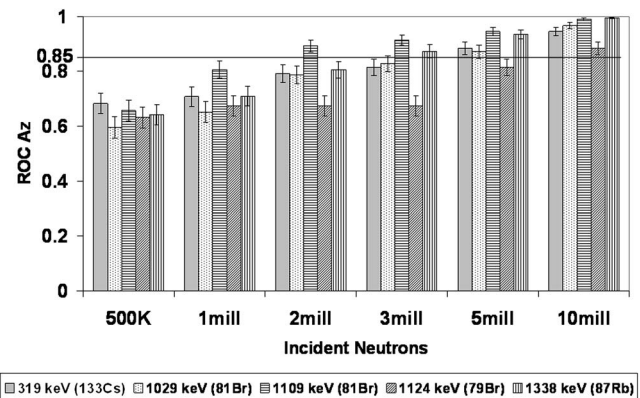|		Normal	Malignant
319 keV	^{133}Cs	√ (98)	√ (90)
439 keV	^{59}Co	√ (100)	√ (100)
1029 keV	^{81}Br	√ (100)	√ (99)
1109 keV	^{81}Br	√ (85)	√ (56)
1124 keV	^{79}Br	(43)	√ (51)
1191 keV	^{79}Br	√ (51)	√ (60)
1338 keV	^{87}Rb	√ (95)	√ (97)
1476 keV	^{79}Br	√ (79)	√ (61)
1697 keV	^{41}K	(49)	√ (54)
2065 keV	^{67}Zn	√ (60)	√ (70)

FIG. 3. ROC A_z for the prominent energy levels over all incident neutron count levels. The horizontal line at 0.85 marks the cutoff for prominence.

model corresponded to elements from the breast tissue model. All eight energy peaks from the normal model were also found in the malignant model, suggesting that they robustly appear in the majority of tissue samples from each population. Table II summarizes the energy levels and the corresponding number of matches for normal and malignant models.

A total of ten energy levels was found to be peaks in over half the runs in either tissue model using 10 million incident neutrons. Only these peaks were further analyzed with ROC at the six different incident neutron levels considered in this simulation. ROC analysis on the 60 total energy level/incident neutron combinations yielded 12 total combinations with ROC $A_z > 0.85$. As seen in Table III, each of these combinations corresponded to one of five separate energy

levels—319, 1029, 1109, 1124, and 1338 keV, representing elements ^{133}Cs, ^{81}Br, ^{81}Br, ^{79}Br, and ^{87}Rb, respectively. Aside from 1124 keV, all these prominent energy levels satisfied the condition of element matching in over 50 of 100 normal and malignant output files. For 1124 keV, this condition was satisfied only for the malignant tissue model. One combination—1338 keV with 10 million incident neutrons—yielded a perfect A_z value of 1.00. Figure 3 summarizes the mean and standard deviation of the ROC A_z values as a function of number of neutrons for all energy levels.

No discriminatory elements were found at the lowest two incident neutron levels (0.5 million and 1 million), but ^{81}Br at 1109 keV was found to be significant at the 2 million incident neutron level. Figure 4 shows the summation of all

TABLE III. Elements and corresponding average and standard error for ROC Az values obtained from ROCKIT software. The values in bold are above the significance threshold of Az=0.85 and are considered significant. The significant error ranged from 0.01 to 0.05.

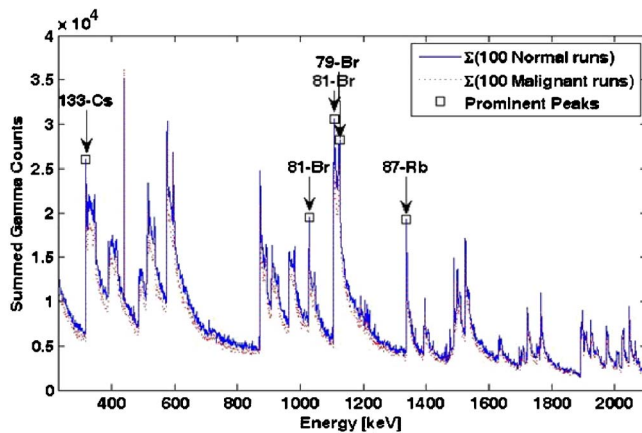| keV	Millions of Incident Neutrons					
	0.5	1	2	3	5	10
319 ^{133}Cs	0.68±0.04	0.71±0.04	0.79±0.03	0.81±0.03	**0.88±0.02**	**0.95±0.01**
439 ^{59}Co	0.54±0.04	0.58±0.04	0.58±0.04	0.64±0.04	0.61±0.04	0.67±0.04
1029 ^{81}Br	0.60±0.04	0.65±0.04	0.79±0.03	0.83±0.03	**0.87±0.02**	**0.97±0.01**
1109 ^{81}Br	0.66±0.04	0.81±0.03	**0.89±0.02**	**0.91±0.02**	**0.95±0.02**	**0.99±0.01**
1124 ^{79}Br	0.63±0.04	0.67±0.04	0.67±0.04	0.67±0.04	0.81±0.03	**0.89±0.02**
1191 ^{79}Br	0.57±0.04	0.57±0.04	0.58±0.04	0.64±0.04	0.64±0.04	0.74±0.03
1338 ^{87}Rb	0.64±0.04	0.71±0.04	0.81±0.03	**0.87±0.02**	**0.93±0.02**	**1.00**
1476 ^{79}Br	0.60±0.04	0.67±0.04	0.72±0.04	0.75±0.03	0.76±0.03	0.85±0.03
1697 ^{41}K	0.52±0.04	0.49±0.04	0.50±0.04	0.56±0.04	0.58±0.04	0.66±0.04
2065 ^{67}Zn	0.47±0.04	0.54±0.04	0.54±0.04	0.58±0.04	0.60±0.04	0.66±0.04

FIG. 4. The 100 normal and ten malignant spectra of 10 million incident neutrons were summed. The squares mark the energy levels found to be highly discriminatory in the ROC analysis.

normal and malignant runs for 10 million incident neutrons and indicates the peaks that were found to be prominent in the ROC analysis.

The dose values calculated for the neutron count levels that yielded prominent elements ranged from 0.0224 to 0.112 mSv, depending on the number of incident neutrons. For 2 million neutrons, the total dose to the volume of breast tissue that was irradiated was only 0.0224 mSv, which is only a fraction of the dose reported for other breast cancer screening methods,[22] and even when the number of incident neutrons is maximized to 10 million, the dose to the breast tissue is still low enough to indicate NSECT's potential as a breast cancer screening technique.

IV. DISCUSSION

This simulation study demonstrates NSECT's feasibility to detect differences in the concentration of several discriminatory trace elements that indicate cancer in breast tissue. We have demonstrated the ability to see peaks corresponding to elements in both the normal and malignant bulk breast tissue model. The results indicate that four elemental isotopes, ^{133}Cs, ^{81}Br, ^{79}Br, and ^{87}Rb, are prominent in differentiating normal from malignant tissue at neutron flux values corresponding to clinically relevant dose levels. One of these elements achieved perfect classification at 10 million neutrons and was able to differentiate normal and malignant tissue at a neutron flux as low as 3 million neutrons. As low neutron flux directly implies low dose, these elements are vital for a low-dose clinical implementation of NSECT for breast cancer detection. Further, the ability of these elements in differentiating normal and malignant tissue suggests that NSECT has the potential to be translated into a clinical breast cancer screening modality.

The breast in this study was modeled as a bulk section of malignant or normal breast tissue. This was done to test the feasibility of NSECT to detect breast cancer markers in malignant tissue and determine which marker elements are most indicative of cancer. As this feasibility has now been demonstrated, a logical extension to this study will be to model the

anatomy of the normal and malignant breast more accurately to investigate the feasibility of detecting element changes within tumors. The issue of patient-specific variability in elemental composition has been studied using several different techniques, including neutron activation analysis, x-ray fluorescence, and atomic absorption spectrophotometry. Although these studies do indicate patient-specific variability, they still show significant increases in elemental concentrations in cancerous tissue. Therefore, patient variability does not does not outweigh the elemental concentration differences in malignant and normal tissue. We plan to investigate this further in the future using the NSECT technique to analyze the composition of *ex vivo* benign, normal, and malignant tissue specimens.

Dose calculated in this study indicates that the dose from an NSECT scan for cancer detection is only a fraction of the dose delivered from a screening mammogram. The ROC analysis from this simulation study suggests that cancer detection can be achieved with a dose of 0.0224 mSv (2 million incident neutrons). Although the present work calculates the dose from a single projection image, which is not directly comparable to the dose calculated for current high-resolution screening technologies, NSECT shows promise as a low-dose cancer screening technique. We could increase the number of neutrons and still be within dose guidelines, but we used 10 million as the maximum number of incident neutrons for two main reasons. First, it was determined in an earlier study that 10 000 gamma counts are required in the detectors to obtain 5% accuracy.[23] Second, 10 million incident neutrons is a computationally feasible number that provides sufficient statistical accuracy while keeping dose at a minimum. Keeping these two factors in mind, 10 million neutrons were considered optimal for this scan.

The dose value obtained in this study is calculated for a model of the breast that does not account for sources of background, which would otherwise be present in the clinical scanning environment. Before translating this technique to the clinic, an expansion of this study is required to determine the performance when noise is added into the signal. Simulation experiments to model the sources of noise in a clinical environment are currently underway. This study assumes a relatively clean, low-noise signal in detecting an element peak, which results in a low-dose estimate. The presence of noise in the system will raise the detection threshold, requiring a larger total concentration of the element for successful detection. Experiments to determine the detection threshold of NSECT in both simulation and clinical environments are being conducted.

From a detection point of view, a logical extension of this study is to develop a fusion classifier to test whether combining elements could be used to detect differences in normal and malignant breast tissue with greater accuracy at lower neutron fluxes. Another extension would be to perform the same set of simulations using a benign breast tissue model to test NSECT's ability to distinguish malignant from benign breast, which is of clinical interest diagnostically. We are encouraged because our current dose estimate is only a fraction of a standard mammography dose. Thus, there is plenty

of room to increase the dosage to overcome noise and still conduct an NSECT scan that is within clinically acceptable dose limits.

ACKNOWLEDGMENTS

[a] Author to whom correspondence should be addressed. Electronic mail: jeb9@duke.edu

[1] C. E. Floyd *et al.*, "Introduction to neutron stimulated emission computed tomography," Phys. Med. Biol. **51**, 3375–3390 (2006).

[2] C. E. Floyd *et al.*, "Breast cancer diagnosis using neutron stimulated emission computed tomography: Dose and count requirements," in *Proceedings of SPIE Medical Imaging 2006: Physics of Medical Imaging* (SPIE, 2006), Vol. 6142, pp. 597–603.

[3] C. E. Floyd *et al.*, "Neutron stimulated emission computed tomography: Background corrections," Nucl. Instrum. Methods Phys. Res. B **254**, 329–336 (2007).

[4] A. E. Schwartz *et al.*, "Trace elements in normal and malignant human breast tissue," Surgery **76**, 325–329 (1974).

[5] K. H. Ng, D. A. Bradley, L. M. Looi, Mahmood Seman, C. Khalik, and A. Wood, "Differentiation of elemental composition of normal and malignant breast tissue by instrumental neutron activation analysis," Appl. Radiat. Isot. **44**, 511–516 (1993).

[6] S. Rizk and H. Sky-Peck, "Comparison between concentrations of trace elements in normal and neoplastic human breast tissue," Cancer Res. **44**, 5390–5394 (1984).

[7] N. Mussalo-Rauhamaa *et al.*, "Cu, Zn, Se, and Mg concentrations in breast fat of Finnish breast cancer patients and healthy controls," Trace Elements in Medicine **10**, 13–15 (1993).

[8] A. Garg *et al.*, "An elemental correlation study in cancerous and normal breast tissue with successive clinical stages by neutron activation analysis," Biol. Trace Elem. Res. **46**, 185–202 (1994).

[9] M. Yaman *et al.*, "Comparison of trace metal concentrations in malign and benign human prostate," J. Med. Chem. **48**, 630–634 (2005).

[10] E. Andrasi *et al.*, "Concentration of elements in human brain: glioblastoma multiforme," Sci. Total Environ. **139–140**, 399–402 (1993).

[11] K. Geraki, M. J. Farquharson, and D. A. Bradley, "X-ray fluorescence and energy dispersive x-ray diffraction for the quantification of elemental concentrations in breast tissue," Phys. Med. Biol. **49**, 99–110 (2004).

[12] K. H. Ng, D. A. Bradley, and L. M. Looi, "Elevated trace element concentrations in malignant breast tissues," Br. J. Radiol. **70**, 375–382 (1997).

[13] B. Sansoni and V. Iyengar, "Sampling and Sample Preparation Methods for the Analysis of Trace Elements in Biological Materials," Jül-Spez-13, Report KFA Jülich, ISSN 0343-7639 (1978).

[14] CERN. *Geant4*. [cited, Available from: wwwinfo.cern.ch/asd/geant4/geant4.html.

[15] J. E. Bender *et al.*, "The effect of detector resolution for quantitative analysis of neutron stimulated emission computed tomography," in *Proceedings of SPIE Medical Imaging 2006: Physics of Medical Imaging* (SPIE, 2006), Vol. 6142, pp. 1597–1605.

[16] Cross Section Evaluation Working Group, ENDEIB-VI Summary Documentation, Report BNL-NCS-17541 (ENDF-201), edited by P. F. Rose, National Nuclear Data Center, Brookhaven National Laboratory, Upton, New York (1991).

[17] G. Ullman *et al.*, "Implementation of pathologies in the Monte Carlo model in chest and breast imaging," Report 94 (ISSN 11-2-1799, 2003).

[18] C. E. Metz, *ROC analysis software*—ROCKIT. [cited, available from: http://www.radiology.uchicago.edu/krl/KRL_ROC/software_index.htm.

[19] C. E. Metz, B. A. Herman, and J. H. Shen, "Maximum likelihood estimation of receiver operating characteristic (ROC) curves from continuously distributed data," Stat. Med. **17**, 1033–1053 (1998).

[20] J. E. Turner, *Atoms, Radiation, and Radiation Protection*, 2nd ed. (John Wiley & Sons, Inc., New York, 1995).

[21] International Commission on Radiological Protection, *1990 Recommendations of the International Commission on Radiological Protection*, ICRP Publication 60 (Pergamon Press, Oxford, 1991).

[22] J. Law, "The development of mammography," Phys. Med. Biol. **51**, R155–R167 (2006).

[23] A. Kapadia, C. Floyd, C. Howell, and B. Harrawood, "Sampling Requirements for Neutron stimulated emission computed tomography," presented at RSNA, Physics (Digital Imaging, PACS) session, Chicago, Illinois, 2004 (unpublished).

GEANT4 Simulation of an NSECT System for Iron Overload Detection

Anuj J. Kapadia, Amy C. Sharma, Brian P. Harrawood, Georgia D. Tourassi

Abstract– **Hemochromatosis (iron overload in liver) is a condition that causes serious consequences for the patient through an increase in the body's iron stores. Diagnosis of the excess iron, which is often stored in the liver, requires an invasive biopsy. We are developing neutron stimulated emission computed tomography (NSECT) as a non-invasive alternative to measure liver iron concentration to diagnose hemochromatosis. This measurement is performed using an incident neutron beam that scatters inelastically with iron nuclei in the liver, causing them to emit characteristic gamma-rays. An energy-sensitive gamma-ray detector is used to detect these gamma-rays and quantify the iron in the liver. Preliminary experiments have demonstrated an implementation of NSECT to quantify concentrations of iron and potassium in bovine liver tissue. Due to the prohibitive nature of these experiments, it is not feasible to perform system evaluation and optimization at each step using a nuclear accelerator. Here we describe a GEANT4 simulation of NSECT as a feasible alternative to perform system evaluation for iron overload diagnosis using computing resources only. The simulation model uses a 5 MeV neutron beam to scan a human liver phantom with induced iron overload. The liver is modeled as a composite shape combining a half-cylinder and a polyhedron, and is housed in a human torso filled with water. Gamma-ray spectra are generated to show element concentration within the liver. To determine the lower limit of iron overload detection, the concentration of iron in the liver is reduced from an initial high value, and the p-value of detecting peaks corresponding to iron is calculated at each step. The lower limit of detection is defined as the concentration at which the p-value of peak detection exceeds 0.05. The limit of iron overload detection from this simulation was found to be 4 mg/g, which represents a clinically relevant value for iron overload.**

I. INTRODUCTION

HEMOCHROMATOSIS (liver iron overload) is a condition that causes serious consequences for the patient through an increase in the body's iron stores. The excess iron, which is often stored in the liver, can cause extensive tissue damage,

liver cirrhosis, cardiac failure, hepatic failure and hepatocellular carcinoma [1]. Diagnosis of iron overload requires an invasive biopsy [2], which is an unpleasant procedure with several associated complications including death. Neutron stimulated emission computed tomography (NSECT) is being developed as a non-invasive alternative to measure element concentration in the liver to diagnose liver iron overload [3-5]. Preliminary experiments have demonstrated NSECT's potential in quantifying concentrations of iron and potassium in bovine liver tissue [4, 5]. The basic principle of NSECT is as follows: An incident neutron that scatters inelastically with a target atomic nucleus excites the nucleus to a higher energy state. The unstable nucleus then rapidly decays to its ground state, emitting the excess energy as a characteristic gamma-ray. The energy of the emitted photon can be measured by an energy-sensitive gamma-ray detector to identify the atom. This project aims at developing a Monte-Carlo simulation of the NSECT system to investigate NSECT's ability to detect hemochromatosis.

II. MOTIVATION

Experimental investigation of NSECT's detection sensitivity is difficult due to the prohibitive nature of the experiments. Each laboratory experiment requires 7 days of beam time per sample from an accelerator source that is in high demand by a large number of research groups. A simulation environment will allow development and evaluation to continue without access to the nuclear accelerator source. This project aims at determining the limit of detection sensitivity in determining iron overload in the human liver.

III. METHOD

NSECT experiments are performed in the Triangle Universities Nuclear Laboratory at Duke University. A 5 MeV collimated neutron beam is used to scan a target liver sample (usually bovine liver for quantification experiments). The gamma-ray photons emitted by the liver sample are counted by two high purity germanium (HPGe) clover detectors hooked up to a data acquisition system. Data is acquired by illuminating the sample with the beam and counting until sufficient gamma events have been acquired to quantify the element with a p-value ≤0.05. The system has been described in detail elsewhere [3, 6]. A simulation of this setup was implemented in GEANT4 as described below.

GEANT4 is an object-oriented Monte-Carlo programming package that allows modeling of particle interactions with matter over a wide range of energies (meV to GeV) [7]. The simulated model consists of 3 parts – (a) Neutron Source, (b)

Gamma-ray Detectors, and (c) Liver phantom. Each part has been designed as a separate GEANT4 object to facilitate modifying individual parameters on one object independently of the others. Fig 1 shows a complete simulation built by combining each of these components.

A. Neutron Source

The neutron source was created by defining a 'GEANT4 Particle Gun', set to emit 5 MeV neutrons. The gun was placed at the left edge of the world so that every particle exiting the gun entered directly into the world, forming a neutron beam that illuminated the target phantom. The neutron beam was given a 1.6 cm width, similar to that used in the physical experiment.

B. Gamma-ray Detectors

Two gamma-ray detectors were created as solid cylinders with user-defined diameter and height, filled with high-purity germanium (Ge density= 5.32 g/cm3). Detector dimensions for each detector crystal were set to 10 cm diameter and 9 cm height, modeled after each crystal of the clover detectors used in the physical experiment. Four such detector crystals were combined to form one complete clover detector. The detector was sensitized to track particle interactions and record the energy deposited at each interaction, and placed at a backward angle of 135 degrees in the beam plane, mimicking the position of the detector in the physical experiment where a backward angle is used to minimize damage to the detector from forward scattered neutrons. Detector efficiency was modeled by collecting information from all events occurring in the detector and then retaining only a required fraction of these events. For example, for a 60% efficient HPGe detector, 100% of events were recorded, but only 60% of these were used to generate spectral results.

C. Liver Phantom

The liver phantom was made up of two parts - a human torso and a liver phantom housed in the torso. The torso was modeled as an elliptical tube with axes 30 cm x 25 cm, and 11 cm height. The torso phantom was filled with water, to simulate the presence of noise-generating tissue in the human torso. The liver was modeled as a combination of an elliptical tube and a hemisphere to form a complex shape, partially shown in Fig 1. This liver was then placed inside the torso. The composition of the liver was obtained from ICRU report 46 [8] as reported for a healthy human adult, and is shown in Table 1. To simulate iron overload in the liver, the concentration of iron was changed in steps from the initial value of 0 to 25.0 mg/g (approximately 5 times the concentration of clinical hemochromatosis) as shown in table 2. Gamma spectra were generated for each overloaded liver sample, and counts for energies corresponding to iron were identified and summed. A background noise sample was generated by substituting the liver with water and repeating the scan with the same number of neutron counts as used for the liver. The p-value of detecting peaks for iron was calculated using the t-test to compare counts at energies

corresponding to iron with the counts from the water background. The lower limit of detection was defined as the concentration at which the p-value exceeded 0.05.
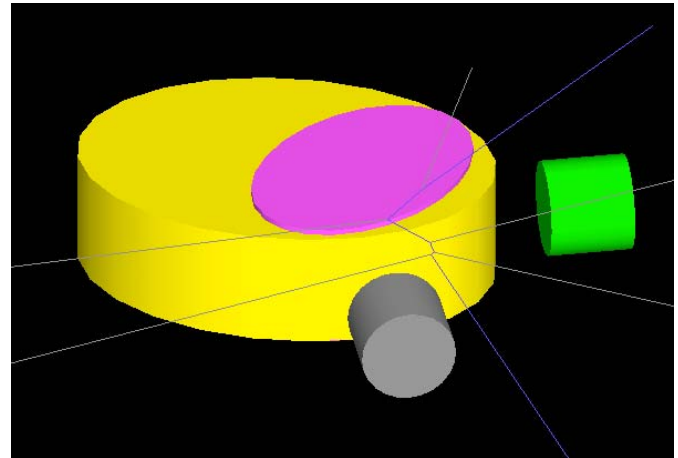
Fig.1. GEANT4 simulation of the NSECT experiment showing the liver (pink) inside an elliptical torso (yellow). Gamma detectors are shown in green and gray. Incident neutrons are shown in blue and scattered particles in gray.

TABLE I
ELEMENTAL COMPOSITION OF THE LIVER PHANTOM (OBTAINED FROM ICRU REPORT 46 [8]).

Element	Normal (%)
O	71.6
C	13.9
H	10.2
N	0.3
P	0.3
S	0.3
K	0.3
Cl	0.2
Na	0.2
Fe	0.0
Density	1.06 g/cm3

IV. RESULTS

Figs. 2, 3 and 4 show the simulated spectrum from the iron overload liver phantom with 25 mg/g, 10 mg/g and 3 mg/g Fe concentration. Energy peaks for ^{56}Fe are observed at 847 keV. Peaks are also seen at energies corresponding to several states in Ge (from the HPGe gamma detectors) and ^{1}H from neutron capture on hydrogen in water (2.22 MeV).

In figs. 2 and 3, the ^{56}Fe peak at 847 keV can be seen clearly above the underlying background as the iron concentration in these phantoms is high (> 10 mg/g). However in fig. 4, the peak corresponding to lower iron concentration (3 mg/g) is not clearly observed above the underlying background.
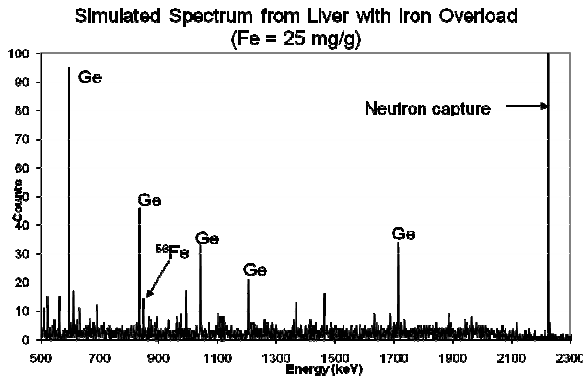
Fig.2. Spectrum corresponding to an iron overloaded liver phantom with 25 mg/g Fe. Peaks are identified for ^{56}Fe, Ge from the detector, and ^{1}H from water in the torso.
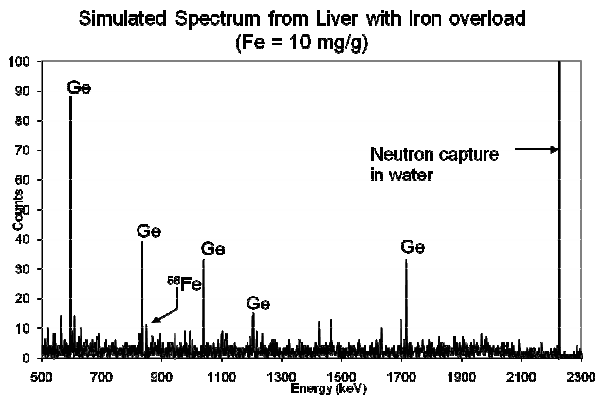
Fig.3. Spectrum corresponding to an iron overloaded liver phantom with 10 mg/g Fe. The peak from ^{56}Fe can be detected above background with $p \leq 0.05$.
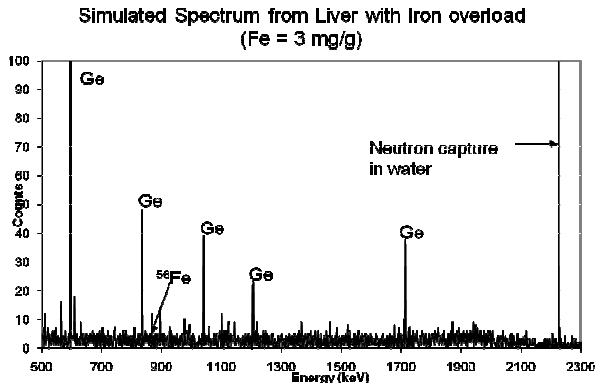
Fig.4. Spectrum corresponding to an iron overloaded liver phantom with 3 mg/g Fe. The peak from ^{56}Fe cannot be detected above background with $p \leq 0.05$.

Table 2 shows the simulated measurement results of the different iron overloaded livers scanned. The p-value of detecting peaks corresponding to iron was seen to decrease with decreasing iron concentration. The lowest concentration of iron corresponding to $p \leq 0.05$ was found to be 4 mg/g Fe.

This concentration was described as the lower limit of detection for the system using the currently available configuration.

TABLE II
SIGNIFICANCE TESTING FOR FE PEAK COUNTS MEASURED IN THE SIMULATED GEANT4 SPECTRA FOR DIFFERENT IRON CONCENTRATIONS.

Fe Conc	t	p-value
25 mg/g	4.12	0.001
10 mg/g	2.40	0.05
5 mg/g	2.24	0.05
4 mg/g	2.06	0.05
3 mg/g	1.89	0.1

V. CONCLUSION AND FUTURE WORK

The simulation developed here presents a feasible and valid alternative to continue evaluation and optimization of NSECT without the use of a nuclear accelerator. Significance testing results demonstrate that NSECT has the potential to detect hemochromatosis in patients with iron concentration as low as 4 mg/g. As clinical iron overload is reported for iron concentrations between 1mg/g to 6 mg/g [1, 2], this value of sensitivity represents a clinically significant concentration. System sensitivity for ^{56}Fe through experimental techniques has been determined as 6 mg/g [6], which demonstrates the validity of this preliminary simulation. While the simulation presented here accounts for the neutron scatter noise generated by the torso, there are several other sources of noise in the experimental system, such as electronic noise in detectors and scatter noise from objects in the experimental area that decrease the overall sensitivity of the system. These sources must be taken into consideration to determine the experimental detection limit for NSECT. Work is underway to model these sources of noise in the simulation.

REFERENCES

[1] L. Powell, "Hemochromatosis," in *Harrison's Principles of Internal Medicine*, 16 ed. vol. 2, D. Kasper, Fawci, AS, Longo, DL, Braunwald, E, Hauser, SL, Jameson, JL, Ed. NY: McGraw Hill, 2005, pp. 2298-2303.
[2] L. W. Powell, "Diagnosis of hemochromatosis," *Semin Gastrointest Dis,* vol. 13, pp. 80-8, Apr 2002.
[3] C. E. Floyd, Jr., J. E. Bender, A. C. Sharma, A. Kapadia, J. Xia, B. Harrawood, G. D. Tourassi, J. Y. Lo, A. Crowell, and C. Howell, "Introduction to neutron stimulated emission computed tomography," *Phys Med Biol,* vol. 51, pp. 3375-90, Jul 21 2006.
[4] A. J. Kapadia, C. E. Floyd, J. E. Bender, C. R. Howell, A. S. Crowell, and M. R. Kiser, "Non-invasive quantification of iron 56-Fe in beef liver using neutron stimulated emission computed tomography," in *IEEE Nuclear Science Symposium, Medical Imaging Conference*, Puerto Rico, 2005, pp. 2232-2234.
[5] A. J. Kapadia, A. C. Sharma, G. D. Tourassi, J. E. Bender, A. S. Crowell, M. R. Kiser, C. R. Howell, and C. E. Floyd, "Non-Invasive Estimation of Potassium (39K) in Bovine Liver Using Neutron Stimulated Emission Computed Tomography (NSECT)," in *IEEE Nuclear Science Symposium, Medical Imaging Conference*, San Diego, CA, 2006, pp. 2076-2078.

[6] A. J. Kapadia, A. C. Sharma, J. E. Bender, G. D. Tourassi, C. R. Howell, A. S. Crowell, M. R. Kiser, B. P. Harrawood, and C. E. Floyd, "Neutron Stimulated Emission Computed Tomography for Diagnosis of Breast Cancer," *IEEE Trans Nuc Sci (in press),* 2007.

[7] V. N. Ivanchenko, "Geant4 toolkit for simulation of HEP experiments," *Nuclear Instruments and Methods in Physics Research Section A,* vol. 502, pp. 666-668, 2003.

[8] ICRU, "Photon, electron, proton and neutron interaction data for body tissues.," International Commission on Radiation Units and Measurements, Bethesda, MD, 46, 1992.

Neutron Stimulated Emission Computed Tomography for Diagnosis of Breast Cancer

Anuj J. Kapadia, Amy C. Sharma, Georgia D. Tourassi, Janelle E. Bender, Calvin R. Howell, Alexander S. Crowell, Matthew R. Kiser, Brian P. Harrawood, Ronald S. Pedroni, and Carey E. Floyd, Jr.

Abstract—**Neutron stimulated emission computed tomography (NSECT) is being developed as a non-invasive spectroscopic imaging technique to determine element concentrations in the human body. NSECT uses a beam of fast neutrons that scatter inelastically from atomic nuclei in tissue, causing them to emit characteristic gamma photons that are detected and identified using an energy-sensitive gamma detector. By measuring the energy and number of emitted gamma photons, the system can determine the elemental composition of the target tissue. Such determination is useful in detecting several disorders in the human body that are characterized by changes in element concentration, such as breast cancer. In this paper we describe our experimental implementation of a prototype NSECT system for the diagnosis of breast cancer and present experimental results from sensitivity studies using this prototype. Results are shown from three sets of samples: (a) excised breast tissue samples with unknown element concentrations, (b) a multi-element calibration sample used for sensitivity studies, and (c) a small-animal specimen, to demonstrate detection ability from *in-vivo* tissue. Preliminary results show that NSECT has the potential to detect elements in breast tissue. Several elements were identified common to both benign and malignant samples, which were confirmed through neutron activation analysis (NAA). Statistically significant differences were seen for peaks at energies corresponding to ^{37}Cl, ^{56}Fe, ^{58}Ni, ^{59}Co, ^{66}Zn, ^{79}Br and ^{87}Rb. The spectrum from the small animal specimen showed the presence of ^{12}C from tissue, ^{40}Ca from bone, and elements ^{39}K, ^{27}Al, ^{37}Cl, ^{56}Fe, ^{68}Zn and ^{25}Mg. Threshold sensitivity for the four elements analyzed was found to range from 0.3 grams to 1 gram, which is higher than the microgram sensitivity required for cancer detection. Patient dose levels from NSECT were found to be comparable to those of screening mammography.**

Index Terms—**Breast cancer detection, gamma-ray spectroscopy, neutron, NSECT, tomography.**

A. J. Kapadia and A. C. Sharma are with the Department of Biomedical Engineering and the Duke Advanced Imaging Laboratories (DAILabs), Department of Radiology, Duke University, Durham, NC 27710 USA (e-mail: anuj.kapadia@duke.edu; anc4@duke.edu).

G. D. Tourassi and B. P. Harrawood are with the Duke Advanced Imaging Laboratories (DAILabs), Department of Radiology, Duke University, Durham, NC 27710 USA (e-mail: gt@deckard.duhs.duke.edu; brian.harrawood@duke.edu).

J. E. Bender is with the Department of Biomedical Engineering, Duke University, Durham, NC 27710 USA (e-mail: janelle.bender@duke.edu).

C. R. Howell, A. S. Crowell, and M. R. Kiser are with the Department of Physics, Duke University, Durham, NC 27710 USA and also with Triangle Universities Nuclear Laboratory, Durham, NC 27708 USA (e-mail: howell@tunl.duke.edu; crowell@tunl.duke.edu; kiser@tunl.duke.edu).

R. S. Pedroni is with the Department of Physics, North Carolina A&T State University, Greensboro, NC 27411 USA.

C. E. Floyd Jr. is with Duke Advanced Imaging Laboratories (DAILabs), Department of Radiology, Duke University Medical Center and also with the Department of Biomedical Engineering Duke University, Durham, NC 27710 USA.

Color versions of one or more of the figures in this paper are available online at http://ieeexplore.ieee.org.

Digital Object Identifier 10.1109/TNS.2007.909847

I. INTRODUCTION

NEUTRON techniques are rapidly evolving as methods of measuring trace element concentrations in the human body [1]–[6] and in animal tissue [7], [8]. We have successfully implemented a tomographic non-invasive *in-vivo* imaging technique called Neutron Stimulated Emission Computed Tomography (NSECT) to obtain two-dimensional tomographic information about element concentration within a target tissue sample [9]–[17]. NSECT uses spectral information obtained from inelastic scattering interactions between neutrons and atomic nuclei in the target sample to identify the target atoms and determine their concentration *in-vivo*.

Such a technique has several potential applications in both humans and small animals. Several studies have indicated that changes in trace element concentrations in human tissue may be a precursor to malignancy in several organs, for example, brain, prostate and breast [1], [5], [6], [18]–[20]. Measuring these concentration changes would provide the ability to differentiate between malignant and benign tissue, and their quantification could enable *in-vivo* cancer diagnosis at very early stages. Element concentration changes have also been observed in iron for diseases such as sickle cell anemia, thalassemia major, hemosiderosis and hemochromatosis [21]–[27], and in copper for Wilson's disease [28]. NSECT has the potential to image element concentrations in tomographic regions of interest within affected organs, which can help in diagnosis and management of these disorders.

The underlying NSECT principle is the following. NSECT relies on inelastic scattering interactions that occur when atomic nuclei are bombarded with fast neutrons. When an incident neutron scatters inelastically with a target atomic nucleus, the nucleus gets excited to one of its quantized higher-energy states which is often unstable. This excited nucleus then rapidly decays to a lower state, emitting a gamma ray photon whose energy is equal to the difference between the energies of the two states. These non-overlapping energy states are well established and somewhat unique to each element and isotope. Thus, detection and analysis of the emitted gamma energy spectrum can be used to identify the emitting target atom.

While the NSECT technique may seem somewhat similar to prompt gamma neutron activation analysis (PGNAA) as gamma rays emitted due to interactions with incident neutrons are measured simultaneously while irradiating the sample, the two techniques differ greatly in the method of gamma ray production. PGNAA relies on neutron capture with prompt gamma emission, while NSECT uses inelastic scatter spectroscopy to identify the scattering isotope without inducing radioactivity. The NSECT technique is a computed tomography extension of neutron inelastic scatter spectroscopy.

Emitted gamma photons are captured using an energy-sensitive gamma-ray detector. Tomography is performed by acquiring a complete set of projections of line integrals using the translate-rotate configuration as in first generation CT scanners, i.e. the beam is translated horizontally through the entire sample length, then the sample is rotated through some fixed angle and the process is repeated. This tomographic scanning technique yields a two-dimensional map of element concentration and distribution within the sample. This translate-rotate geometry is appropriate for initial proof of concept studies using phantoms, specimens or small animals. Once feasibility is demonstrated, other geometries can be used in future clinical systems. Images are reconstructed using the Maximum Likelihood Expectation Maximization algorithm, an iterative technique to optimize an image reconstructed from a finite set of its projections [29]–[31].

This manuscript presents NSECT as a potential application for diagnosis of breast cancer. Early detection has proven to be the most effective technique to increase survival rates of patients with breast cancer. While screening mammography has been proven to be effective in screening for breast cancer, it suffers from the following limitations: (a) it requires that the mammograms have good contrast, which is often difficult to achieve in dense breasts; (b) its anatomic approach in trying to identify abnormalities in mammograms makes it essential that the abnormality be in an advanced stage of development; and (c) it has limitations in classifying detected abnormalities as benign or malignant. NSECT's sensitivity to metabolic changes seen in malignant tumors in very early developmental stages has the potential to overcome the disadvantages of screening mammography.

Several studies have demonstrated that breast cancer is associated with changes in trace element concentration in the malignant tissue at very early stages. These changes have been observed in concentration of elements such as Al, Br, Ca, Cl, Co, Cs, Cu, Fe, K, Mn, Na, Rb, Sb, Se and Zn, and often occur much earlier than morphologic changes such as tumors and calcifications begin to appear [1], [6], [18]–[20], [32]. Quantifying these element concentrations could potentially enable diagnosis of breast cancer much before the tumor grows large enough to be detected by existing imaging techniques. Generally, NSECT's role in diagnosing breast cancer is to (i) spectroscopically quantify the concentration of elements of interest in the tissue to diagnose the disorder, and (ii) generate three dimensional tomographic image of the element concentration in the organ to isolate the region affected by the disorder. As most of these trace elements occur in the body in microgram quantities, a primary

objective of this study is to determine whether NSECT has the required sensitivity to detect micro-gram concentration changes *in-vivo*.

In this paper we describe our experimental implementation of a prototype NSECT system for the diagnosis of breast cancer and present experimental results from sensitivity studies using this prototype. This manuscript presents the first results from a spectroscopic examination of the breast as a preliminary step in determining whether it is realistic to develop NSECT for diagnosis of breast cancer in a clinical scenario.

II. MATERIALS AND METHODS

A. Description of NSECT Prototype System

NSECT experiments have been performed at the Triangle Universities Nuclear Laboratory (TUNL) accelerator lab located at Duke University. TUNL is a low energy nuclear physics research laboratory with a variety of ion beam sources and a 10 megavolt tandem Van de Graaff accelerator capable of producing 20 MeV proton or deuteron beams and a host of other light ion beams. The shielded neutron source provides researchers with an intense pulsed collimated mono-energetic neutron beam. The shape and cross sectional dimension of the beam can be selected with collimator inserts in the 1.5 meter thick shielding wall. For instance, beams with rectangular cross sections are available with sides ranging from 1 mm to 60 mm. The reduction in the background by the 1.5 meter thick wall is sufficient to permit gamma-ray detectors to be used without extensive shielding. The key NSECT components are described below.

1) Neutron Source: Neutrons are produced through the $^2H(d, n)^3He$ reaction by directing an accelerated and pulsed beam of deuterons onto a deuterium gas target. Deuterons are accelerated to energies between 3 and 20 MeV by the tandem Van de Graaff accelerator. The charged deuteron beam is directed onto a pressurized deuterium gas cell located behind a 1 meter thick shielding wall composed of concrete, steel, lead, and paraffin loaded with boron and lithium. Beam positioning and focusing on target are performed using magnetic steering coils and magnetic quadrupole lenses, respectively. A collimated channel made of copper with swappable inserts is used to select the beam profile. Copper is chosen because it adequately attenuates neutrons at energies available at TUNL, is fairly simple to machine and is reasonably low cost. For this experiment, the beam profile was selected to be cylindrical with 6 cm diameter.

The neutron beam created is highly peaked in the forward direction and has a narrow energy width of approximately 1 MeV. Neutron beam energies between 5 and 23.2 MeV are available at TUNL.

The beam is pulsed to provide 2 ns wide bunches at the target to allow measurement of neutron and gamma time of flight (TOF), enabling TOF background correction. The repetition rate of the beam pulses is adjustable from 2.5 MHz down to 39 kHz. This pulsed neutron beam allows researchers to measure the background simultaneously with the foreground.

2) Neutron Flux Monitors: After exiting the collimator channel, the beam is incident on a thin neutron flux monitor made of a 1.6 mm thick plastic scintillator attached to a
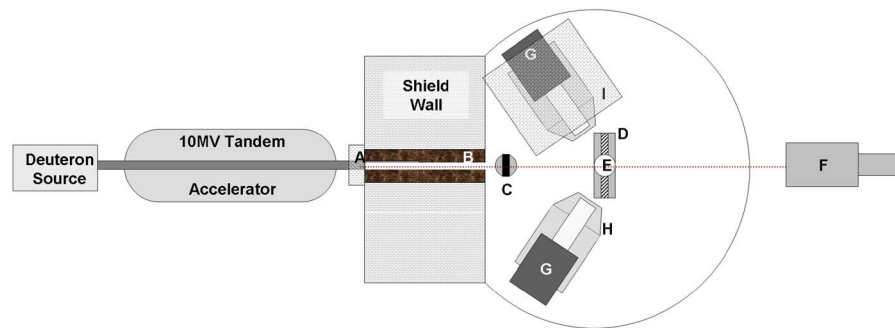
Fig. 1. Schematic drawing of the experimental setup used in NSECT measurements. Components are labeled as follows: A—Deuterium Gas Cell; B—Copper Collimator; C—Neutron Flux Monitor; D—Sample Manipulator; E—Sample; F—Zero-degree Liquid Scintillator Detector; G—HPGe detector; H—Anti-coincidence Compton Shield; I—Detector Shielding Enclosure.

photomultiplier tube. The attenuation of neutrons by the flux monitor in the energy range of our studies is less than 0.1%. The threshold setting on the discriminator of the flux monitor is set sufficiently high to reject more than 90% of the pulses due to recoil electrons from Compton scattering of gamma rays. The efficiency of the thin flux monitor is calibrated relative to a liquid scintillator detector positioned at 0 degrees with respect to the beam. This detector has an active volume 5 inches diameter $\times$ 0.74 inches thick and is filled with Bicron Corporation's BC519 scintillator fluid that enables gamma-ray rejection by pulse shape analysis. The absolute efficiency of this detector has been determined in a separate measurement to an accuracy of $\pm 5\%$ [33]. The zero degree liquid scintillator detector is also used to obtain the neutron transmission image of the sample which is required to make attenuation corrections.

3) Sample Manipulator: A computer-controlled sample holder allows precise horizontal, vertical and rotational positioning of small samples remotely. This holder allows tomographic acquisition by translating and rotating the sample with respect to the neutron beam. In the current implementation, tomography is performed by using the translate-rotate geometry to obtain a complete set of projections of line integrals through a slice of the sample. For NSECT, these projections are defined by the angular and spatial sampling intervals between successive positions of the sample as positioned by the sample manipulator.

4) Gamma Detectors: Two high-purity germanium (HPGe) detectors are used to detect gamma rays emitted from the sample. These detectors are the 2-Fold Segmented Clover Detectors (CLOVER $4 \times 50 \times 80$ SEG2) manufactured by Canberra Eurysis S.A. Each detector consists of four co-axial n-type germanium crystals mounted together in the shape of a 4-leaf clover. Each germanium crystal is 50 mm in diameter and 80 mm in length, with minimum relative efficiency of 22% and full width at half maximum less than or equal to 2.25 keV for 1.332 MeV gamma rays of ^{60}Co. Both detectors were calibrated against known energy peaks from a ^{22}Na source and positioned at ± 135 degrees from the incident neutron beam at a distance of 20 cm from the sample. A majority of the states of interest decay by an electric quadrupole transition whose distribution has a maximum intensity at about 45 and 135 degrees. Using the 135 degree orientation helps prevent the gamma detector from being illuminated by either the direct neutron beam or by neutrons that elastically scatter from the

target. Active Compton shielding is used to reduce the effects of Compton scattering in the detectors. These shields have a minimum peak-to-Compton ratio of 41 for ^{60}Co gamma rays at 1.332 MeV.

A schematic drawing of the source, detector and shielding configuration is shown in Fig. 1.

5) Passive Shielding: The gamma detector is shielded from the neutron source by a 1.5 m thick wall composed of concrete, steel, lead, borated plastic and lithium-loaded paraffin. In addition to this wall, an enclosure of lead bricks and lithium-loaded paraffin built around each detector provides additional shielding to further reduce particles incident on the active area of the detector.

6) Computers and Acquisition Software: Data is acquired using SpecTcl, a nuclear event data acquisition and analysis software package developed at the National Superconducting Cyclotron Laboratory at Michigan State University. SpecTcl allows acquisition and storage of raw data using an object oriented C++ framework, and allows online and offline data visualization through the Xamine display program. Complete as well as partial sets of raw data can be retrieved at any time, including during acquisition, and analyzed using any combination of data parameters. The Xamine display program allows simultaneous display of multiple spectra including spectrum overlay.

7) Amplifiers: Canberra 2026 spectroscopy amplifiers are used to integrate and shape the signals from the gamma detectors before they are digitized by peak-sensing ADC's at the data acquisition interface. Adjustable gain settings on these amplifiers allow 'zooming' in or out on a specific range of nuclear energy levels. For example, acquiring data for a gamma energy range of 0–2 MeV would require double the gain as that for 0–4 MeV. However, as the number of channels in the ADC is finite, focusing the entire range of the ADC into a smaller energy range gives better energy resolution in the measured gamma ray energy spectrum. This feature is important when looking for specific energy peaks from certain elements, which lie close to energy peaks from other elements, as in the case of iron (56Fe at 846.7 keV) and germanium (74Ge at 841.1 keV).

B. Spectral Acquisition Methodology

Spectral acquisition for samples was performed by using SpecTcl to digitize two measurable quantities for each gamma count observed: gamma TOF and gamma photon energy. For each data acquisition run, several quantities were counted

using scalars and recorded. These scalars include neutron flux, accelerator beam current and the zero-degree monitor counts. For tomography, the sample position was recorded by reading the sample manipulator's x,y,z positions at each projection as the sample was translated and rotated. Each projection was then analyzed separately and results were fed to the reconstruction algorithm. Data were recorded for each projection until a statistical accuracy of 95% was obtained.

Recorded data sets could be retrieved and analyzed in both real-time while acquiring data as well as at a later time for off-line analysis. Analysis parameters such as TOF windows and detector calibration bias were applied and adjusted in software to allow replaying the experiment with different windows for off-line optimization of these parameters. Spectra were generated using the Xamine display program with different combinations of timing and energy windows applied to the acquired data.

1) Background Reduction: Background reduction was performed to account for three contributing sources of background: time uncorrelated events via a TOF background suppression technique [34], [35], sample uncorrelated backgrounds that are time correlated by a sample-out scan subtraction [35], and polynomial curve-fitting of the residual background, i.e. the background that remains after the measured contributions are subtracted. [13]–[15]. The TOF suppression technique is used to correct for the time-uncorrelated backgrounds that are due mostly to gamma rays created and noise generated from the neutron interactions in the shielding material and target apparatus. This technique uses a pulsed neutron beam to allow selection of gamma rays which appear within the prompt peak that corresponds to the time of flight for a neutron from the source to the sample plus the time of flight for the subsequently emitted gamma from the sample to the detector. The remaining gamma rays are suppressed as 'background noise'. The time zero for the TOF measurement is set by using pulsing information from the deuteron beam to control a clock that measures the time of flight of the neutrons from the gas cell to the sample plus the time of flight of the emitted gamma rays from the sample to the detector. Our implementation of this technique has been described in detail elsewhere [35].

Background events that are due to processes that don't involve the sample are measured by acquiring data with the sample removed. Examples of such processes are interactions of neutrons with the collimator or sample holder. This data is subtracted from the sample-in data to produce an estimate of the spectrum due to neutron interactions in the sample. This technique has been described in detail elsewhere [35]. In this study, the samples of interest were only the elements present in the tissue. Hence, the sample-out scan was acquired by substituting the tissue sample with an equivalent mass of water, i.e. removing only the elements of interest while retaining the neutron scatter properties of hydrogen and oxygen nuclei in tissue.

Polynomial curve fitting is used to remove residual background due to Compton scattering of detected gammas. When high energy gamma photons are incident on a detector, some of
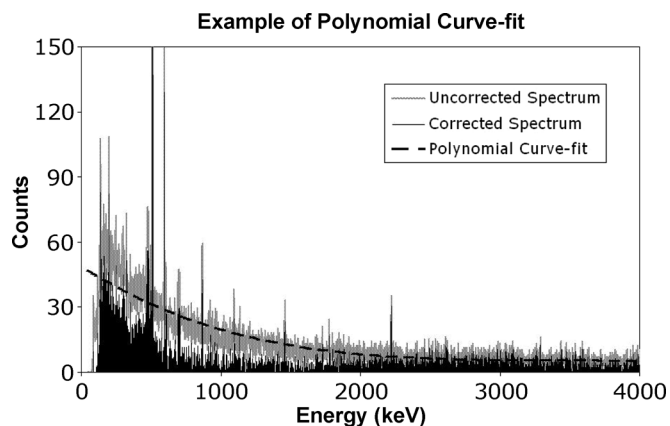
Fig. 2. Example of polynomial curve-fitting for residual background correction. The uncorrected spectrum is shown in grey with the polynomial curve overlaid in dotted black. The resulting corrected spectrum is shown in the foreground as a solid black line in the lower part of the image.

the gammas will deposit their full energy in the detector while others will scatter out of the detector active volume. As a result, there is a trend of increasing counts in the lower energy channels of the detector. A polynomial curve-fit is used to model this trend and subtract this residual background.

An example of this is shown in Fig. 2, which shows an original uncorrected spectrum (light gray), the polynomial curve fit to underlying background (dotted black line), and the spectrum after residual background correction (solid black line in the lower part of the image).

2) Samples: A total of 5 samples were scanned for this study investigating our ability to use NSECT to detect element concentration changes in human tissue. Samples I and II comprised breast biopsy tissue samples with matched tumors excised from the same patient. Sample I had a benign tumor and Sample II was malignant. Each sample weighed approximately 40 g and was scanned with a 6.0 MeV neutron beam while placed in a plastic container, delivering an integrated dose of approximately 1 mSv. Sample III comprised 40 g of distilled water in an identical plastic container, and was used to get an estimate of sample related background originating mainly from hydrogen and oxygen nuclei in tissue cells. Sample IV was made of varying concentrations of ^{56}Fe, ^{23}Na, ^{39}K, ^{35}Cl and ^{37}Cl in distilled water and was used as a calibration sample to determine the lower detection threshold of NSECT. Finally, as none of the above samples were of *in-vivo* tissue, Sample V comprising a fixed mouse specimen was scanned to demonstrate NSECT's ability in detecting elements from an intact biological specimen. The mouse specimen was prepared as follows. A freshly sacrificed mouse was flushed with saline and then fixed for one week using a 1:10 gadolinium/formalin solution. After flushing the fixed mouse with saline once again, it was enclosed and sealed in a glass tube along with diluted formalin solution. This enclosed specimen was scanned for 95 minutes with a 5.0 MeV monochromatic neutron beam.

Gamma spectra obtained from each sample were normalized against neutron flux monitor counts for the duration of the scan and corrected for sample uncorrelated backgrounds.

C. Spectral Analysis Methodology

After correcting for sample uncorrelated backgrounds, each spectrum was analyzed to identify the location of a peak using an automated peak-finding algorithm. The algorithm identifies a peak as a region of high intensity within a pre-specified energy window and peak height above a certain pre-specified threshold [36]. For the breast spectra in this experiment, the energy window width was defined as ± 10 keV and peak height threshold was set to 7. Each detected peak was compared to its underlying background using a z-score test for difference of means. Collection of gamma rays in the detectors is assumed to follow Poisson counting statistics, where, for each energy peak, the mean and variance are equal to the number of counts in the peak. With this assumption, the statistical significance for any two energy peaks can be calculated using the z-score test for a difference of means. Peaks with a two-tailed p-value ≤ 0.05 are considered significant. For each energy peak in the spectrum, an underlying background was calculated using a polynomial curve-fit as described earlier. The significance of the energy peak was determined by calculating the value of z as shown in (1), comparing the counts in the energy peak against counts in the underlying background

$$z = \frac{\mu_{peak} - \mu_{background}}{\sqrt{\mu_{peak} + \mu_{background}}}. \tag{1}$$

Only peaks detected with a 95% confidence level (i.e., two-tailed p-value ≤ 0.05) were reported for element matching. This analysis was performed separately for the benign and malignant breast spectra.

Each reported peak was then matched with potential elements using the National Nuclear Data Center's Nuclear structure and decay data online tool (NuDat 2.3) [37]. This identification was made in three steps: (a) a list of all elements with gamma lines at the energy peak of interest were listed; (b) isotopes of elements not expected to be present in the breast, including radioactive isotopes and stable isotopes with low abundance, were discarded from the list; (c) prior information about the remaining isotopes' line contributions to prominent gamma lines was used to identify a possible element match. Several elements such as ^{12}C, ^{40}Ca, ^{35}Cl ^{63}Cu, ^{56}Fe and, ^{16}O, which are present in the breast, have been scanned and studied in earlier NSECT experiments where several of these elements were scanned individually [9]–[11]. These individual element scans were used to experimentally establish the relative contribution of prominent gamma lines for each of these elements. This prior information was used in identifying the corresponding element in the breast spectra. However, there are many other elements in the breast spectrum that have not yet been scanned individually, and their contributions to different gamma lines have not been experimentally established. As a result, certain gamma energy peaks in the breast spectra were found to have multiple element matches, and these are labeled accordingly.

After identifying energy peaks in the individual spectrum, a z-score test for the difference of means was used to analyze the comparative differences in peak heights between the benign and malignant spectra. Counts in an energy peak identified as a potential element peak in a benign spectrum were compared

Fig. 3. Gamma energy spectrum from benign breast sample showing energy peaks for several potential elements identified. Gamma peaks are seen for ^{72}Ge and ^{74}Ge from the germanium detector. Peaks with multiple potential element matches are labeled accordingly.

to counts from the same energy peak in the malignant spectrum using the formula in (1). Each peak was considered individually for this analysis. Energy peaks that differed from each other at the 95% confidence level (i.e. two-tailed p-value ≤ 0.05) were reported as possible markers for malignancy.

For the multi-element calibration sample, prominent peaks corresponding to ^{56}Fe, ^{39}K, ^{23}Na and ^{35}Cl were identified in the spectrum, taking into consideration prior information about their line contributions to the peaks, and the intensity of their peaks was associated with the known concentration of the element in the sample. Assuming the statistical noise in the system to remain constant, threshold sensitivity for each element was calculated as the concentration at which the resulting peak could be detected with two-tailed p-value ≤ 0.05 above its underlying background using the z-score test for difference of means.

III. RESULTS

The results below show sample-uncorrelated background corrected spectra from each of the samples scanned except for Sample III, which was used to estimate background.

Fig. 3 and Fig. 4 show background corrected spectra from the benign and malignant tumor samples respectively. Several elements were identified common to both samples. Energy peaks were seen for Ag, Br, Cl, Co, Cr, Cs, Cu, Fe, Mg, Mn, Ni, Rb, Se, and Zn. Energy peaks were also seen for Ge from the gamma detectors. While several gamma energy peaks were seen to vary in intensity between the two samples, statistically significant differences were observed for the peaks listed in Table I. These peaks were found to correspond to Al, Br, Cl, Co, Fe, K, Rb and Zn.

Both breast samples were sent for spectral examination through neutron activation analysis (NAA). Results from the NAA indicated significant increases in the concentration of Cl, Fe, K, Na, and Zn and is shown in Table II.

Fig. 5 shows the gamma spectrum from the mixed Fe-Na-K-Cl sample containing 5 g Fe, 0.98 g Na, 1.31 g K, and 2.71 g Cl. Peaks were seen for each of the elements present in the sample. Assuming the statistical noise in the system to remain constant, the detection threshold for NSECT was calculated for each element and is shown in Table III.
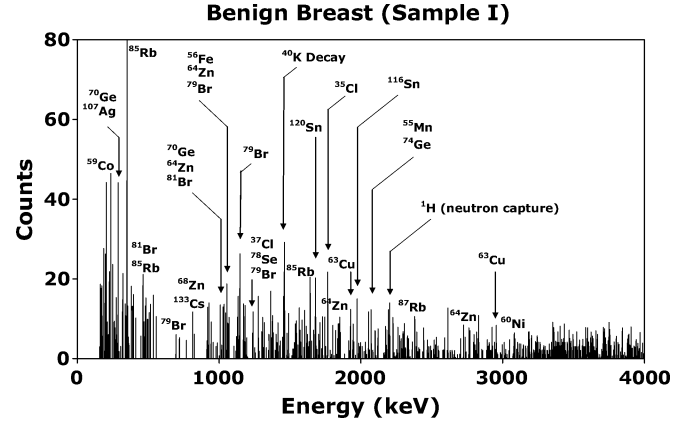
Fig. 4. Gamma energy spectrum from malignant breast sample showing energy peaks for several potential elements identified. Gamma peaks are seen for ^{72}Ge and ^{74}Ge from the germanium detector. Peaks with multiple potential element matches are labeled accordingly.

TABLE I
LIST OF ENERGY LEVELS SHOWING STATISTICALLY SIGNIFICANT DIFFERENCES IN INTENSITIES BETWEEN BENIGN AND MALIGNANT SPECTRA ALONG WITH A LIST OF POTENTIAL MATCHING ELEMENTS. ELEMENTS WITH NEGATIVE DIFFERENCES SHOWED A DECREASE IN CONCENTRATION IN THE MALIGNANT SAMPLE. THE STATISTICAL SIGNIFICANCE WAS CALCULATED USING A z-SCORE TEST FOR DIFFERENCE OF MEANS

Energy keV	Element Match	Counts Benign	Counts Malignant	Diff	p-val
219	^{79}Br	6	19	13	0.01
397	^{59}Co, ^{79}Br	16	2	-14	0.01
1028	^{81}Br	13	29	16	0.05
1128	^{39}K, ^{68}Zn	0	13	13	0.001
1306	^{56}Fe	10	0	-10	0.01
2299	^{27}Al	0	13	13	0.001
2469	^{37}Cl, ^{56}Fe, ^{66}Zn	5	15	10	0.05
3635	^{35}Cl	3	14	11	0.01

TABLE II
LIST OF ELEMENTS SHOWING STATISTICALLY SIGNIFICANT DIFFERENCES IN CONCENTRATION BETWEEN BENIGN AND MALIGNANT TISSUE DETERMINED THROUGH NAA

Element	Cl	Fe	K	Na	Zn
Benign (µg/g)	2170	<172	<507	1440	3.96
Malignant (µg/g)	4000	902	834	3110	13.1

Fig. 6 shows the gamma energy spectrum accumulated for the fixed mouse specimen. Gamma peaks were observed for several elements expected from the mouse specimen as well as some from materials present in the scanning setup. Energy peaks were identified for ^{12}C from tissue, ^{40}Ca from bone, and elements ^{39}K, ^{27}Al, ^{37}Cl, ^{56}Fe, ^{68}Zn and ^{25}Mg which could be present in the specimen. Elements ^{27}Al and ^{56}Fe could also be system dependent as many components used to mount the detectors and other hardware were made of aluminum and iron. Peaks were seen for ^{158}Gd and ^{160}Gd from the 1:10 gadolinium/formalin fixing solution in the sample, along with peaks from several naturally occurring states in germanium in the HPGe detectors.

Fig. 5. Gamma energy spectrum from a mixed sample of 2.5 g KCl, 2.5 g NaCl and 5 g Fe in 40 g H_2O. Peaks are seen for each of the elements in the sample.

TABLE III
RESULTS OF SENSITIVITY ANALYSIS FOR THE MULTI-ELEMENT CALIBRATION SAMPLE. ALSO LISTED FOR A COMPARATIVE ANALYSIS IS THE CORRESPONDING NAA SENSITIVITY FOR THE ELEMENT

	Mass	Peak	Threshold	Sensitivity	
	(g)	counts	counts	NSECT (g)	NAA (µg)
^{23}Na	0.98	140.21	40	0.28	5
^{56}Fe	5	519.79	72	0.69	90
^{39}K	1.31	71.47	32	0.59	1000
^{35}Cl	2.71	52.46	19	0.98	20

Fig. 6. Gamma energy spectrum from a formalin fixed mouse specimen showing peaks corresponding to excited states in various elements. Gamma peaks are seen for ^{12}C (escape peaks), ^{40}Ca, ^{39}K, ^{27}Al, ^{37}Cl, ^{56}Fe, ^{68}Zn and ^{25}Mg. Gamma peaks are also seen for ^{72}Ge and ^{74}Ge from the germanium detector, and ^{158}Gd and ^{160}Gd from the fixing solution. Peaks with multiple potential element matches are labeled accordingly.

IV. DISCUSSION

This work demonstrates that NSECT shows significant potential in developing into a modality capable of detecting breast cancer in early stages. Results from preliminary scans of breast tissue samples demonstrate its ability to detect individual elements within breast tissue. Energy peaks seen to vary in intensity between the benign and malignant samples facilitate future hypothesizing of these peaks as potential markers of breast cancer. Although the spectra obtained in this study were from

excised tissue, results from the whole mouse specimen indicate that element detection is possible for *in-vivo* tissue without the need for biopsy. The lower detection threshold for accurate quantification of an element using this preliminary NSECT system was found to range from 0.28 grams to 0.98 grams for the four elements analyzed. This threshold value is much higher than the microgram sensitivity required to detect cancer-indicating trace elements in the breast. Accurate element quantification using the current NSECT system requires at least the threshold concentration of the target element to be present in the beam. However, simulation experiments conducted to test the feasibility of breast cancer detection for *in-vivo* tumors have demonstrated the ability to detect microgram concentrations of trace elements that are markers of breast cancer for tumors that are *in-vivo* [36]. In some cases, it may be possible to increase the total mass of the element in the beam by using a broad neutron beam to illuminate a larger volume of the sample. Generally, a significant sensitivity improvement will be required in order to facilitate breast cancer diagnosis. Efforts are under way to improve sensitivity while maintaining the lowest possible dose level delivered to the patient. Using high-flux neutron sources and multiple gamma detectors will increase the overall detection efficiency and reduce scan time, which will both in turn reduce the time-dependent background noise. Optimizing the detector shielding will reduce the sample-related and room-related background, which will increase signal to noise ratio and improve the sensitivity of the system. Increasing the gamma detection efficiency to reduce overall scan time will also reduce the associated patient dose. Neutron and gamma attenuation correction algorithms are being developed and implemented simultaneously to improve sensitivity and detection accuracy [38].

Three background correction techniques were used in this experiment, TOF correction, sample-related background subtraction, and polynomial curve-fitting. The TOF correction technique is used to reduce the time-uncorrelated backgrounds. This background can also be estimated by acquiring a spectrum from a sample-out scan. Both techniques have been tested and are seen to suppress time-uncorrelated background sufficiently. We prefer to implement the TOF subtraction technique here because not only does it require less time by not having to acquire a separate sample-out scan, but the electronics are also readily available at TUNL. In a clinical environment however, it may be easier to use the sample-out subtraction technique to avoid the added complexity in required hardware.

Slowing and attenuation of neutrons in the body depends largely on the concentration of hydrogen and oxygen nuclei in the sample, and is of significant concern when interrogating large samples such as the abdomen. However, for the size of tumor samples that have been used in this study, simulations have shown that neutron slowing is not of significant concern. As larger samples are interrogated, neutron slowing and attenuation will be corrected in one of two ways: (a) Neutron energy slowing: Incident neutrons lose a part of their energy through interactions with nuclei encountered in the sample while traveling towards target trace element nuclei. As a result, the energy of the neutron available to interact with the target nucleus is lower. As the criterion for successful interrogation of a target nucleus through inelastic scatter spectroscopy is that the energy of the incident neutron must be larger than the target nuclear energy level to be excited, the reduction in energy

through slowing of neutrons is taken into consideration when selecting the original incident energy of the neutron beam. For example, to interrogate a sample containing ^{12}C with its first excited state at 4.4 MeV, a 5 MeV neutron beam is used to ensure that there will be sufficient energy left to excite the 4.4 MeV energy state even after minor energy losses through slowing. (b) Neutron attenuation: Interactions such as elastic scatter between incident neutrons and nuclei encountered while traveling towards target trace elements often result in a change in direction of the incident neutron. As a result, fewer neutrons are able to reach the target trace element nucleus, leading to a reduction in the number of observed gamma counts for that nucleus. For spectroscopic examination of a homogeneous sample, this neutron attenuation is accounted for by using a calibration sample with the same geometric dimensions as the target tissue sample. For non-homogeneous samples which require tomographic examination, a neutron attenuation-correction algorithm has been developed for use with NSECT and has been described elsewhere [38].

Using neutrons as the incident radiation leads to significant concerns about patient dose. At our energies of interest (2 MeV to 8 MeV), neutrons are known to damage the body 10 times more than x-rays. However, as it takes fewer neutrons to create an NSECT image than x-rays required to create a mammogram, it is possible to maintain patient dose level at values comparable to other ionizing radiation modalities. In previous studies, it has been established that only 10,000 gamma events are required in the detectors to obtain quantitative accuracy of 95% in a tomographic image. Geant4 simulations to evaluate the efficiency of inelastic scatter interactions have shown that 10,000 gamma events can be obtained in the detectors using 10 million incident neutrons, which corresponds to an effective patient dose of less than 1 mSv. Our preliminary simulation experiments suggest that for breast cancer detection, it may be possible to achieve effective patient dose levels lower than 5 mSv [36], [39]. By increasing the number of detectors and using high-flux neutron sources to reduce scan time, dose levels can potentially be brought down even further. Dose assessments are currently performed through a Geant4 simulation which models the acquisition geometry, neutron beam characteristics and tissue sample data [39]. The simulation is used to count the energy deposited in the tissue sample from which an effective dose equivalent for the organ can be calculated by using the appropriate weighting factors for the organ of interest. For the breast, the weighting factor relative to whole body exposure is 0.05.

An important issue to address for breast cancer diagnosis using NSECT is the accurate quantification of a particular element in the spectrum despite line contributions to its gamma peaks from other elements. This involves an understanding of the nuclear transition structure of the element under evaluation, and subsequent correction for the 'noise' line-contributions from other elements. These line contributions have been evaluated experimentally for several samples. Before quantification experiments can be performed for micro-gram concentrations of breast trace elements, it is imperative to analyze the line contributions from each of the elements of interest and develop a model to identify an element based on its gamma line contributions throughout the spectrum. Efforts are under way to evaluate gamma spectra from several such elements using Geant4 simulation.

NSECT is a new alternate diagnosis method with the potential to detect breast cancer. Its advantage lies in its ability to detect and identify malignant tissue in the breast and generate a two-dimensional image through a single non-invasive *in-vivo* tomographic scan without the need for breast compression or biopsy. Through the use of portable neutron sources and portable gamma detectors, NSECT can potentially be translated to clinical use as a screening and diagnostic technique for breast cancer. Our final goal is to implement a portable, low-dose breast cancer screening system which can detect breast cancer without the need for breast compression or invasive biopsies.

ACKNOWLEDGMENT

REFERENCES

[1] A. Garg and V. Singh *et al.*, "An elemental correlation study in cancerous and normal breast tissue with successive clinical stages by neutron activation analysis," *Biol. Trace Element Res.*, vol. 46, pp. 185–202, 1994.

[2] Y. Katoh, T. Sato, and Y. Yamamoto, "Use of instrumental neutron activation analysis to determine concentrations of multiple trace elements in human organs," *Arch. Environ. Health*, Oct. 2003.

[3] G. S. Knight, A. H. Beddoe, S. J. Streat, and G. L. Hill, "Body composition of two human cadavers by neutron activation and chemical analysis," *Am. J Physiol. Endocrinol. Metab.*, vol. 250, pp. E179–E185, 1986.

[4] M. Yukawa, M. Suzuki-Yasumoto, K. Amano, and M. Terai, "Distribution of trace elements in the human body determined by neutron activation analysis," *Arch. Environ. Health*, vol. 35, pp. 36–44, 1980.

[5] A. Danielsen and E. Steinnes, "A study of some selected trace elements in normal and cancerous tissue by neutron activation analysis," *J. Nucl. Med.*, vol. 11, pp. 260–264, 1970.

[6] K. H. Ng, D. A. Bradley, L. M. Looi, C. Seman Mahmood, and A. Khalik Wood, "Differentiation of elemental composition of normal and malignant breast tissue by instrumental neutron activation analysis," *Appl. Radiat. Isot.*, vol. 44, pp. 511–516, 1993.

[7] G. V. Iyengar, K. Kasperek, and L. E. Feinendegen, "Determination of certain bulk and trace elements in the bovine liver matrix using neutron activation analysis," *Phys. Med. Biol.*, vol. 23, pp. 66–76, 1978.

[8] W. E. Kollmer, P. Schramel, and K. Samsal, "Simultaneous determination of nine elements in some tissues of the rat using neutron activation analysis," *Phys. Med. Biol.*, vol. 17, pp. 555–562, 1972.

[9] C. E. Floyd, J. E. Bender, A. C. Sharma, A. J. Kapadia, J. Q. Xia, B. P. Harrawood, G. D. Tourassi, J. Y. Lo, A. S. Crowell, and C. R. Howell, "Introduction to neutron stimulated emission computed tomography," *Phys. Med. Biol.*, vol. 51, pp. 3375–3390, 2006.

[10] C. E. Floyd, A. J. Kapadia, J. E. Bender, A. C. Sharma, J. Q. Xia, B. P. Harrawood, G. D. Tourassi, J. Y. Lo, A. S. Crowell, and C. R. Howell, "Neutron stimulated emission computed tomography of a multi-element phantom," *Phys. Med. Biol.*, submitted for publication.

[11] C. E. Floyd, C. R. Howell, B. P. Harrawood, A. S. Crowell, A. J. Kapadia, R. Macri, J. Q. Xia, R. Pedroni, J. Bowsher, M. R. Kiser, G. D. Tourassi, W. Tornow, and R. Walter, "Neutron stimulated emission computed tomography of stable isotopes," in *Proc. SPIE Medical Imaging 2004*, vol. 5368, pp. 248–254.

[12] A. J. Kapadia, C. E. Floyd, J. E. Bender, C. R. Howell, A. S. Crowell, and M. R. Kiser, "Non-invasive quantification of iron 56-Fe in beef liver using neutron stimulated emission computed tomography," in *Proc. IEEE Nuclear Science Symp., Medical Imaging Conf. 2005*, vol. 4, pp. 2232–2234.

[13] A. J. Kapadia, A. C. Sharma, G. D. Tourassi, J. E. Bender, A. S. Crowell, M. R. Kiser, C. R. Howell, and C. E. Floyd, "Neutron spectroscopy of mouse using Neutron Stimulated Emission Computed Tomography (NSECT)," in *Proc. IEEE Nuclear Science Symp., Medical Imaging Conf. 2006*, vol. 6, pp. 3546–3548.

[14] A. J. Kapadia, A. C. Sharma, G. D. Tourassi, J. E. Bender, A. S. Crowell, M. R. Kiser, C. R. Howell, and C. E. Floyd, "Neutron Stimulated Emission Computed Tomography (NSECT) for early detection of breast cancer," in *Proc. IEEE Nuclear Science Symp., Medical Imaging Conf. 2006*, vol. 6, pp. 3928–3931.

[15] A. J. Kapadia, A. C. Sharma, G. D. Tourassi, J. E. Bender, A. S. Crowell, M. R. Kiser, C. R. Howell, and C. E. Floyd, "Non-invasive estimation of potassium (39K) in bovine liver using Neutron Stimulated Emission Computed Tomography (NSECT)," in *Proc. IEEE Nuclear Science Symp., Medical Imaging Conf. 2006*, vol. 4, pp. 2076–2078.

[16] J. E. Bender, C. E. Floyd, B. P. Harrawood, A. J. Kapadia, A. C. Sharma, and J. L. Jesneck, "The effect of detector resolution for quantitative analysis of neutron stimulated emission computed tomography," in *Proc. SPIE Medical Imaging 2006*, vol. 6142, pp. 1597–1605.

[17] A. C. Sharma, G. D. Tourassi, A. J. Kapadia, J. E. Bender, J. Q. Xia, B. P. Harrawood, A. S. Crowell, M. R. Kiser, C. R. Howell, and C. E. Floyd, "Development of a high-energy gamma camera for use with NSECT imaging of the breast," in *Proc. IEEE Nuclear Science Symp., Medical Imaging Conf. 2006*, vol. 6, pp. 3925–3927.

[18] K. H. Ng, D. A. Bradley, and L. M. Looi, "Elevated trace element concentrations in malignant breast tissues," *Brit. J. Radiol.*, vol. 70, pp. 375–382, 1997.

[19] S. Rizk and H. Sky-Peck, "Comparison between concentrations of trace elements in normal and neoplastic human breast tissue," *Cancer Res.*, vol. 44, pp. 5390–5394, 1984.

[20] A. Schwartz and R. Fink, "Trace elements in normal and malignant human breast tissue," *Surgery*, vol. 76, pp. 325–329, 1974.

[21] R. Engelhardt, J. H. Langkowski, R. Fischer, P. Nielsen, H. Kooijman, H. C. Heinrich, and E. Bucheler, "Liver iron quantification: Studies in aqueous iron solutions, iron overloaded rats, and patients with hereditary hemochromatosis," *Magn. Reson. Imaging*, vol. 12, pp. 999–1007, 1994.

[22] J. P. Villeneuve, M. Bilodeau, R. Lepage, J. Cote, and M. Lefebvre, "Variability in hepatic iron concentration measurement from needle-biopsy specimens," *J. Hepatol.*, vol. 25, pp. 172–177, 1996.

[23] J. M. Alustiza, J. Artetxe, A. Castiella, C. Agirre, J. I. Emparanza, P. Otazua, M. Garcia-Bengoechea, J. Barrio, F. Mujica, and J. A. Recondo, "MR quantification of hepatic iron concentration," *Radiology*, vol. 230, pp. 479–484, 2004.

[24] L. W. Powell, "Diagnosis of hemochromatosis," *Semin. Gastrointest. Dis.*, vol. 13, pp. 80–88, 2002.

[25] S. R. Hollan, "Transfusion-associated iron overload," *Curr. Opin. Hematol.*, vol. 4, pp. 436–441, 1997.

[26] S. Joffe, "*Hemochromatosis*" [Online]. Available: http://www.emedicine.com/radio/topic323.htm 2005

[27] L. Powell, "Hemochromatosis," in *Harrison's Principles of Internal Medicine*, D. Kasper, A. S. Fawci, D. L. Longo, E. Braunwald, S. L. Hauser, and J. L. Jameson, Eds., 16th ed. New York: McGraw Hill, 2005, vol. 2, pp. 2298–2303.

[28] G. Brewer, "Wilson disease," in *Harrison's Principals of Internal Medicine*, D. Kasper, A. S. Fawci, D. L. Longo, E. Braunwald, S. L. Hauser, and J. L. Jameson, Eds., 16th ed. New York: McGraw Hill, 2005, vol. 2, pp. 2313–2315.

[29] A. P. Dempster, N. M. Laird, and D. B. Rubin, "Maximum likelihood from incomplete data via the EM algorithm," *J. Royal Stat. Soc. Series B*, vol. 39, pp. 1–38, 1977.

[30] R. Sundberg, "Maximum likelihood theory for incomplete data from an exponential family," *Scand. J. Stat.*, vol. 1, pp. 49–58, 1974.

[31] L. Shepp and Y. Vardi, "Maximum likelihood reconstruction for emission tomography," *IEEE Trans. Med. Imag.*, vol. MI-1, pp. 113–122, Oct. 1982.

[32] H. Mussalo-Rauhamaa, S. Piepponen, J. Lehto, R. Kauppila, and O. Auvinen, "Cu, Zn, Se and Mg concentrations in breast fat of Finnish breast cancer patients and healthy controls," *Trace Elements in Med.*, vol. 10, pp. 13–15, 1993.

[33] C. R. Howell and Q. Chen *et al.*, "Toward a resolution of the neutron-neutron scattering length issue," *Phys. Lett. B*, vol. 444, pp. 252–259, 1998.

[34] P. Håkansson, "An introduction to the time-of-flight technique," *Braz. J. Phys.*, vol. 29, pp. 422–427, 1999.

[35] C. E. Floyd, A. C. Sharma, J. E. Bender, A. J. Kapadia, J. Q. Xia, B. P. Harrawood, G. D. Tourassi, J. Y. Lo, M. R. Kiser, A. S. Crowell, R. S. Pedroni, R. A. Macri, S. Tajima, and C. R. Howell, "Neutron stimulated emission computed tomography: Background corrections," *Nucl. Instrum. Methods Phys. Res. Section B*, vol. 254, pp. 329–336, 2007.

[36] J. E. Bender, A. J. Kapadia, A. C. Sharma, G. D. Tourassi, B. P. Harrawood, and C. E. Floyd, "Breast cancer detection using neutron stimulated emission computed tomography: Prominent elements and dose requirements," *Med. Phys.*, vol. 34, pp. 3866–3871, 2007.

[37] National Nuclear Data Center BNL, NuDat 2.3 2007.

[38] A. J. Kapadia and C. E. Floyd, "An attenuation correction technique to correct for neutron and gamma attenuation in the reconstructed image of a neutron stimulated emission computed tomography (NSECT) system," in *Proc. SPIE Medical Imaging 2005*, vol. 5745, pp. 737–743.

[39] A. C. Sharma, B. P. Harrawood, A. J. Kapadia, J. E. Bender, and G. D. Tourassi, "Neutron stimulated emission computed tomography: A Monte Carlo simulation approach," *Phys. Med. Biol.*, vol. 52, pp. 6117–6131, 2007.

Neutron-stimulated emission computed tomography of a multi-element phantom

Carey E Floyd Jr[1,2]**, Anuj J Kapadia**[1,2]**, Janelle E Bender**[2]**,
Amy C Sharma**[1,2]**, Jessie Q Xia**[1,2]**, Brian P Harrawood**[1]**,
Georgia D Tourassi**[1]**, Joseph Y Lo**[1,2]**, Alexander S Crowell**[3,4]**,
Mathew R Kiser**[3,4] **and Calvin R Howell**[3,4]

[1] Department of Radiology, Duke Advanced Imaging Laboratories, Durham, NC 27705, USA
[2] Department of Biomedical Engineering, Duke University, Durham, NC 27708, USA
[3] Department of Physics, Duke University, Durham, NC 27706, USA
[4] Triangle Universities Nuclear Laboratory, Duke University, Durham, NC 27706, USA

E-mail: anuj.kapadia@duke.edu

Abstract

This paper describes the implementation of neutron-stimulated emission computed tomography (NSECT) for non-invasive imaging and reconstruction of a multi-element phantom. The experimental apparatus and process for acquisition of multi-spectral projection data are described along with the reconstruction algorithm and images of the two elements in the phantom. Independent tomographic reconstruction of each element of the multi-element phantom was performed successfully. This reconstruction result is the first of its kind and provides encouraging proof of concept for proposed subsequent spectroscopic tomography of biological samples using NSECT.

1. Introduction

Neutron-stimulated emission computed tomography (NSECT) is a technique for non-invasive *in vivo* imaging of stable isotopes in the body (Floyd *et al* 2004, 2006). It uses a thin beam of fast neutrons to stimulate stable nuclei in a sample, which emit characteristic gamma radiation. The energy of the emitted gamma is unique to the nucleus and is used to identify the emitting nucleus. NSECT is a technique of tomographic spectroscopy. In the current implementation, the tomographic path of integration is defined by the neutron beam while the emitting nuclear species is identified by gamma spectroscopy. The result is a tomographic and spectroscopic image of element distribution in the body acquired through a non-invasive *in vivo* scan. While other techniques have been developed for identifying the concentrations of elements in tissue samples (Geraki and Farquharson 2002, Ng *et al* 1993, 1997), NSECT is the first technique with properties that will allow non-invasive and *in vivo* spectroscopic imaging

in humans or small animals with a non-lethal radiation dose. Previously, we have presented an introduction to NSECT along with some preliminary results to demonstrate proof of concept for some of the required key components of the system (Floyd *et al* 2004, 2006, Kapadia *et al* 2005, 2006a, 2006b, 2006c, 2007, 2008). Here, we present a full description of the tomographic technique as successfully applied to acquire and reconstruct tomographic images from a multi-element phantom.

The motivation for this work is to develop a technique that can image the elemental composition of biomedical volumes *in vivo*. Potential applications include cancer diagnosis and staging by examining the concentration of certain elements in regions of suspicion based on an observed difference in the trace element concentration between benign and malignant tissues (Dobrowolski *et al* 2002, Ng *et al* 1993, 1997, Schwartz and Fink 1974, Gregoriadis *et al* 1983, Rizk and Sky-Peck 1984); quantitative assessment of the iron load in the liver (Brittenham and Badman 2003), following the transport of nutrients through the body; and the role of metals in dementia (Stedman and Spyrou 1995).

The physical principles behind NSECT are based on neutron inelastic scattering and nuclear spectroscopy, and include the physics of computed tomography. Each of these principles that are important for NSECT is described below.

1.1. Neutron inelastic scatter

When a neutron collides with an atomic nucleus at incident neutron energies of interest (1–7.5 MeV), one of several processes may occur. The most probable interaction is elastic scattering, while inelastic scattering is the next most likely interaction (Evans 1955). Other interactions, such as neutron capture (n,γ), charge exchange (n,p), knockout (n,d), (n,t), $(n, {}^3\text{He})$, $(n, {}^4\text{He})$, or fission (n,x), are less likely. When the neutron scatters inelastically, some of the energy of the neutron is transferred to the nucleus leaving it in an excited state. After a short time (typically several picoseconds), the excited nucleus decays to a lower energy state, usually by emitting a gamma photon. The photon has energy equal to the difference in energy between the two states, and an angular distribution specified by the difference in angular momentum and parity of these states (Cottingham and Greenwood 1986). The energy of the emitted gamma ray is used to identify the emitting nucleus.

1.2. Gamma spectroscopy

The gamma emissions that are stimulated by inelastic neutron scattering are characteristic of the isotope and energy states involved. While the energy of emitted gamma rays is not absolutely unique to each element, there is very little overlap over the range of elements and neutron energies of interest to NSECT. A high-resolution gamma detector acquires the energy spectrum emitted by the elements along the path of the neutron beam. NSECT uses the characteristic signature of these inelastic collisions to identify the isotope from which the neutron scatters. The incident neutron flux is shaped into a beam that defines a path of integration. The emitted gamma flux that is characteristic of a particular element is proportional to the concentration of that element in the body integrated over the path of the neutron beam weighted by the incident flux of the neutron beam. In this way, multiple energy integrals are acquired simultaneously for each spatial path integral defined by the orientation of the neutron beam. The spatial projections of each combination of energy channels associated with a given element can be reconstructed separately to provide tomographic image reconstructions that represent the spatial distribution of each respective element within the illuminated volume of the sample.
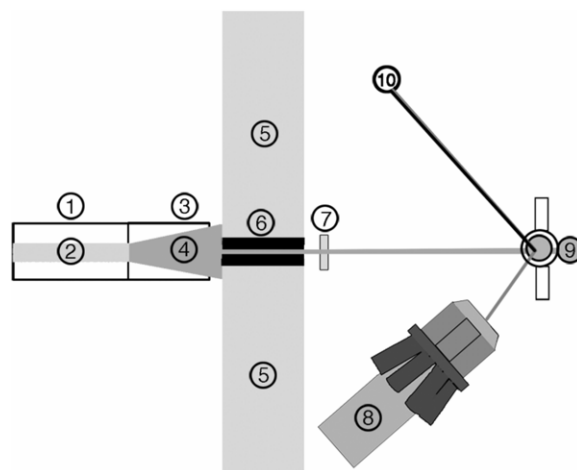
Figure 1. Geometry for NSECT tomography experiment. (1) Neutron accelerator tube, (2) deuteron beam, (3) deuterium gas cell, (4) neutron production region, (5) shield wall, (6) copper collimator, (7) thin plastic neutron monitor, (8) HPGe gamma detector with Compton shield, (9) sample target on translational and rotational stages, (10) inelastically scattered neutron.

1.3. Computed tomography

The projection-slice theorem states that if line integrals (referred to as projections) of a property of a body are acquired such that these line integrals cover the area at all angles of a slice through the body, then the interior density of the slice can be reconstructed from these projections. The process of reconstruction is called tomography and the image of the interior spatial density is known as the tomographic image. The simplest technique for reconstructing the interior from a complete set of projections is Fourier inversion (FI) (Kak and Slaney 1999). Unfortunately, practical limitations of sampling seriously limit the number of applications for which FI yields acceptable image quality. The most popular reconstruction algorithm over the past 30 years has been filtered back projection in which each projection ray is filtered by a $1/r^2$ function, and the resulting value is distributed uniformly along the projection path through the interior space to be reconstructed (Kak and Slaney 1999). With a sufficient signal-to-noise ratio (SNR) and sufficient spatial and angular sampling in the acquisition of the projections, this technique can provide high-quality images. Unfortunately, in many applications (including NSECT), the SNR and the number of spatial and angular samples are related to the acquisition time and to the patient dose, both quantities that should ideally be minimized. For this reason, statistical-based algorithms are used. For the work presented here, we have chosen the maximum likelihood through expectation maximization (MLEM) algorithm as developed for emission computed tomography (ECT) (Lange and Carson 1984). The advantage of this algorithm for applications like NSECT is that it is more tolerant of a limited SNR and sampling than FBP or FI (Lange and Carson 1984). A feature of MLEM that is of advantage to NSECT is the ability to incorporate several physical features of the acquisition system and geometry directly into the reconstruction algorithm through a forward-modeling approach. For example, MLEM is able to model the Poisson nature of gamma counting, number and location of gamma detectors, and non-uniform acquisition geometries. MLEM still requires projection data that reflect the line integral of the elemental concentrations within the sample. These line integrals are provided by a neutron beam that defines the path and geometry of integration. The neutron
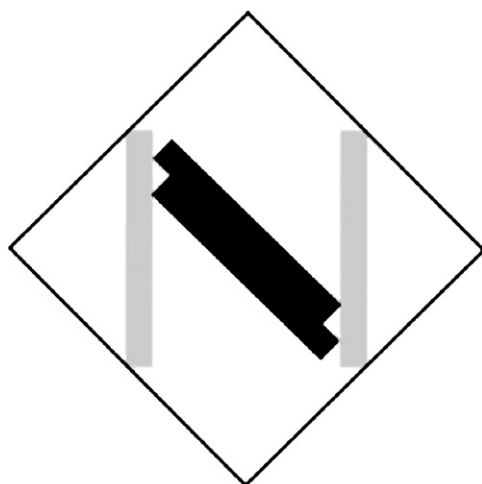
Figure 2. Geometry of the phantom imaged in the tomography experiment. The gray bars represent copper, while the black bars represent iron. Each bar measures 0.6 cm in width, 6 cm in height and 2.5 cm in depth (into the page).

beam stimulates the emission of characteristic gamma photons that are integrated in a gamma spectrometer.

2. Materials and methods

NSECT experiments are currently performed at the Triangle Universities Nuclear Laboratory (TUNL) at Duke University, Durham, NC. TUNL is a medium energy accelerator source with a tandem Van-de-Graaff accelerator capable of producing neutron beams up to 20 MeV.

2.1. Neutron illumination

Neutrons for our experiments were produced at the shielded neutron source facility of TUNL. A 7.5 MeV neutron beam was produced through the d(d,n) reaction using the geometry shown in figure 1.

The 7.5 MeV neutron beam passed through a 1.5 m long copper collimator with swappable inserts that allowed manipulation of the size and shape of the beam profile. The profile of the neutron beam was measured using a 1 mm thick plastic scintillator that was moved across the beam at the location of the sample. The counts were recorded for each position in both the horizontal and the vertical planes to map the beam profile in two dimensions.

2.2. Sample phantom

A phantom was constructed of solid bars of natural copper and natural iron to form the shape of the letter 'N'. A schematic drawing of the top view of this phantom is shown in figure 2. The gray bars represent copper, while the black bars represent iron. Each bar measured 0.6 cm in width, 6 cm in height and 2.5 cm in depth (into the page).

2.3. Sample transport

The sample was held on a computer-controlled stage that permitted motion in the horizontal plane (across the beam path), the vertical plane and rotation about the vertical (tomographic) axis. With the beam fixed, the horizontal motion allowed selecting a projection path through
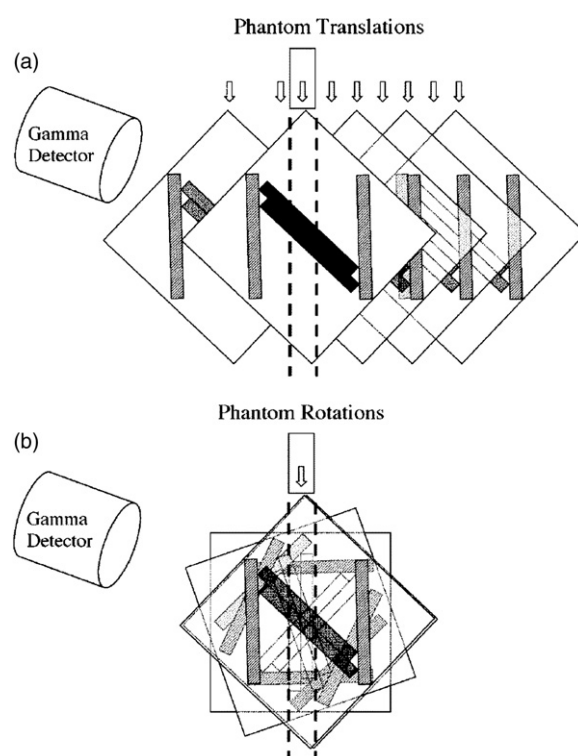
Figure 3. Top view of phantom showing (a) translations and (b) rotations used to achieve the tomographic acquisition geometry. The gray bars are copper and black bars are iron. All bars have height 6 cm, width 0.6 cm and depth 2.5 cm. The maximum dimension of the phantom is 9 cm (diagonal).

the sample, the vertical motion allowed selecting a trans-axial slice through the sample, and the rotation about the central axis of the sample allowed selecting a projection angle for the stimulating neutron beam. This arrangement is shown in figure 3.

2.4. Gamma spectroscopy

The characteristic gamma photons emitted due to inelastic scattering of neutrons have energies between 100 and 6500 keV (National Nuclear Data Center 2007). Photons in this energy range are well transmitted through the body with transmission between 12% at low energies (300 keV), where the attenuation coefficient is 0.21 cm^{-1}, and 65% at higher energies (6500 keV), where the attenuation coefficient is 0.043 cm^{-1} (NIST 1990). The emitted gamma photons were detected in a high purity germanium (HPGe) detector with an energy resolution of 0.1% full-width at half-maximum (FWHM) at 1 MeV detected energy, corresponding to $\pm$1 keV (Knoll 2000). This resolution was sufficient to resolve most of the gamma photon energies that were characteristic of the isotopes of interest with incident neutron energy between 1 MeV and 7.5 MeV.

The HPGe detector was surrounded by an anti-Compton shield in the axial dimension of the germanium element. This shield was a cylindrical section of NaI and a conical section of BGO coupled to photomultiplier tubes with preamplifiers whose outputs were summed. If a photon produced a signal in the main detector by Compton scattering, there was a high

probability that the scattered photon would interact with the shield. These events would have a signature given by a coincidence between a signal in the main detector and a signal in the shield. The coincidence events were used to block the input to the spectroscopy amplifier that processed the main detector signal and thus reduced the processing of signals that were due to Compton-scattered events that escaped the main detector. The output of the spectroscopy amplifier was read into an analog-to-digital converter and was then read into the data acquisition computer.

2.5. Tomography

The projection-slice theorem states that the interior density in plane passing through an object can be reconstructed from a complete set of projections that consist of line integrals of the density along all paths that lie within that plane. In transmission computed tomography (TCT), these line integrals consist of the total attenuation of a beam with known intensity passing from a point photon source through the object and ending in a photon detector. In ECT, the source of photons is distributed through the object, and the paths of the line integrals are defined by the acceptance beam of a lead collimator placed on the detector. For NSECT, the path is defined by the beam of the stimulating neutrons. Photons whose emission is stimulated by this beam are integrated in the gamma detector. In this experiment, the phantom was scanned at 8 angular positions at $22.5°$ intervals and 11 spatial positions at 8 mm intervals at each angle.

2.6. Reconstruction

Images were reconstructed from the projection data sets using the MLEM algorithm as derived for positron emission tomography (PET) (Lange and Carson 1984). For our implementation of this technique, the probabilities were computed using Monte Carlo techniques as developed for single photon emission computed tomography (SPECT) (Floyd *et al* 1985). While these algorithms were developed for ECT, they are appropriate for extension to NSECT due to the shared principles of stimulated emission computed tomography. The algorithm is defined below following the notation in Lange and Carson (1984).

Let λ_j represent the image intensity in the image voxel j where $j = 1, \ldots, N_J$ with N_J being the number of image voxels. Let Y_i represent the projection ray i where $i = 1, \ldots, N_I$ with N_I being the number of projection measurements. Let p_{ji} equal the probability that a photon emitted from the source voxel j is detected when the stimulating neutron beam is at orientation i. p_{ji} are pre-computed using a Monte Carlo calculation that accurately models the beam shape, the voxel shape, the angular spacing, and the detector size and location. For this experiment, the reconstruction voxels are square regions, 1 mm on a side. The MLEM algorithm for the $k + 1$th iteration is then given by

$$\lambda_j^{k+1} = \frac{\lambda_j^k}{\sum_{i''}^{N_I} p_{ji''}} \sum_{i'}^{N_I} \frac{p_{ji'} Y_{i'}}{\sum_{j'}^{N_J} p_{j'i'} \lambda_{j'}^k}. \tag{1}$$

The first factor on the right side of the equal sign is the estimate of the source voxel j at the kth iteration and the rest is the correction to it. The second factor is a normalization factor. The sum over i' is of the ratio of the measured projection data at projection i' ($Y_{i'}$) to the estimated projection based on the kth estimate of λ, weighted by the probability that this projection originates from the voxel j ($p_{ji'}$).

This algorithm converges absolutely to the maximum likelihood (ML) solution (Lange and Carson 1984). For image reconstruction, the ML solution often is not what we want to visualize as it can be very noisy looking. To overcome this, the MLEM algorithm should be
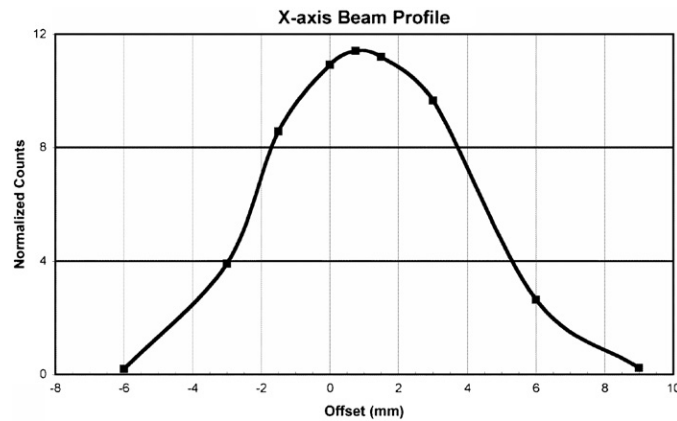
Figure 4. Neutron beam profile along the horizontal axis measured with a 1 mm thick plastic scintillator. The beam measured 0.70 cm at full-width at half-maximum.
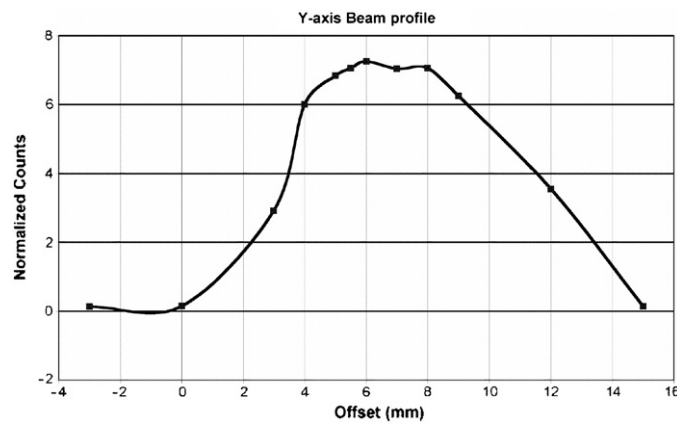
Figure 5. Neutron beam profile along the vertical axis measured with a 1 mm thick plastic scintillator. The beam measured 0.86 cm at full-width at half-maximum.

'regularized'. One of the easiest techniques for regularization is to terminate the iterations before the algorithm has completely converged. For our initial implementation, we performed this step visually by picking the iteration at which the structure of the phantom appeared to be well represented but where the noise was not objectionable. A uniform distribution was chosen for the initial guess of the source voxels λ°. We examined reconstructed images at each iteration between 1 and 50 and chose 6 as the optimum. Reconstruction required about 1 s per iteration on a 1 GHz PC running Linux.

3. Results

3.1. Beam profiles

The profiles along the horizontal and vertical axes are shown in figures 4 and 5, respectively. The beam profiles at FWHM measured as 0.70 cm in the horizontal dimension and 0.86 cm in the vertical dimension.
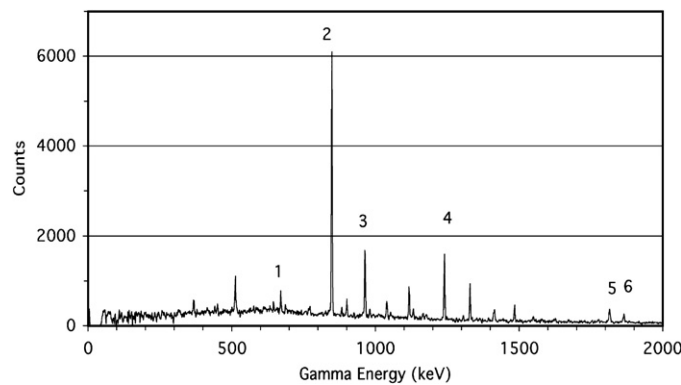
Figure 6. Gamma energy spectrum corrected for accidental background. Spectral lines corresponding to six states from ^{56}Fe and ^{63}Cu are indicated by numbers: (1) ^{63}Cu from the first excited state to the ground state; energy 660 keV. (2) ^{56}Fe from the first excited state to the ground state; energy 847 keV. (3) ^{63}Cu from the second excited state to the ground state; energy 962 keV. (4) ^{56}Fe from the third to the second excited state; energy 1239 keV. (5) ^{56}Fe from the fourth to the second excited state; energy 1811 keV. (6) ^{63}Cu from the sixth to the first excited state; energy 1864 keV.

3.2. Spectra

Figure 6 shows the background-corrected spectrum from one spatial position at one projection angle. Six spectral lines were identified corresponding to energy transitions from iron and copper and are labeled 1–6 in the figure caption.

3.3. Sinograms

The emissions from the first two states in each of ^{56}Fe and ^{63}Cu were summed to generate a projection profile for each element. The sums are shown plotted as sinograms for each element for angles 0° and 45° in figure 7.

From these projections, it can be seen that there is a change in the profile with a change of angle. At 0°, the iron bars are almost parallel to the beam and the iron projection shows its narrowest profile. The copper is spread fairly evenly except for some overlap near the center. As the angle increases from 0°, the copper bars become more parallel with the beam, reaching a maximum at 45° as can be seen by the narrowing of the copper peaks. The normalized yields in the sinograms represent the input projection values to the MLEM reconstruction algorithm.

3.4. Reconstructed images

The reconstructed image for copper is shown in figure 8 and the image from iron is shown in figure 9. Each figure was reconstructed separately from projections for the individual element and attenuation corrected using the algorithm described in Kapadia *et al* (2005).

The combination of the two reconstructed images is shown in figure 10. Note that the combined figure was generated by adding the separately reconstructed images, and not by adding the projection data before reconstruction. Figure 11 shows the combined reconstructed image overlaid with the schematic of the phantom for comparison.

A horizontal profile of gamma intensity through the reconstructed image is shown in figure 12. From figures 11 and 12, it is evident that the reconstructed image shows a broader profile of the object than the object itself. This was entirely expected since the spatial sampling
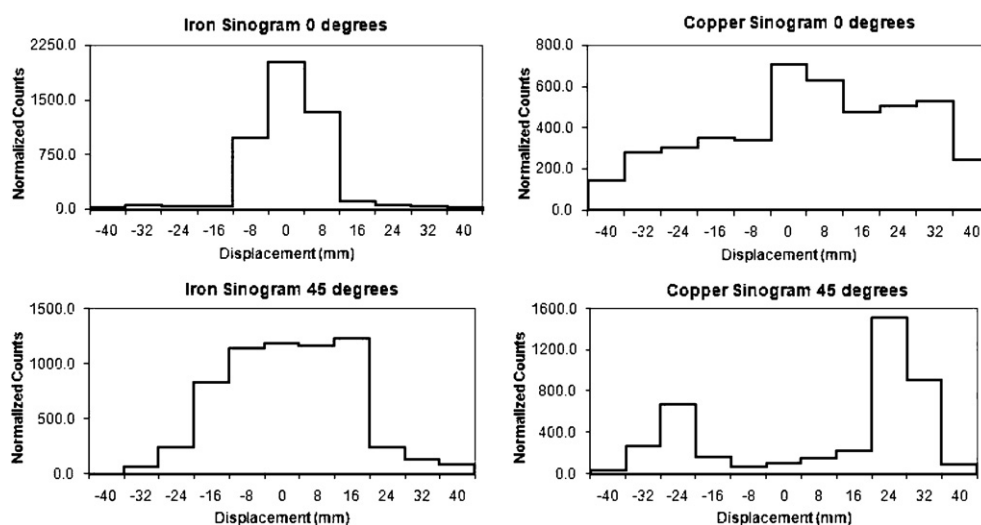
Figure 7. Projection profiles for iron (on the left) and copper (on the right) for projection angles 0° and 45°.

was performed in 8 mm intervals while the width of the individual bars was 6 mm. What is of note is that the result of reconstructing this under-sampled system was a smooth overestimation of size rather than an image with a significant artifact. The width of the line profiles for the two copper bars at FWHM was found to measure 1.05 cm.

4. Discussion

This paper presents the first tomographic image reconstruction from a multi-element phantom using NSECT. The reconstructed images demonstrate reasonable fidelity in imaging the spatial distribution of elements within an object through a non-invasive scan, especially given the sparse sampling of the data acquisition. Images were reconstructed on an 88 × 88 pixel matrix from an acquisition that sampled the object at only 88 projections. This reconstruction was possible due to the superior performance of the MLEM algorithm in severely under-sampled systems with non-uniform data sampling.

It can be noted that the original object space was acquired with 11 pixels on a side (11 spatial projections), but was reconstructed with 88 pixels on a side. This does not represent a true eight-fold increase in the resolution of the system. The apparent increase in resolution comes from the Monte Carlo code used to generate the probability matrix (p_{ji}) for the MLEM algorithm, where the image space is divided into a grid of 88 × 88 pixels. Probabilities are calculated for each pixel in this grid and are used to obtain pixel intensities based on the experimental projection data. As a result, the intensities in the reconstructed image are distributed into a higher resolution region than the original acquisition. The beam and acquisition parameters used in calculating MLEM probabilities were kept consistent with the experiment, i.e. 11 spatial projections at each of 8 angles. The true resolution of the system achieved in this experiment was found to be approximately 1 cm, which depends largely on the width of the neutron beam. The beam in this experiment measured 0.7 cm at FWHM in the horizontal direction, with tails extending up to 1.5 cm. The resolution obtained here is a reasonable value, given the limitations of this experimental system. It should be noted that
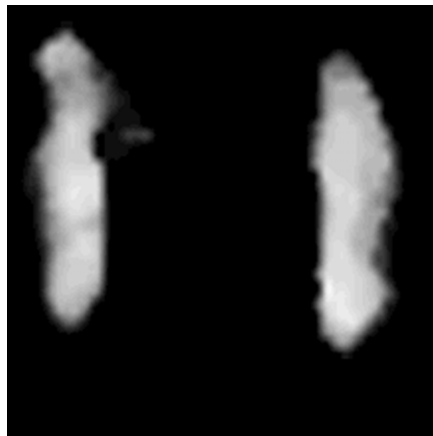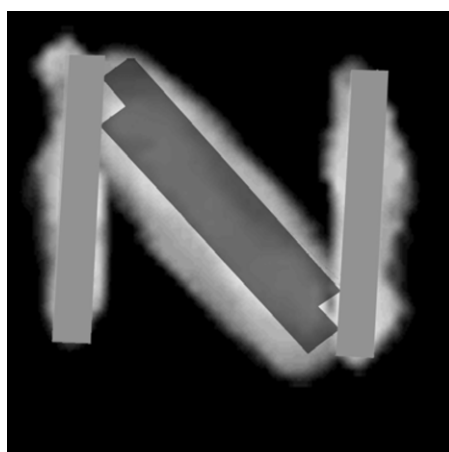
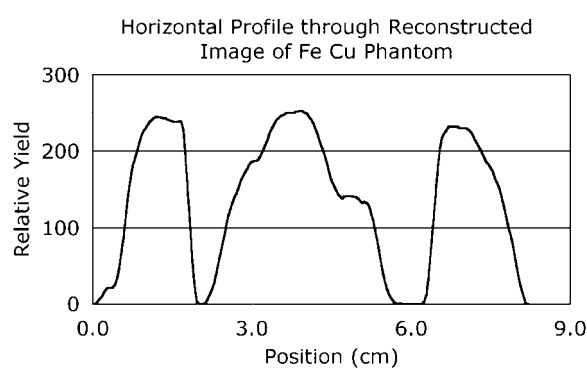**Figure 8.** Reconstructed copper image.
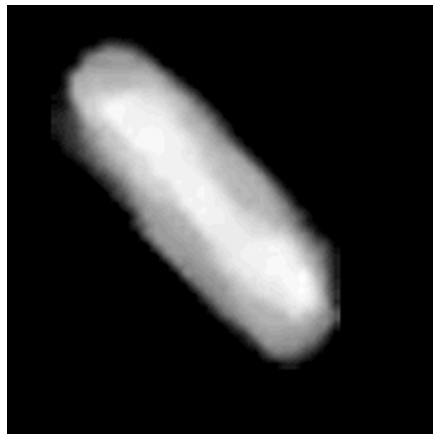
Figure 9. Reconstructed iron image.

Figure 10. Sum of the iron and copper images.

Figure 11. Sum of reconstructed iron and copper images overlaid with the schematic drawing of the phantom.

Figure 12. Profile through summed reconstructed image.

the sample used in this experiment describes an ideal experimental scenario with very a low scatter background due to the absence of hydrogen. In a biological sample, however, there will be considerable neutron scatter generated by hydrogen in tissue, which will affect the true resolution of the system. Neutrons that are meant to illuminate a certain voxel in the sample may scatter onto adjacent voxels containing an element of interest and induce inelastic gamma emission from that voxel. Detection of the adjacent-voxel gammas may lead to a spread in the tails of the resulting sinograms, which can lead to reduced resolution. While the resolution of the NSECT system depends primarily on the size of the incident neutron beam, the best resolution achievable in a hydrogen-rich biological sample will also be limited by the scatter noise component.

Images were corrected for attenuation using a technique developed specifically for NSECT applications (Kapadia *et al* 2005). This technique calculates the attenuation correction factors due to combined neutron and gamma attenuation effects and applies the correction to the individual projection data before it is reconstructed.

While no clinical applications have been described in this paper, the eventual goal is to develop NSECT into a clinical imaging modality. Therefore, it is necessary to address certain issues that will affect the clinical feasibility of the system. First, the neutron source used in this experiment is a Van-de-Graaff accelerator which is an immovable and expensive source that is difficult to use in a clinical system. A portable neutron source is more suited for this purpose. For dedicated applications, neutrons with energy of a few MeV are readily and economically produced using commercially available neutron generators. Neutrons of these energies can easily penetrate the body to allow good coverage of internal organs for a wide range of elements commonly observed in the human body. Second, using neutrons also leads to significant concerns about patient dose. We have performed several dose-analysis experiments using simulations in GEANT4, which have demonstrated that NSECT can detect biologically relevant concentrations of elements with doses lower than 10 mSv (Bender *et al* 2007, Kapadia 2007, Sharma *et al* 2007). Finally, NSECT must be able to achieve the sensitivity required to image clinically relevant concentrations of elements in finite localized lesions. Simulation studies performed to investigate NSECT sensitivity and resolution have demonstrated the ability to detect an iron concentration of 5 mg g^{-1} in a 2 cm lesion in the liver using a 1 cm wide beam (Kapadia 2007, Kapadia *et al* 2007). Sensitivity analysis performed with the experimental system has shown the ability to detect as little as 0.3 g of sodium in a hydrogen-rich sample (Kapadia *et al* 2008). The detection of smaller lesions with lower element concentrations may be possible by optimizing the acquisition parameters to deliver maximum neutron flux to the illuminated volume of the lesion using a narrow beam while minimizing the volume of illuminated background tissue. Regardless, detection of smaller lesions with low element concentration will require improvement in the sensitivity of the current system.

The phantom used in this experiment consists of solid bars of iron and copper. While the concentration of elements and the physical size of this phantom do not represent a clinically realistic scenario, it provides an adequate starting point for proof-of-concept experimental acquisition. Future experiments will be performed with clinically relevant phantoms that model disease states in the human body.

5. Conclusion

This paper has described the first results from the tomographic reconstruction of a multi-element sample using NSECT. The results demonstrate proof of concept for imaging the spatial distribution of elements within a body through a non-invasive scan. The results and techniques described in this paper can be developed further to enable NSECT to evolve into a clinical diagnostic imaging modality. Work is currently underway to address the limitations of the system that will make it more suitable for clinical imaging, especially for diagnosis of breast and liver disorders.

References

Bender J E, Kapadia A J, Sharma A C, Tourassi G D, Harrawood B P and Floyd C E 2007 Breast cancer detection using neutron stimulated emission computed tomography: prominent elements and dose requirements *Med. Phys.* **34** 3866–71

Brittenham G and Badman D 2003 Noninvasive measurement of iron: report of an NIDDK workshop *Blood* **101** 15–9

Cottingham W N and Greenwood D A 1986 *An Introduction to Nuclear Physics* (New York: Cambridge University Press)

Dobrowolski Z, Drewniak T, Kwiatek W and Jakubik P 2002 Trace elements distribution in renal cell carcinoma depending on stage of disease *Eur. Urol.* **42** 475–80

Evans R 1955 *The Atomic Nucleus* (New York: Addison-Wesley)

Floyd C E Jr, Bender J E, Sharma A C, Kapadia A, Xia J, Harrawood B, Tourassi G D, Lo J Y, Crowell A and Howell C 2006 Introduction to neutron stimulated emission computed tomography *Phys. Med. Biol.* **51** 3375–90

Floyd C E, Jaszczak R J and Coleman R E 1985 Inverse Monte Carlo: a unified reconstruction algorithm for SPECT *IEEE Trans. Nucl. Sci.* **32** 779–85

Floyd C E *et al* 2004 Neutron stimulated emission computed tomography of stable isotopes *SPIE Medical Imaging (San Diego, CA)* pp 248–54

Geraki K and Farquharson M 2002 Concentrations of Fe, Cu and Zn in breast tissue: a synchrotron XRF study *Phys. Med. Biol.* **47** 2327–39

Gregoriadis G C, Apostolidis N S, Romanos A N and Paradellis T P 1983 A comparative study of trace elements in normal and cancerous colorectal tissues *Cancer* **52** 508–19

Kak A C and Slaney M 1999 *Principles of Computerized Tomographic Imaging* (New York: IEEE)

Kapadia A J 2007 Accuracy and patient dose in neutron stimulated emission computed tomography for diagnosis of liver iron overload: simulations in GEANT4 *Biomedical Engineering* (Durham, NC: Duke University)

Kapadia A J, Floyd C E, Bender J E, Howell C R, Crowell A S and Kiser M R 2005 Non-invasive quantification of iron 56-Fe in beef liver using neutron stimulated emission computed tomography *IEEE Nuclear Science Symp. Conf. 2005* **4** 2232–4

Kapadia A J, Tourassi G D, Sharma A C, Crowell A S, Kiser M R and Howell C R 2007 Experimental detection of iron overload in liver through neutron stimulated emission spectroscopy *Phys. Med. Biol.* submitted

Kapadia A J, Sharma A C, Tourassi G D, Bender J E, Crowell A S, Kiser M R, Howell C R and Floyd C E 2006a Neutron spectroscopy of mouse using neutron stimulated emission computed tomography (NSECT) *IEEE Nuclear Science Symp. Conf. Rec. 2006* **6** 3546–8

Kapadia A J, Sharma A C, Tourassi G D, Bender J E, Crowell A S, Kiser M R, Howell C R and Floyd C E 2006b Neutron stimulated emission computed tomography (NSECT) for early detection of breast cancer *IEEE Nuclear Science Symp. Conf. Rec. 2006* **6** 3928–31

Kapadia A J, Sharma A C, Tourassi G D, Bender J E, Crowell A S, Kiser M R, Howell C R and Floyd C E 2006c Non-invasive estimation of potassium (39 K) in Bovine liver using neutron stimulated emission computed tomography (NSECT) *IEEE Nuclear Science Symp. Conf. Rec. 2006* **4** 2076–8

Kapadia A J, Sharma A C, Bender J E, Tourassi G D, Howell C R, Crowell A S, Kiser M R, Harrawood B P and Floyd C E 2008 Neutron stimulated emission computed tomography for diagnosis of breast cancer *IEEE Trans. Nucl. Sci.* **55** 501–9

Knoll G F 2000 *Radiation Detection and Measurement* (Hoboken, NJ: Wiley)

Lange K and Carson R 1984 EM reconstruction algorithms for emission and transmission tomography *J. Comput. Assist. Tomogr.* **8** 306–16

National Nuclear Data Center B N L 2007 *National Nuclear Database NuDat 2.3*, url: http://www.nndc.bnl.gov/nudat2, Accessed 10 November 2005

Ng K H, Bradley D A and Looi L M 1997 Elevated trace element concentrations in malignant breast tissues *Br. J. Radiol.* **70** 375–82

Ng K H, Bradley D A, Looi L M, Seman Mahmood C and Khalik Wood A 1993 Differentiation of elemental composition of normal and malignant breast tissue by instrumental neutron activation analysis *Appl. Radiat. Isot.* **44** 511–6

NIST 1990 *XCOM: Photon Cross Sections Database*, url: http://physics.nist.gov/PhysRefData/Xcom/Text/XCOM.html, Accessed 10 November 2005

Rizk S and Sky-Peck H 1984 Comparison between concentrations of trace elements in normal and neoplastic human breast tissue *Cancer Res.* **44** 5390–4

Schwartz A and Fink R 1974 Trace elements in normal and malignant human breast tissue *Surgery* **76** 325–9

Sharma A C, Harrawood B P, Bender J E, Tourassi G D and Kapadia A J 2007 Neutron stimulated emission computed tomography: a Monte Carlo simulation approach *Phys. Med. Biol.* **52** 6117–31

Stedman J D and Spyrou N M 1995 Major and trace element concentration differences between right and left hemispheres of the 'normal' human brain *Nutrition* **11** 542–5

Experimental detection of iron overload in liver through neutron stimulated emission spectroscopy

A J Kapadia[1,2,5] **, G D Tourassi**[1]**, A C Sharma**[1,2]**, A S Crowell**[3,4]**, M R Kiser**[3,4] **and C R Howell**[3,4]

[1] Department of Radiology, Duke Advanced Imaging Laboratories, Durham, NC 27705, USA
[2] Department of Biomedical Engineering, Duke University, Durham, NC 27708, USA
[3] Department of Physics, Duke University, Durham, NC 27706, USA
[4] Triangle Universities Nuclear Laboratory, Duke University, Durham, NC 27706, USA

E-mail: anuj.kapadia@duke.edu

Abstract

Iron overload disorders have been the focus of several quantification studies involving non-invasive imaging modalities. Neutron spectroscopic techniques have demonstrated great potential in detecting iron concentrations within biological tissue. We are developing a neutron spectroscopic technique called neutron stimulated emission computed tomography (NSECT), which has the potential to diagnose iron overload in the liver at clinically acceptable patient dose levels through a non-invasive scan. The technique uses inelastic scatter interactions between atomic nuclei in the sample and incoming fast neutrons to non-invasively determine the concentration of elements in the sample. This paper discusses a non-tomographic application of NSECT investigating the feasibility of detecting elevated iron concentrations in the liver. A model of iron overload in the human body was created using bovine liver tissue housed inside a human torso phantom and was scanned with a 5 MeV pulsed beam using single-position spectroscopy. Spectra were reconstructed and analyzed with algorithms designed specifically for NSECT. Results from spectroscopic quantification indicate that NSECT can currently detect liver iron concentrations of 6 mg g^{-1} or higher and has the potential to detect lower concentrations by optimizing the acquisition geometry to scan a larger volume of tissue. The experiment described in this paper has two important outcomes: (i) it demonstrates that NSECT has the potential to detect clinically relevant concentrations of iron in the human body through a non-invasive scan and (ii) it provides a comparative standard to guide the design of iron overload phantoms for future NSECT liver iron quantification studies.

(Some figures in this article are in colour only in the electronic version)

[5] Address for correspondence: 2424 Erwin Road, Suite 302, Hock Plaza, Durham, NC 27705, USA.

1. Introduction

Iron overload disorders affect a significant part of the American population today. About 5 out of every 1000 Caucasians are susceptible to developing the disease (NIH 2007). These disorders may be due to genetic or acquired factors and cause an increase in the body's total iron content. In advanced stages of iron overload, the total body iron content is seen to increase by up to five times over normal, i.e. from 3 to 4 g to over 20 g total (Powell 2002, 2005, Powell *et al* 1998). The excess iron is stored in several vital organs in the body, especially in the liver, heart and spleen, and may cause extensive tissue damage, liver cirrhosis, cardiac failure, hepatic failure and hepatocellular carcinoma (Powell 2002, 2005, Powell *et al* 1998). Accurate measurement of the body's iron content is vital for effective diagnosis and management of the iron overload disorder. Since a significant part of the body's total iron is stored in the liver, an estimate of the liver's iron concentration is used as a measure of the body's total iron content. Currently, this measurement is obtained using an invasive liver biopsy, which is an unpleasant procedure associated with several potential complications. Repeated biopsy is required for monitoring the disease. The morbidity associated with performing repeated biopsy creates two obstacles: (1) in following the progress of patients obtaining therapeutic treatments and (2) in developing new forms of treatment for the disorder. Additionally, quantification results from biopsy suffer from as much as 20% margins of error in the presence of cirrhosis (Villeneuve *et al* 1996), primarily due to errors in tissue sampling (Bonkovsky *et al* 1999, Ratziu *et al* 2005, Regev *et al* 2002). There is an imminent need for an alternative technique to estimate liver iron concentration without a biopsy. A workshop conducted by the National Institute of Diabetes and Digestive and Kidney Diseases (NIDDK) to assess the needs for techniques to determine the iron concentration in the body concluded that 'physicians have a pressing clinical need for quantitative means of measuring body storage iron that are non-invasive, safe, accurate, and readily available to improve the diagnosis and management of patients with iron overload, including those with hereditary hemochromatosis, thalassemia major, sickle cell disease, aplastic anemia, myelodysplasia and other disorders' (Brittenham and Badman 2003).

Several different techniques have been attempted to detect and quantify the iron concentration in the liver *in vivo*, for example, x-ray computed tomography, MRI, MR spectroscopy, super-conducting quantum interference susceptometry (SQUID) and nuclear resonance scattering (NRS) (Alustiza *et al* 2004, Avrin and Kumar 2007, Bonkovsky *et al* 1999, Brittenham *et al* 2001, Cecchin *et al* 1990, Chapman *et al* 1980, Chezmar *et al* 1990, Dixon *et al* 1994, Gandon *et al* 2004, Guyader *et al* 1992, Howard *et al* 1983, Liu *et al* 1996, Nielsen *et al* 2000, 2002a, 2002b, Perrimond *et al* 1991, Sheth 2003, Vartsky *et al* 1979, 1982, Wielopolski *et al* 1985). While each has had varying degrees of success, few have found widespread acceptance in the clinical environment. Both x-ray CT and MRI lack the sensitivity required for detecting mild to moderate degrees of iron overload, and MRI also shows reduced sensitivity in cases of severe iron overload (Angelucci *et al* 1997, Chapman *et al* 1980, Chezmar *et al* 1990, Howard *et al* 1983). In MR spectroscopy (MRS), the low signal from bound Fe makes quantification studies difficult. MRS also has limited resolution (larger than 1 cm) (Wang *et al* 2002). While SQUID has found some success in detecting liver iron, there are only about four SQUID facilities in the world that offer iron overload testing, making it difficult to translate into a widely used clinical alternative. NRS has achieved some success in patients with iron overload but with high levels of dose (Wielopolski *et al* 1985).

Neutron spectroscopic techniques have demonstrated great potential in detecting element concentrations within biological tissue. Neutron activation analysis (NAA) and *in vivo* neutron activation analysis (IVNAA) have been used in several studies to map the elemental structure

of normal and diseased tissue in humans (McNeill *et al* 1990, Katoh *et al* 2003, Knight *et al* 1986, Ng *et al* 1993, Yukawa *et al* 1980, Zeisler *et al* 1993). Many of these studies have been successful in quantifying a large number of elements, and some have achieved sensitivity of a few micrograms (Arnold *et al* 2002). One NAA study has reported a detection limit of 58–60 mg Fe in a sample of mass 1.5 kg, corresponding to a concentration of 0.04 mg g^{-1} (McNeill *et al* 1990). Patient dose values associated with neutron activation methods have been reported to be less than 10 mSv (Mattsson and Thomas 2006). However, despite their apparent success, neutron activation techniques have not been widely accepted in the clinic.

We are developing a neutron spectroscopic technique called neutron stimulated emission computed tomography (NSECT), which has the potential to diagnose iron overload in the liver at clinically acceptable levels of dose through a non-invasive *in vivo* scan (Floyd *et al* 2006, 2008, Kapadia *et al* 2005, 2008). The technique uses fast <u>N</u>eutrons to <u>S</u>timulate elements in the body to <u>E</u>mit characteristic gamma radiation, which is acquired and reconstructed using <u>C</u>omputed <u>T</u>omography. NSECT utilizes inelastic scatter interactions between atomic nuclei in the sample and incoming fast neutrons to non-invasively determine the concentration of elements in the sample. The working principle is described briefly as follows. Incoming fast neutrons interact with atomic nuclei in the sample through inelastic scatter interactions, exciting the nuclei to higher energy levels. The excited nuclei rapidly decay to their ground states emitting gamma rays with energy equal to the difference between the excited and ground energy states. These energy states are quantized, well known and unique to most elements and isotopes. The emitted gamma rays are detected by an energy-sensitive gamma-ray detector. Measuring the energy and intensity of the emitted gamma rays provides an accurate estimate of the concentration of the emitting atoms in the target tissue.

Although the NSECT technique incorporates tomographic ability, this experiment discusses a simple non-tomographic application as a first step toward clinical translation of the technique. The non-tomographic approach, henceforth referred to as single-position spectroscopy (or simply spectroscopy), involves scanning the sample at only a single position without translation or rotation. This approach can be used for iron quantification in cases of uniform iron overload, where the distribution of iron in the entire region of the liver being scanned is uniform. In cases where the iron is distributed in non-uniform regions of varying iron content, a tomographic scan is required to determine the concentration and location of iron in each such region in the liver. While the iron storage mechanism of the liver is generally well understood, it has not yet been clearly demonstrated whether the excess iron is stored uniformly or in localized regions of varying concentration within the liver. NSECT has the ability to investigate both scenarios by generating quantitative tomographic images of iron distribution in the liver. Each of the two acquisition methods, single-position spectroscopy and multi-position tomography, has the potential for clinical applicability in a different scenario. For the purpose of this paper, the readers should note that although the term NSECT appears when referring to the imaging technique, acquisition has been performed using single-position spectroscopy. Therefore, no tomographic results are presented here. Tomography experiments and resulting images have been described in other publications (Kapadia 2007, Sharma *et al* 2007, Floyd *et al* 2008).

In this paper, we present results from a study investigating the feasibility of detecting elevated iron concentrations in the liver through NSECT. As this technique is still in its initial stages, feasibility testing is essential in working toward the final goal of implementing a low-dose scanning solution for detecting and monitoring iron concentrations in the liver. In earlier work, we have demonstrated the technique's ability to perform spectroscopic quantitative evaluation in a variety of samples (Floyd *et al* 2004, 2006, Kapadia *et al* 2005, 2006c), most of which have been high-density elements with very low hydrogen content. Hydrogen, a

large constituent of biological tissue, is a primary generator of neutron scatter, which adds a significant level of noise to the NSECT system. Neutrons scattering by the sample interact with materials around the target (including instrumentation apparatus, shielding material and room constituents) leading to inelastic scatter gamma-ray emission from these materials, which is detected as noise along with signal from the sample. This study aims at achieving two objectives: (i) investigating the feasibility of detecting liver iron in the presence of scatter noise generated by the human torso and (ii) obtaining an estimate of the minimum concentration of iron that can be detected in the human torso with the current acquisition setup.

2. Materials and methods

2.1. Materials

Bovine liver was used as liver tissue of choice in this experiment for several reasons. First, fresh bovine liver is easily available in large quantities. Second, there is considerable overlap in elements reported in the human and bovine liver (ICRU 1992, NIST). Third, it is easy to create artificial iron overload model phantoms by inserting iron into required regions of the bovine liver phantom. Thus, even though this study has been performed on a bovine liver model, the results are broadly transferable to a human liver.
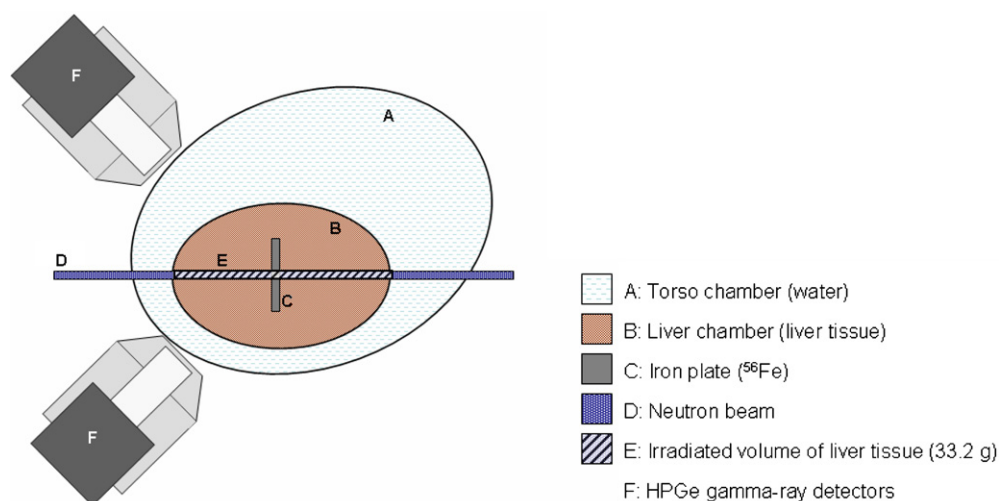
2.2. Disease model phantom

A model of iron overload in the human body was created using bovine liver tissue housed inside a human torso phantom, with uniform iron overload in the form of a solid plate of natural density iron. Due to the geometry of spectroscopic scanning, the concentration of excess iron was distributed uniformly across the entire volume of the liver tissue illuminated by the neutron beam. A uniform iron distribution forms one possible scenario of iron overload in the liver and can be detected through single-position spectroscopy without the need for a tomographic scan. As this scenario is the focus of the present study, a uniform iron distribution model was selected for this experiment to evaluate the feasibility of the spectroscopic technique. The construction of the phantom is described below.

The human torso phantom, shown in figure 1, is a dual-chamber plastic phantom of an adult human torso originally designed for nuclear medicine studies. It has two primary chambers—an outer chamber representing an adult torso and an inner chamber representing a typically sized adult human liver. The torso chamber measures 12 inches in height, 10 inches in diameter, 7.5 inches in depth, and has a volume of 11 200 ml. The inner liver chamber measures 5.5 inches in height and has a volume of 1520 ml. Volumes of both chambers were measured individually by measuring the amount of liquid required to fill each chamber separately. For the spectroscopic neutron scan, the outer torso chamber was filled with water and the inner liver chamber was filled with fresh bovine liver tissue.

Natural density iron was used to create a uniform distribution of iron overload in the liver chamber of the phantom. A square iron plate measuring 5 cm in height and 2.4 mm in thickness was inserted in a region of the liver illuminated by the neutron beam. The geometry of the scan was aligned to ensure that the beam was perpendicular to the face of the iron plate, and the entire beam illuminated the thickness of the plate. As the phantom was scanned with single-position spectroscopy, any iron in the path of the neutron beam would appear to be distributed along the entire volume of the liver illuminated by the neutron beam, thereby modeling a uniform distribution of iron overload in the liver. The acquisition geometry is shown in figure 2. In the iron overload phantom in this experiment, 4.18 g of iron were present in 33.2 g of

Figure 1. The dual-chamber human torso plastic phantom showing its two chambers. The outer chamber measuring 11 200 ml corresponds to an adult human torso, and the inner chamber measuring 1520 ml represents a typical-sized adult human liver. Both chambers can be filled separately with any desired material.

A: Torso chamber (water)
B: Liver chamber (liver tissue)
C: Iron plate (^{56}Fe)
D: Neutron beam
E: Irradiated volume of liver tissue (33.2 g)
F: HPGe gamma-ray detectors

Figure 2. Schematic of the NSECT acquisition geometry for the liver scan. Iron overload was created in the liver tissue using a natural density iron plate. The mass of iron in the path of the neutron beam appeared to be distributed uniformly within the illuminated volume of the liver tissue (shown using gray stripes). The iron concentration obtained with this acquisition geometry was determined to be 126.1 mg g^{-1}.

tissue illuminated by a 1.3 cm $\times$ 1.7 cm rectangular neutron beam. From these measurements, the iron concentration in this phantom was calculated as 126.1 mg per gram (mg g^{-1}) of liver tissue. As this experiment is the first study of its nature with no previously known estimates of concentration for comparison, the value of iron concentration used here was set high enough to be detected with adequate statistical accuracy in the gamma-ray detectors.

The natural density iron plate is a mixture of the naturally occurring stable isotopes of iron, ^{54}Fe (5.8%), ^{56}Fe (91.8%), ^{57}Fe (2.2%) and ^{58}Fe (0.3%). While all four isotopes of iron are present in the sample, our early experiments and simulation studies demonstrate that at incident neutron energies of 5 MeV, gamma lines can be detected from four prominent transitions in ^{56}Fe (at 847 keV, 1038 keV, 1238 keV and 1811 keV) and one in ^{54}Fe (at 1408 keV) (Floyd *et al* 2008, Kapadia 2007). Energy transitions from the remaining isotopes are not detected clearly, likely due to a combination of low neutron cross-section and low concentrations of the remaining isotopes in the sample. Further, the five prominent transitions described above can be detected only when the sample contains a significantly high concentration of iron (as in the case of natural density solid iron) and is scanned in a noise-free environment, i.e. one that does not generate a large quantity of neutron scatter. In scans of biological tissue containing modest quantities of iron, only the first excited state in ^{56}Fe (at 847 keV) is observed clearly (Kapadia *et al* 2005). Therefore, only the 847 keV gamma line from ^{56}Fe has been reported and used in the quantification experiment. The 847 keV gamma line is relatively free from contaminating contributions from other elements in the sample. For example, radioactive manganese (^{56}Mn) emits gamma ray at 847 keV and can lead to errors in iron measurement through contamination of the 847 keV peak. However, a combination of very low ^{55}Mn content in the sample and selection of a monochromatic fast-neutron beam makes the contribution of ^{55}Mn negligible.

2.3. Experimental setup

The NSECT experiments in this study were performed at the Triangle Universities Nuclear Laboratories at Duke University, Durham, NC. The experimental setup contains three major components, the neutron source, gamma detectors and a neutron-flux monitor. A schematic of the acquisition system is shown in figure 2 and a brief description of the individual components is provided below. Detailed description of the NSECT system hardware has been provided elsewhere (Floyd *et al* 2004, 2006, 2007, Kapadia *et al* 2008)

A Van-de-Graaff tunable accelerator was used to generate a 5 MeV pulsed neutron beam through the ^{2}H(d, n)^{3}He reaction by directing an accelerated and pulsed beam of deuterons onto a deuterium gas target. While the tandem Van-de-Graaff accelerator allows the production of mono-energetic neutron beams with energies between 3.5 MeV and 23 MeV, an energy of 5 MeV was selected for this study in order to excite energy levels in ^{56}Fe (at 847 keV) and ^{12}C (at 4.4 MeV). The beam was pulsed to provide 2 ns wide bunches at the target, with a repetition rate adjustable from 2.5 MHz down to 39 kHz. Beam pulsing was used to facilitate time-of-flight (TOF) background correction through measurement of neutron and gamma TOF. Gamma emission originating from neutron interactions observed in beam pulses was acquired and retained as foreground data, while data acquired during the time gap between pulses were used to obtain a measure of background effects and subtracted from the foreground data. The TOF application for NSECT has been described in detail in an earlier study (Floyd *et al* 2007). The 5 MeV neutron beam was collimated to a rectangular profile measuring 1.7 cm in height and 1.3 cm in width at the target.

Two high-purity germanium (HPGe) gamma-ray detectors were used to acquire the emitted gamma spectrum showing gamma lines corresponding to energy transitions in various samples. The HPGe detectors used in this study were two-fold segmented clover detectors (CLOVER 4×50×80 SEG2) manufactured by Canberra Eurysis S.A. Each detector comprised four co-axial n-type germanium crystals mounted together in the shape of a four-leaf clover, with each germanium crystal measuring 50 mm in diameter and 80 mm in length. The detectors were rated for minimum relative efficiency of 22% and full width at half maximum less than or equal to 2.25 keV for 1.33 MeV gamma rays of ^{60}Co. Both detectors used in

this study were calibrated against known energy peaks from a ^{22}Na source and positioned at $\pm135°$ from the incident neutron beam. Backward angles of 135° were selected to minimize detector activation and detector damage from forward scattering neutrons.

Neutron beam flux was monitored with a 1.6 mm thick plastic scintillator attached to a photomultiplier tube placed before the sample. Neutron attenuation from this scintillator was measured to be less than 0.5% at 5 MeV. Data from the scintillator were used to obtain an estimate of the total number of neutrons incident on the sample, which is required for dose calculation and to correct for minor temporal fluctuations in the flux of the neutron beam.

The iron overload phantom was scanned with the 5 MeV pulsed beam using single-position spectroscopy. Scanning was continued until 95% statistical accuracy was obtained in the gamma-ray detectors for gamma energy peaks corresponding to excited states from natural iron (^{56}Fe). After the torso phantom scan was completed, the iron plate was removed from the phantom and scanned again to obtain a spectrum corresponding to the iron plate without scatter from the torso. This iron spectrum was compared with the overload torso phantom spectrum to get an estimate of scatter generated by an adult human torso. Source and detector calibration was left unchanged between the two sample scans.

2.4. Data analysis

Data obtained in this experiment were reconstructed and analyzed in three steps, spectral reconstruction, background correction and spectral analysis as follows.

2.4.1. Spectral reconstruction. Spectra were reconstructed from acquired data using SpecTcl to plot gamma counts detected as a function of energy for each detector. SpecTcl is a nuclear event data acquisition and analysis package developed at the National Superconducting Cyclotron Laboratory at Michigan State University (Fox *et al* 2004). The software package facilitates acquisition and storage of raw nuclear data using an object-oriented C^{++} framework and allows online and offline retrieval of complete and partial data sets. Visualization is enabled through the Xamine display program. Data sets can be retrieved and analyzed using any combination of acquisition parameters and displayed with features such as spectrum overlay of multiple acquisitions. Spectra were reconstructed separately for each of the eight crystals of the HPGe detectors and summed to obtain the final energy spectrum.

2.4.2. Background correction. Background correction was performed using the time-of-flight (TOF) subtraction technique (Håkansson 1999) and sample-out background subtraction techniques as applied to NSECT (Floyd *et al* 2007). TOF gating information was acquired using the pulsed neutron beam simultaneously with the sample data and was used to reduce time-uncorrelated background from the resulting gamma spectra. The TOF technique is easily implemented in TUNL through readily available beam pulsing and TOF hardware, and provides the added advantage of being able to acquire background simultaneously with the foreground without the need for an additional sample-out scan. Figure 3 shows a TOF spectrum from the iron overload phantom, acquired during time gaps between neutron beam pulses. Three primary background effects can be observed in the spectrum: (a) a sharp peak at 2224 keV originating from neutron capture on hydrogen, (b) a sharp peak at 1461 keV originating from decay of ^{40}K in the acquisition room and (c) a gradual rise in gamma counts observed at lower energies originating from Compton scattering of detected gamma rays. The first two effects directly cancel out after TOF subtraction while the Compton scatter effect is corrected using a polynomial curve-fit subtraction. The latter subtraction technique, described in Kapadia *et al* (2008), uses a polynomial curve fit to obtain an estimate of the Compton

Time-of-flight Background Noise Spectrum
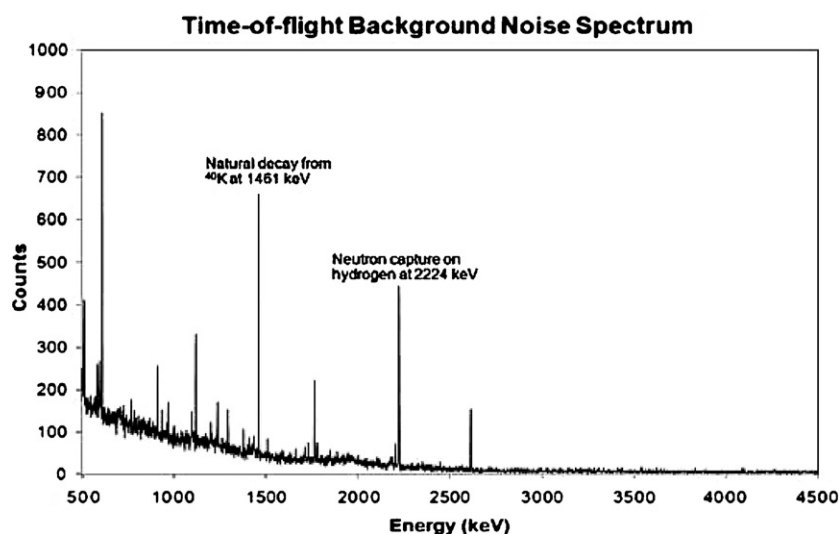
Figure 3. Time-of-flight background noise observed during experimental scanning of the iron-overloaded liver. The spectrum shows gamma counts that are observed during the time gaps between neutron pulses. Noise effects that dominate the spectrum include neutron capture on hydrogen (at 2.2 MeV) and natural decay of ^{40}K from the experiment room (labeled peaks). The remaining peaks in the spectrum are primarily from germanium in the detectors. The spectrum is used to subtract these noise effects from the torso signal spectrum.
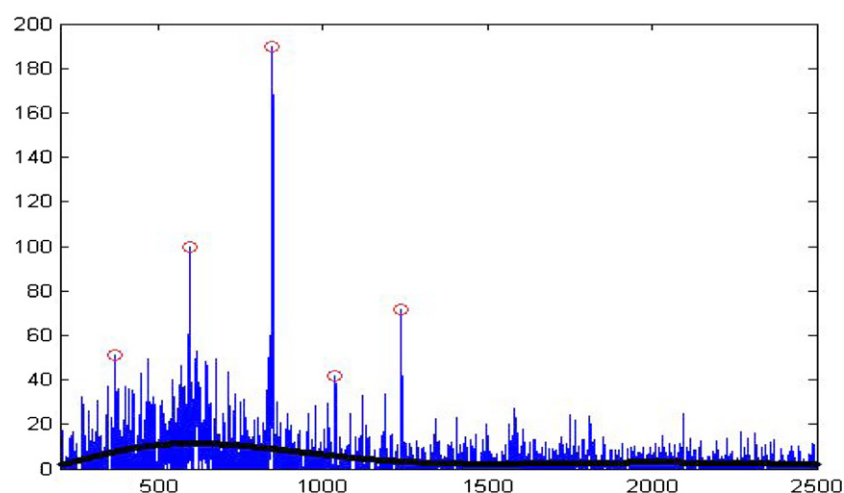
Figure 4. Example of automatic peak-detection algorithm applied to a sample iron spectrum. The spectrum is background-corrected. The superimposed black line shows the polynomial curve-fit pseudo-background used for calculating the peak-defining threshold. Energies identified as peaks are indicated by circles. For this iron spectrum, the identifier shows peaks at 369 and 595 keV corresponding to germanium, and at 847, 1037 and 1238 keV corresponding to iron.

scatter background (similar to the solid black line in figure 4) and subtracts the background from the signal.

TOF gating and subtraction was performed using SpecTcl. An estimate of the room-related sources of background was obtained by acquiring data from the empty room at the

beginning of the scan. While these data are able to account for room-related sources of background such as decay of ^{40}K, they cannot take into account the sample-dependent noise generated by interactions between neutrons scattered in the phantom and elements in detection instruments around the experiment area. For example, this empty room acquisition is not able to account for energy peaks in the spectra resulting from germanium in the detectors, aluminum in the detector mounting assembly and hydrogen from neutron capture in water amongst other elements. These sources of noise may be corrected by acquiring a gamma spectrum from a water sample of the same mass as the torso and subtracting it from the liver spectrum. However, this correction has not been performed in this experiment in order to be able to evaluate the feasibility of detecting iron overload in the presence of this sample-dependent noise.

2.4.3. Spectral analysis. Background-corrected spectra from each scan were analyzed for the presence of gamma energy peaks using an automatic peak-detection algorithm designed for NSECT (Bender *et al* 2007). As originally designed, this algorithm looks for energy peaks with heights above a user-specified minimum threshold within a user-specified energy window and identifies energy peaks whose two-tailed p-value above the underlying background is $p \leqslant 0.05$ using a z-score test. Energy peaks with heights below the absolute threshold are not reported. While this technique works adequately for small energy ranges ($\sim$1 MeV), it presents a potential problem for the larger energy range ($\sim$4 MeV) used in this analysis. The HPGe gamma detectors used during data acquisition exhibit an energy-dependent decrease in efficiency of gamma-ray detection, where the detection efficiency of the crystal drops off as a function of the gamma energy. As a result, the detection efficiency at the upper end of the spectrum is lower, leading to gamma lines at the upper end of the spectrum being reported with lower peak values. Therefore, even though an energy peak may be real and significant, using an absolute detection threshold may lead to missed identification of a peak at higher energies. To prevent this missed identification event, the peak-detection algorithm was modified as follows. A pseudo-background was modeled using a 5th degree polynomial curve fit to the detector data. The peak height threshold was determined dynamically as a function of this pseudo-background for each channel of the detector. Thus, as the heights of the detected gammas at higher energies decreased, the value of the pseudo-background decreased simultaneously, thereby decreasing the threshold value for peak identification at higher gamma energies. An example of the algorithm's operation applied to the Fe plate spectrum is shown in figure 4. The solid (blue) line shows the original background-corrected spectrum. The black line shows the pseudo-background fit used to generate the peak threshold. Energy peaks identified with p-values $\leqslant$0.05 are shown by the circles. For this experiment, the peak threshold was set at a factor of 4 higher than the background, and the element detection window width was set at $\pm$6 keV. These values were optimized through a separate study (Bender *et al* 2007). Note that the pseudo-background employed here was used only to determine the peak-identification threshold only. No background correction or subtraction was performed using this fit.

Energy values reported as significant peaks were then compared against Brookhaven National Laboratory's National Nuclear Database (National Nuclear Data Center 2007) using the gamma level search tool web interface to obtain a list of probable element matches.

2.5. Sample validation through NAA analysis

The liver sample was sent for neutron activation analysis (NAA) to determine the naturally occurring concentration of iron in the tissue in order to ensure that the iron detected in the torso scan was from the iron plate alone and not from a prior abnormally high liver
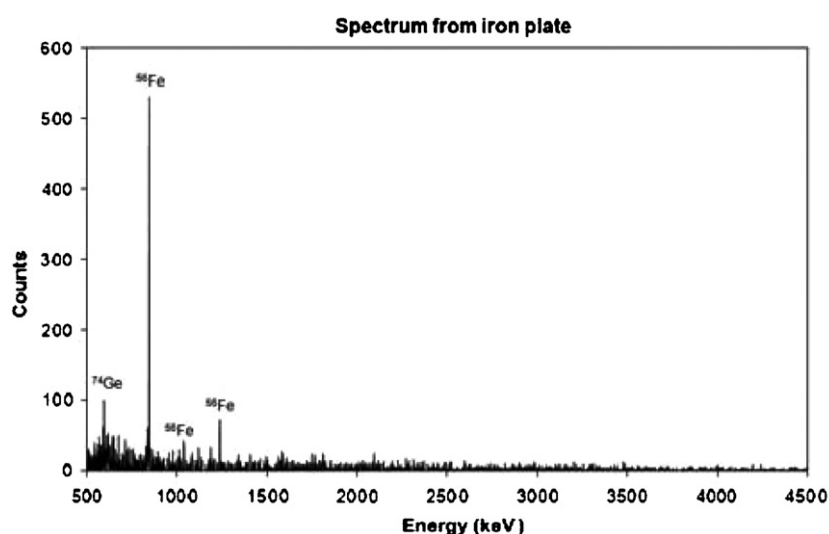
Figure 5. Gamma energy spectrum from the solid iron plate showing peaks corresponding to ^{56}Fe from the sample. An energy peak is also seen for ^{74}Ge from the detector.

Table 1. List of elements identified in the NSECT spectrum of the liver and confirmed through neutron activation analysis (NAA). The NSECT element identification was performed prior to NAA of the sample to eliminate identification bias.

Element	Energy peaks (keV)	Concentration reported in NAA (mg g^{-1})
Cl	1944	0.90
Cu	422, 645	0.09
Fe	847	0.06
K	1377, 1960	3.18
Na	440, 629	0.68
Zn	629	0.05

iron concentration. NAA is considered the gold standard in tissue element quantification and demonstrates microgram sensitivity for several elements of biological interest including iron. NAA sensitivity for ^{56}Fe has been reported as 90 mg with a short irradiation (Madison Nuclear Reactor Laboratory). A multi-element NAA analysis was performed to determine the quantity of iron and identify other elements in the liver sample as follows. A wet liver tissue sample was placed in a plastic vial and irradiated for 30 min with a flux of 1.8×10^{12} n cm^{-2} s^{-1}. Activity from the isotopes produced was counted at different times after irradiation, ranging from 1 min (for short-lived isotopes) to 3 weeks (for long-lived isotopes). The detected isotopes were used to establish a measure of the mass and concentration of the element present in the liver tissue sample. The NAA multi-element survey was able to confirm the presence of six elements detected in the NSECT scan (shown in table 1).

3. Results

3.1. Reconstructed spectra

Figure 5 shows the gamma energy spectrum from the NSECT acquisition of the 2.4 mm thick Fe plate. Peaks for ^{56}Fe are seen at 847 keV, 1039 keV and 1238 keV. The ^{56}Fe peak at
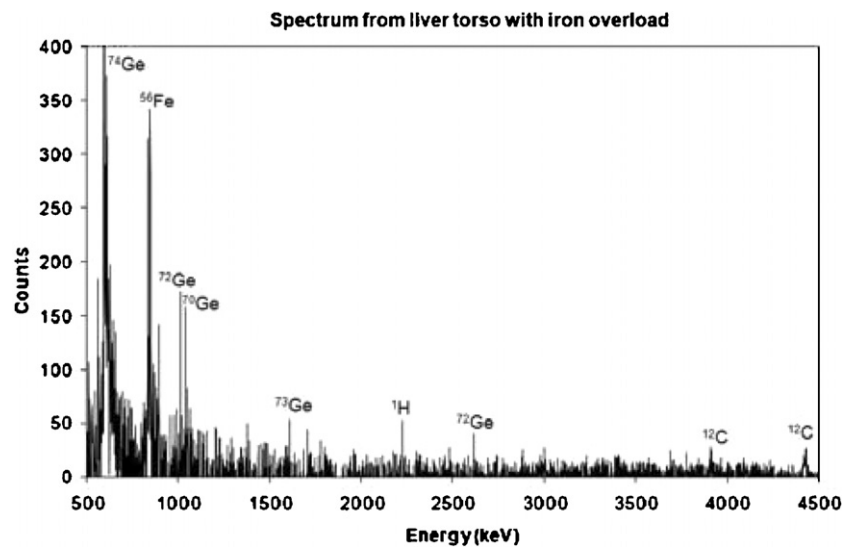
Figure 6. Gamma energy spectrum from the uniform iron overload torso phantom, showing peaks corresponding to several elements. The peak at 847 keV corresponds to ^{56}Fe. Peaks are also seen for Ge from the detector, and ^{12}C and ^{1}H from the tissue.

1811 keV was not strong enough to be detected by the peak-detection algorithm. A total of 1276 gamma photons were counted in the peak at 847 keV, corresponding to a known concentration of 4.18 g of ^{56}Fe. The spectrum also showed a peak at 595 keV, corresponding to ^{74}Ge in the detector.

Figure 6 shows the gamma energy spectrum from the iron-overloaded torso phantom. A strong peak was detected at 847 keV corresponding to 4.18 g of ^{56}Fe. A total of 1000 gamma photons were counted in this peak. Energy peaks were also identified for several other elements including ^{74}Ge and ^{76}Ge from the gamma-ray detectors, ^{42}K, ^{1}H (neutron capture) and ^{12}C from the phantom. A list of the elements detected in the NSECT spectrum and verified through the NAA multi-element survey is given in table 1.

Six elements detected in the NSECT spectrum were confirmed through NAA. While each of these elements was present in the sample, their concentration was too low to be accurately quantified through NSECT. It can be noted from table 1 that the value of iron in the sample is extremely low. This value represents the naturally occurring concentration of iron in the liver tissue without the overload condition.

3.2. Spectral analysis of iron peaks

As one of the designated criteria in the peak-detection algorithm was that the peak must be detected above background with p-value $\leqslant 0.05$, all the peaks reported in the spectral analysis have $p \leqslant 0.05$ calculated using a z-score test for difference of means. For the peak at 847 keV corresponding to ^{56}Fe, 1000 peak counts were detected above an underlying background of 120 counts, corresponding to $p \leqslant 0.001$. The underlying background counts were measured using the pseudo-background polynomial curve fit used to model the dynamic threshold as shown in figure 4.

Table 2 presents an estimate of the neutron attenuation observed in the torso phantom calculated using the plate of natural iron. Gamma counts were obtained from the iron plate
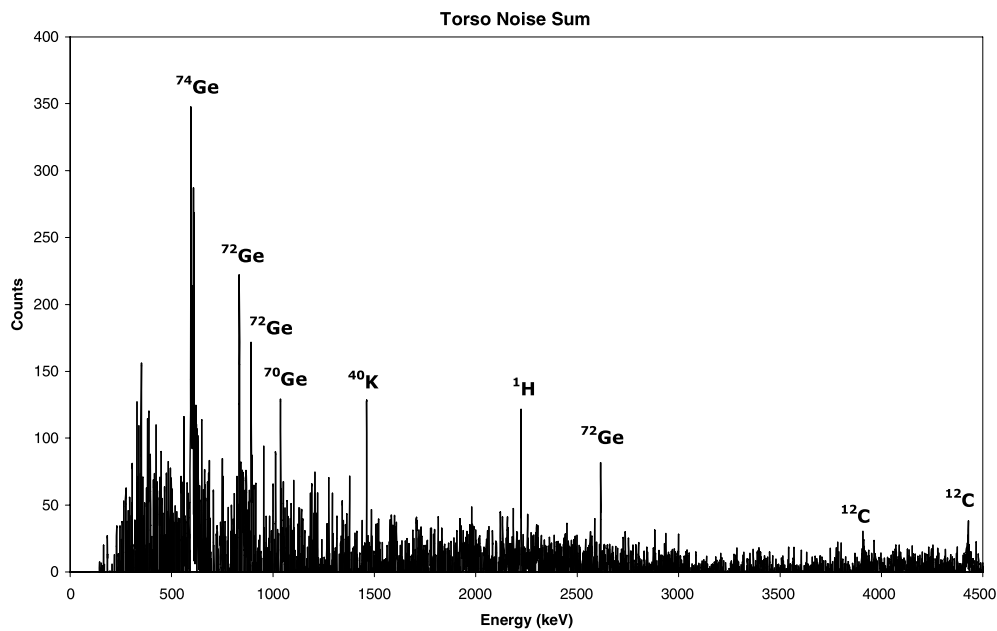
Figure 7. Subtraction spectrum of the torso phantom without iron.

Table 2. Calculation of neutron and gamma attenuation ratio in the human torso.

	847 keV counts	Neutron paddle counts	Normalized counts	Ratio of normalized counts
Fe plate in air	1276	755 46	16.9×10^{-3}	$\frac{\text{Plate\_in\_air}}{\text{Plate\_in\_torso}} = 3.15$
Fe plate in torso phantom	1000	186 443	5.36×10^{-3}	

placed in air and normalized to the incident neutron counts observed in the neutron paddle. A similar measurement was performed with the iron plate placed in the torso phantom surrounded by liver tissue. The ratio of the normalized gamma counts in air to normalized gamma counts in the torso phantom was used to obtain an estimate of the attenuation due to the torso. As shown in table 2, a normalized value of 16.9×10^{-3} was observed for the plate in air, while a normalized value of 5.36×10^{-3} was observed for the same plate placed in the torso. The ratio of the two values resulted in an attenuation factor of 3.15. Based on the known dimensions of the phantom, the corresponding theoretical value of attenuation was then calculated using an algorithm designed for attenuation correction in NSECT (Kapadia and Floyd 2005). The calculated value was found to be 2.44, representing a 30% difference from the measured value.

Figure 7 shows the difference spectrum of the overload torso phantom and the iron plate, generated by subtracting the normalized iron spectrum (figure 5) from the torso liver spectrum (figure 6). It can be seen in the subtracted spectrum that the peaks from ^{56}Fe at 847 keV and 1238 keV are difficult to identify, while the peak from neutron capture on ^{1}H at 2224 keV and peaks from ^{12}C at 4439 keV and 3928 keV (escape peak) are identified clearly. Therefore, it is possible to conclude that the peaks at 847 keV and 1238 keV originate from the external source of iron, i.e. the 2.4 mm thick iron plate, while the remaining peaks originate from elements in the liver tissue.

Table 3. Effective dose delivered from NSECT spectroscopy scan of the torso.

Parameter	Calculated value
Number of incident neutrons	3.21×10^7
Total energy deposited (MeV)	1.56×10^8
Total energy deposited (J)	2.49×10^{-5}
Mass of liver (kg)	3.32×10^{-2}
Absorbed dose (J kg^{-1}) Gy	7.50×10^{-4}
Neutron radiation weighting factor	10
Equivalent dose (Gy)	7.50×10^{-3}
Tissue weighting factor for liver	0.05
Effective dose equivalent (mSv)	$3.75 \times 10^{-1} = 0.375$ mSv

3.3. Patient dose

The patient dose for this study was calculated by using a GEANT4 model to determine the amount of energy deposited per neutron in a human liver torso and multiplying this information by the total neutron fluence incident on the torso phantom. The GEANT4 model for dose calculation has been developed and described elsewhere (Kapadia 2007, Sharma *et al* 2007), and results from the model were directly used to calculate dose values for this experiment. The number of neutrons incident on the sample was calculated from data acquired by the thin scintillation paddle detector and the zero-degree liquid scintillator neutron monitor. A neutron scan with no sample in the beam was used to establish a ratio of scintillation paddle counts to zero-degree liquid scintillator counts. The neutron detection efficiency of the zero-degree scintillator was known *a priori*. From this scan, the ratio of scintillator paddle counts to neutron flux was established as 172 neutrons per scintillator paddle count. Therefore, it was possible to estimate that the torso scan with 186 443 paddle counts was performed using 3.21×10^7 incident neutrons. The GEANT4 simulation was used to establish a ratio of the energy deposited in the torso per incident neutron as 4.85 MeV per neutron. The dose calculation for this scan is shown in table 3 and is explained as follows:

- The total number of neutrons required for spectroscopic quantification $= 3.21 \times 10^7$.
- The total energy deposited (MeV) $=$ total number of neutrons $\times$ energy deposited per neutron.
- The total energy deposited (J) $=$ total energy deposited (MeV) $\times 1.6 \times 10^{-13}$ J MeV^{-1}.
- Absorbed dose (Gy) $=$ total energy deposited (J)/mass of irradiated tissue (kg).
- Radiation weighting factor for neutrons at 5 MeV $= 10$.
- Equivalent dose (Gy) $=$ absorbed dose (Gy) $\times$ radiation weighting factor.
- Tissue weighting factor for liver $= 0.05$.
- Effective dose equivalent (Sv) $=$ equivalent dose (Gy) $\times$ liver tissue weighting factor.

The detection limit observed in the study was 0.2 g with a dose of 0.375 mSv, corresponding to a liver iron concentration of 6 mg g^{-1}.

4. Discussion

This paper describes the first experiment to determine the feasibility of detecting iron overload in humans. Results from the experiment suggest that in its current form NSECT shows significant potential in being able to diagnose clinical iron overload in the human liver through

a scan that is both non-invasive and *in vivo*. Clinical iron overload in patients has been reported with concentrations between 1.8 mg g^{-1} and 5.45 mg g^{-1} for moderate to severe cases (Powell 2002, 2005, Powell *et al* 1998), and up to 9 mg g^{-1} in very severe cases (Mazza *et al* 1995, Scharfetter *et al* 2003). As this experiment was the first study of its nature with no previous NSECT diagnostic values for comparison, the iron overload in this experiment was set at 126 mg g^{-1}, approximately 20 times the typical limit reported in patients, in order to ensure adequate signal and accuracy from the system. However, the results from this experiment can be used to obtain a projected sensitivity for iron overload diagnosis as follows. In the torso phantom scan, the noise background under the peak corresponding to ^{56}Fe was determined to have a maximum height of 30 counts. With this noise background, for a peak to be determined with a *p*-value of $\leqslant 0.05$, the number of counts in the foreground peak would have to be 48, which, based on the iron concentration in this phantom, corresponds to an iron concentration of 0.2 g. This concentration of 0.2 g distributed over the 33.2 g of liver tissue scanned corresponds to an iron overload of 6 mg g^{-1}, which represents a clinically relevant value.

NSECT relies on the total quantity of iron that is present in the beam during a scan. Therefore, in order to increase signal strength in the case of low concentration livers, the acquisition geometry can be optimized to illuminate a larger volume of liver tissue (and consequently include more iron in the beam) while minimizing the illumination of surrounding tissue in the torso. Further, specialized components such as high-flux neutron sources and multiple gamma detectors can be used to increase the overall detection efficiency of the system and reduce scan time, which will both in turn reduce the time-dependent background noise. Implementing optimized detector shielding can reduce sample-related and room-related background, which will increase the signal-to-noise ratio and improve the overall sensitivity of the system. Increased gamma detection efficiency with reduced scan time will also reduce the levels of patient dose. Such system optimization has the potential to improve the sensitivity of the technique to facilitate the diagnosis of even lower concentrations of iron overload (less than 5 mg g^{-1}). System optimization has been explored using GEANT4 simulations (Kapadia 2007).

Although MRI is able to quantify moderate concentrations of iron overload, it suffers from a loss of accuracy for concentrations above 6 mg g^{-1} wet weight (20 mg g^{-1} dry weight) due to the signal intensity from the liver being reduced by high concentration of iron (Angelucci *et al* 1997). NSECT on the other hand shows an increase in the signal with increasing concentrations of iron in the beam, and therefore has the ability to detect severe degrees of iron overload in patients where MRI begins to lose accuracy. The experiment described in this paper demonstrates that NSECT in its current form can detect and quantify liver iron concentrations of 6 mg g^{-1} or higher and has the potential to detect lower concentrations by scanning a larger volume of tissue with an optimized acquisition geometry.

The acquisition technique described in this study is that of single-position spectroscopy, where a thin neutron beam is used to illuminate a given volume of the tissue. Due to the nature of the spectroscopic acquisition, any iron present at any given location in the illuminated tissue appears to be distributed uniformly along the entire volume of the tissue. This mode of acquisition, therefore, is unable to identify high concentrations of iron located in small localized regions along the illuminated tissue volume. Localized iron concentrations will appear to be distributed uniformly along the entire tissue volume, with concentration that is lower than that in the original localized region. Detection of non-uniform distributions will require tomographic scanning of the patient. Although future clinical applicability of NSECT may appear to be more practical using the tomographic acquisition mode, it is important to understand the behavior of each individual projection in order to determine the optimal technique of generating a tomographic image. Further, through its tomographic mode of

acquisition, NSECT has the ability to investigate the effect of factors such as cirrhosis on the distribution of iron in liver iron overload.

Background correction was performed using TOF correction to reduce time-uncorrelated noise events and a beam-only scan to reduce effects from beam-correlated noise events from materials in the system. Noise generated from interactions between neutrons scattered in the human torso and materials in the experimental area other than the sample was not suppressed. In other experiments, this background has been suppressed using a spectrum obtained from an equivalent volume of water to model the neutron scatter background (Kapadia *et al* 2005, 2006a, 2006b, 2006c, 2008). In a clinical scenario, this scatter background can be corrected by subtracting a spectrum acquired from an equivalent volume water sample. Reducing scatter background will further improve the sensitivity of the system, thereby making it possible to detect lower concentrations of iron in the liver.

Patient dose for this experiment was found to be 0.375 mSv, which is significantly lower than an abdominal x-ray exam that typically delivers 2 mSv (RSNA 2007). Although neutrons have a higher radiation weighting factor than gamma rays, it takes fewer neutrons to create an NSECT image than x-rays required to create a radiograph. Therefore, it is possible to maintain patient dose levels at values comparable to other ionizing radiation modalities. Further, using high-flux neutron sources and increasing the number of detectors can bring down patient dose and reduce scan time further.

The results described in this paper have two important outcomes. First, they demonstrate that NSECT has the potential to detect clinically relevant concentrations of iron in the human body through a non-invasive scan. Second, they provide a comparative standard to guide the design of iron overload phantoms for future liver iron quantification studies using NSECT.

Acknowledgments

References

Alustiza J M, Artetxe J, Castiella A, Agirre C, Emparanza J I, Otazua P, Garcia-Bengoechea M, Barrio J, Mujica F and Recondo J A 2004 MR quantification of hepatic iron concentration *Radiology* **230** 479–84
Angelucci E, Giovagnoni A, Valeri G, Paci E, Ripalti M, Muretto P, McLaren C, Brittenham G M and Lucarelli G 1997 Limitations of magnetic resonance imaging in measurement of hepatic iron *Blood* **90** 4736–42
Arnold M L, McNeill F E, Stronach I M, Pejovic-Milic A, Chettle D R and Waker A 2002 An accelerator based system for *in vivo* neutron activation analysis measurements of manganese in human hand bones *Med. Phys.* **29** 2718–24
Avrin W F and Kumar S 2007 Noninvasive liver–iron measurements with a room-temperature susceptometer *Physiol. Meas.* **28** 349–61
Bender J E, Kapadia A J, Sharma A C, Tourassi G D, Harrawood B P and Floyd C E 2007 Breast cancer detection using neutron stimulated emission computed tomography: prominent elements and dose requirements *Med. Phys.* **34** 3866–71
Bonkovsky H L, Rubin R B, Cable E E, Davidoff A, Rijcken T H and Stark D D 1999 Hepatic iron concentration: noninvasive estimation by means of MR imaging techniques *Radiology* **212** 227–34

Brittenham G and Badman D 2003 Noninvasive measurement of iron: report of an NIDDK workshop *Blood* **101** 15–9

Brittenham G M, Sheth S, Allen C J and Farrell D E 2001 Noninvasive methods for quantitative assessment of transfusional iron overload in sickle cell disease *Semin. Hematol.* **38** 37–56

Cecchin E, De Marchi S, Querin F, Marin M G, Fiorentino R and Tesio F 1990 Efficacy of hepatic computed tomography to detect iron overload in chronic hemodialysis *Kidney Int.* **37** 943–50

Chapman R W, Williams G, Bydder G, Dick R, Sherlock S and Kreel L 1980 Computed tomography for determining liver iron content in primary haemochromatosis *Br. Med. J.* **280** 440–2

Chezmar J L, Nelson R C, Malko J A and Bernardino M E 1990 Hepatic iron overload: diagnosis and quantification by noninvasive imaging *Gastrointest. Radiol.* **15** 27–31

Dixon R M, Styles P, al-Refaie F N, Kemp G J, Donohue S M, Wonke B, Hoffbrand A V, Radda G K and Rajagopalan B 1994 Assessment of hepatic iron overload in thalassemic patients by magnetic resonance spectroscopy *Hepatology* **19** 904–10

Floyd C E, Bender J E, Sharma A C, Kapadia A J, Xia J Q, Harrawood B P, Tourassi G D, Lo J Y, Crowell A S and Howell C R 2006 Introduction to neutron stimulated emission computed tomography *Phys. Med. Biol.* **51** 3375–90

Floyd C E *et al* 2004 Neutron stimulated emission computed tomography of stable isotopes *SPIE Medical Imaging* (San Diego, CA: IEEE) pp 248–54

Floyd C E *et al* 2007 Neutron stimulated emission computed tomography: background corrections *Nucl. Instrum. Methods Phys. Res.* B **254** 329–36

Floyd C E *et al* 2008 Neutron stimulated emission computed tomography of a multi-element phantom *Phys. Med. Biol.* **53** 2313–26

Fox R, Bolen C, Orji K and Venema J 2004 NSCLSpecTcl meeting the needs of preliminary nuclear physics data analysis *11th Ann. Tcl/Tk Conference* (New Orleans, Louisiana)

Gandon Y, Olivie D, Guyader D, Aube C, Oberti F, Sebille V and Deugnier Y 2004 Non-invasive assessment of hepatic iron stores by MRI *Lancet* **363** 357–62

Guyader D, Gandon Y, Robert J Y, Heautot J F, Jouanolle H, Jacquelinet C, Messner M, Deugnier Y and Brissot P 1992 Magnetic resonance imaging and assessment of liver iron content in genetic hemochromatosis *J. Hepatol.* **15** 304–8

Håkansson P 1999 An introduction to the time-of-flight technique *Braz. J. Phys.* **29** 422–7

Howard J M, Ghent C N, Carey L S, Flanagan P R and Valberg L S 1983 Diagnostic efficacy of hepatic computed tomography in the detection of body iron overload *Gastroenterology* **84** 209–15

ICRU 1992 Photon, Electron, Proton and Neutron Interaction Data for Body Tissues *ICRU Report No 46* (Bethesda, MD: ICRU)

Kapadia A J 2007 Accuracy and patient dose in neutron stimulated emission computed tomography for diagnosis of liver iron overload: simulations in GEANT4 *Biomedical Engineering* (Durham, NC: Duke University)

Kapadia A J and Floyd C E 2005 An attenuation correction technique to correct for neutron and gamma attenuation in the reconstructed image of a neutron stimulated emission computed tomography (NSECT) system *SPIE Medical Imaging* (San Diego, CA: IEEE) pp 737–43

Kapadia A J, Floyd C E, Bender J E, Howell C R, Crowell A S and Kiser M R 2005 Non-invasive quantification of iron 56-Fe in beef liver using neutron stimulated emission computed tomography *IEEE Nucl. Sci. Symp., Med. Imag. Conf.* **4** 2232–4

Kapadia A J, Sharma A C, Bender J E, Tourassi G D, Howell C R, Crowell A S, Kiser M R, Harrawood B P and Floyd C E 2008 Neutron stimulated emission computed tomography for diagnosis of breast cancer *IEEE Trans. Nucl. Sci.* **55** 501–9

Kapadia A J, Sharma A C, Tourassi G D, Bender J E, Crowell A S, Kiser M R, Howell C R and Floyd C E 2006a Neutron spectroscopy of mouse using neutron stimulated emission computed tomography (NSECT) *IEEE Nucl. Sci. Symp., Med. Imag. Conf.* **6** 3546–8

Kapadia A J, Sharma A C, Tourassi G D, Bender J E, Crowell A S, Kiser M R, Howell C R and Floyd C E 2006b Neutron stimulated emission computed tomography (NSECT) for early detection of breast cancer *IEEE Nucl. Sci. Symp., Med. Imag. Conf.* **6** 3928–31

Kapadia A J, Sharma A C, Tourassi G D, Bender J E, Crowell A S, Kiser M R, Howell C R and Floyd C E 2006c Non-invasive estimation of potassium (39K) in bovine liver using neutron stimulated emission computed tomography (NSECT) *IEEE Nucl. Sci. Symp., Med. Imag. Conf.* **4** 2076–8

Katoh Y, Sato T and Yamamoto Y 2003 Use of instrumental neutron activation analysis to determine concentrations of multiple trace elements in human organs *Arch. Environ. Health* **58** 655–61

Knight G S, Beddoe A H, Streat S J and Hill G L 1986 Body composition of two human cadavers by neutron activation and chemical analysis *Am. J. Physiol. Endocrinol. Metab.* **250** E179–85

Liu P *et al* 1996 Quantification of cardiac and tissue iron by nuclear magnetic resonance relaxometry in a novel murine thalassemia-cardiac iron overload model *Can. J. Cardiol.* **12** 155–64

Madison Nuclear Reactor Laboratory *UW INAA: Estimated Interference-Free Sensitivity in Micrograms*

Mattsson S and Thomas B J 2006 Development of methods for body composition studies *Phys. Med. Biol.* **51** R203–28

Mazza P *et al* 1995 Iron overload in thalassemia: comparative analysis of magnetic resonance imaging, serum ferritin and iron content of the liver *Haematologica* **80** 398–404

McNeill F E, Franklin D M, Chettle D R, Ellis R E, Pittard S P, Scott M C and Vennart W 1990 Feasibility studies in the *in vivo* measurement of iron in synovial membrane *Basic Life Sci.* **55** 413–8

National Nuclear Data Center B N L 2007 *National Nuclear Database NuDat 2.3*

Ng K H, Bradley D A, Looi L M, Seman Mahmood C and Khalik Wood A 1993 Differentiation of elemental composition of normal and malignant breast tissue by instrumental neutron activation analysis *Appl. Radiat. Isot.* **44** 511–6

Nielsen P, Engelhardt R, Duerken M, Janka G E and Fischer R 2000 Using SQUID biomagnetic liver susceptometry in the treatment of thalassemia and other iron loading diseases *Transfus. Sci.* **23** 257–8

Nielsen P, Engelhardt R, Dullmann J and Fischer R 2002a Non-invasive liver iron quantification by SQUID-biosusceptometry and serum ferritin iron as new diagnostic parameters in hereditary hemochromatosis *Blood Cells Mol. Dis.* **29** 451–8

Nielsen P, Kordes U, Fischer R, Engelhardt R and Janka G E 2002b SQUID-biosusceptometry in iron overloaded patients with hematologic diseases *Klin. Padiatr.* **214** 218–22

NIH 2007 *NIH Publication No.* 07-4621

NIST *NIST-SRM 1577b Bovine Live*r http://www-naweb.iaea.org/nahu/nmrm/nmrm2003/material/ni1577b.htm accessed 4 April 2008

Perrimond H, Chagnon C, Moulanier I, Michel G, Guidicelli H and Bernard P J 1991 The value of nuclear magnetic resonance in the study of iron overload in thalassemia patients *Ann. Pediatr. (Paris)* **38** 175–84

Powell L W 2005 *Harrison's Principles of Internal Medicine* ed D Kasper, A S Fawci, D L Longo, E Braunwald, S L Hauser and J L Jameson (New York: McGraw-Hill) pp 2298–303

Powell L W 2002 Diagnosis of hemochromatosis *Semin. Gastrointest Dis.* **13** 80–8

Powell L W, George D K, McDonnell S M and Kowdley K V 1998 Diagnosis of hemochromatosis *Ann. Intern. Med.* **129** 925–31

Ratziu V, Charlotte F, Heurtier A, Gombert S, Giral P, Bruckert E, Grimaldi A, Capron F and Poynard T 2005 Sampling variability of liver biopsy in nonalcoholic fatty liver disease *Gastroenterology* **128** 1898–906

Regev A, Berho M, Jeffers L J, Milikowski C, Molina E G, Pyrsopoulos N T, Feng Z Z, Reddy K R and Schiff E R 2002 Sampling error and intraobserver variation in liver biopsy in patients with chronic HCV infection *Am. J. Gastroenterol.* **97** 2614–8

RSNA 2007 *Radiation Exposure in X-ray Examinations (USA: American College of Radiology (ACR) and the Radiological Society of North America (RSNA))*

Scharfetter H, Casanas R and Rosell J 2003 Biological tissue characterization by magnetic induction spectroscopy (MIS): requirements and limitations *IEEE Trans. Biomed. Eng.* **50** 870–80

Sharma A C, Harrawood B P, Bender J E, Tourassi G D and Kapadia A J 2007 Neutron stimulated emission computed tomography: a Monte Carlo simulation approach *Phys. Med. Biol.* **52** 6117–31

Sheth S 2003 SQUID biosusceptometry in the measurement of hepatic iron *Pediatr. Radiol.* **33** 373–7

Vartsky D, Ellis K J, Hull D M and Cohn S H 1979 Nuclear resonant scattering of gamma rays—a new technique for *in vivo* measurement of body iron stores *Phys. Med. Biol.* **24** 689–701

Vartsky D, Wielopolski L, Ellis K J and Cohn S H 1982 The use of nuclear resonant scattering of gamma-rays for *in vivo* measurement of iron *Nucl. Instrum. Methods Phys. Res.* **193** 359–64

Villeneuve J P, Bilodeau M, Lepage R, Cote J and Lefebvre M 1996 Variability in hepatic iron concentration measurement from needle-biopsy specimens *J. Hepatol.* **25** 172–7

Wang Z J, Haselgrove J C, Martin M B, Hubbard A M, Li S, Loomes K, Moore J R, Zhao H and Cohen A R 2002 Evaluation of iron overload by single voxel MRS measurement of liver T2 *J. Magn. Reson. Imag.* **15** 395–400

Wielopolski L, Ancona R C, Mossey R T, Vaswani A N and Cohn S H 1985 Nuclear resonance scattering measurement of human iron stores *Med. Phys.* **12** 401–4

Yukawa M, Suzuki-Yasumoto M, Amano K and Terai M 1980 Distribution of trace elements in the human body determined by neutron activation analysis *Arch. Environ. Health* **35** 36–44

Zeisler R, Ostapczuk P, Stone S F and Stoeppler M 1993 Effective tools for trace element characterization of tissue: neutron activation analysis and voltammetry *Sci. Total Environ.* **139/140** 403–10

GEANT4 Simulation of NSECT for Detection of Iron Overload in the Liver

Anuj J. Kapadia[a], Brian P. Harrawood[a], Georgia D. Tourassi[a,b]

[a]Duke Advanced Imaging Laboratories, Duke University Medical Center, Durham, NC 27705;
[b]Department of Medical Physics, Duke University, Durham, NC 27705

ABSTRACT

Neutron stimulated emission computed tomography (NSECT) is being proposed as a non-invasive technique to diagnose iron overload in humans. It uses inelastic scatter interactions between incident neutrons and iron nuclei to stimulate gamma-ray emission from iron. Tomographic detection of the emitted gamma-rays yields information about the concentration and spatial distribution of iron in the liver. Early proof-of-concept experiments have shown that NSECT has the potential to quantify clinical quantities of liver iron overload through single-position spectroscopy. However, a tomography application for patient diagnosis has never been tested. This work uses a Monte-Carlo simulation of a tomographic NSECT system to investigate the feasibility of imaging the spatial distribution of liver iron through tomography. A simulation of an NSECT system has been designed in GEANT4 and used to tomographically scan a simulated human liver phantom with high-concentration iron lesions. Images are reconstructed with the MLEM algorithm and analyzed for pixel values within iron regions to determine the statistical significance of detection. Analysis results indicate that a wet iron concentration of 3 mg/g can be detected in surrounding liver tissue with p-value ≤ 0.0001 for neutron exposure corresponding to a radiation dose of 0.72 mSv. The research performed here demonstrates that NSECT has the ability to image clinically relevant distributions of iron through tomographic scanning.

Keywords: Neutron, Spectroscopy, Gamma, Iron-overload, NSECT, Tomography, Simulation, GEANT4.

1. INTRODUCTION

Neutron stimulated emission computed tomography (NSECT) system is being developed as a non-invasive technique to quantitatively image the distribution of elements in the human body [1-5]. It uses inelastic scattering interactions between neutrons and target element nuclei to obtain a tomographic image of the element's spatial distribution in the body. NSECT uses the following principle. An incident neutron scatters inelastically with a target atomic nucleus and stimulates the nucleus to emit characteristic gamma radiation. The energy of the emitted gamma-ray is unique to the emitting isotope and can be measured to identify the distribution and concentration of the element in the sample. Translation and rotation of the sample yields tomographic information about the element's spatial distribution in the target. Such quantitative imaging has the potential to diagnose several disorders in the human body that are characterized by differences in element concentration between normal and diseased tissue. Element concentration differences have been observed in liver iron overload [6, 7], Alzheimer's disease [8, 9], and several cancers including breast [10-12], prostate[13] and brain [14-16]. While the imaging of element distribution in all of the above mentioned disorders is within the capabilities of NSECT, the present work is focused on detection of iron overload in the liver.

Iron overload is a condition in which the body's iron stores increase significantly due to iron accumulation through increased dietary absorption (hemochromatosis) or through blood transfusion that form a part of treatment procedures for chronic disorders such as thalassemia major, myelodysplasia and moderate aplastic anemia (transfusional iron overload). While the body has fine techniques for monitoring and controlling the absorption of iron ingested from food in accordance with its iron need, it has no corresponding mechanism to eliminate excess iron in case of overload. The excess quantity is stored in several vital organs in the body such as the liver, heart and spleen, and can lead to extensive tissue damage, liver cirrhosis, cardiac failure, hepatic failure and hepatocellular carcinoma [6, 17, 18].

Accurate measurement of the body's iron content is vital for effective diagnosis and management of iron overload [6, 17]. The measurement is currently obtained through a liver biopsy, which is an uncomfortable procedure. The discomfort and risks associated with biopsy significantly limit its acceptability to patients. NSECT has the ability to obtain an accurate estimate of iron concentration in the liver through a single non-invasive in-vivo scan. It provides an alternative to biopsy

with no associated morbidity. It can be used for repeated monitoring of patients obtaining therapeutic treatments for iron overload.

Preliminary experiments have demonstrated the clinical feasibility of detecting iron overload through a non-invasive 'neutron radio-biopsy'[19]. These experiments have achieved a statistically significant measurement of liver iron in a human iron-overload phantom through a single projection scan with a dose of less than 0.5 mSv. While the single-projection acquisition is appropriate for measuring uniform iron distributions in the liver, a tomographic acquisition is required to image and quantify non-uniform patches of high iron concentration in otherwise normal liver tissue. However, before experimental implementation of a clinical tomography system is begun, it is important to determine the ability of NSECT for detecting non-uniform iron overload in humans with reasonable radiation dose. This work uses a Monte-Carlo simulation to test the feasibility of detecting non-uniform distributions of iron in the liver through a tomographic NSECT scan.

2. METHODOLOGY

A Monte-Carlo simulation of a clinical NSECT system is designed in GEANT4. GEANT4 is a programming toolkit to model high-energy physics interactions between particles and matter over a broad range of energies[20]. It has been developed by a worldwide collaboration of over 100 scientists in Europe, Russia, Japan, Canada and the United States. GEANT4 allows precise modeling of interactions that occur between neutrons and a variety of target nuclei at energies of relevance to NSECT. It is an object-oriented programming package which incorporates a powerful set of random number generators, physics units and constants, and provides all the tools required for detector simulation including geometry, tracking and detector response management.

2.1 Experimental System

The NSECT simulation is modeled after the experimental system, which uses a Van-de-Graaff accelerator source, high-purity germanium gamma-ray detectors, and a tomographic gantry to accommodate the sample. The experimental system has been described in detail elsewhere [1, 2, 4], and only a brief description is provided here. A Van-de-Graaff accelerator is used to generate mono-energetic neutron beams with energies ranging from 4 MeV and 7.5 MeV for NSECT imaging. Beam width is controlled by a copper collimator with swappable inserts. High-purity germanium (HPGe) gamma-ray detectors are used to generate gamma energy spectra with approximate energy resolution of 1 keV per detector channel. Tomography is performed using the translate-rotate geometry of first generation CT scanners using a gantry to hold and control the sample remotely.

2.2 Simulated Model

The simulated NSECT model consists of 3 components – (a) Neutron Source, (b) Gamma Detectors, and (c) Liver Phantom, each designed independently based on the corresponding component of the experimental acquisition system.

2.2.1 Neutron Source

The simulated neutron source produces a 5 MeV mono-energetic neutron beam collimated to 1 cm beam width. These parameters are typical of the beam used in NSECT experiments. Neutrons with 5 MeV of energy are sufficient to excite several energy states in iron as well as the first excited state in carbon in the liver. Carbon can be used to image the location of the liver within the abdomen and also to obtain an image of tissue distribution which can be used for attenuation correction.

2.2.2 Gamma-ray Detectors

The detector system is designed as an array of six germanium crystals that surround the liver sample as shown in figure 1. Four detectors are located at ±45 degrees and ±135 degrees around the sample and two are above and below the sample. The ±45 degree and ±135 degree locations correspond to regions of maximum gamma emission around the sample from electric quadrupole interactions, which are expected to be dominant at this neutron energy. While the experimental setup uses detectors only in the 135 degree positions to minimize detector damage from scattered neutrons, the 45 degree position is included here to increase detection efficiency. The two detectors located above and below the liver sample serve to further increase gamma-ray detection efficiency in the simulated system. Each detector is designed as a cylinder of 30 cm diameter and 10 cm height and is filled with natural density germanium. The detector material is sensitized to track particle transport and energy deposit in its volume.
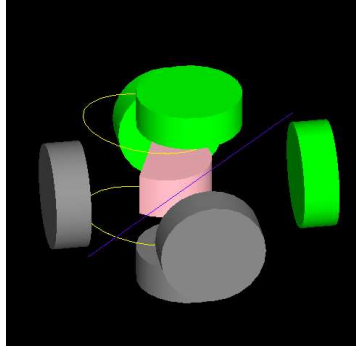
Figure 1. GEANT4 simulation showing the 6-detector array system. The green and gray cylinders are gamma detectors. The liver is shown as a pink model housed in a water-filled torso shown by yellow lines.

2.2.3 Liver Phantom

The liver phantom is designed as a combination of a half-cylinder and a trapezoid as shown in figure 2. The major axis of the liver measures 17 cm and the minor axis measures 15 cm. The liver tissue material is modeled on the tissue composition defined in ICRU Report 46 [21], as shown in table 1. Non-uniform iron distribution is modeled as two spherical lesions of 3 cm diameter with concentrations of 5 mg/g and 3 mg/g (wet). These concentration values correspond to iron concentrations reported clinically in liver iron overload in humans. The liver sample is placed inside a simulated torso modeled as an ellipse with 30 cm major axis and 25 cm minor axis. The torso is filled with water to mimic the elastic scattering properties of tissue. Finally, a spine is modeled as a cylindrical tube with 5 cm outer diameter and 1 cm inner diameter, with material definition of skeletal bone tissue from ICRU Report 46 [21] as shown in table 2. The spine provides a dense anatomic structure that can cast a shadow on the iron lesions in certain projections and therefore potentially affect the reconstructed image.
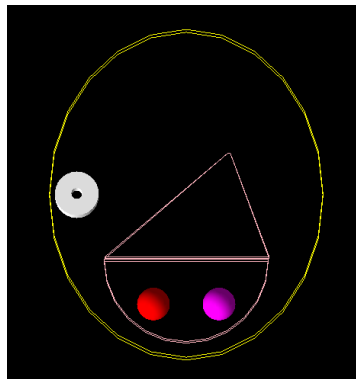

Figure 2. Simulated liver-torso phantom with non-uniform iron overload. The torso is shown as a yellow outline. The liver is shown as a pink outline measuring 17 cm major axis and 15 cm minor axis, and contains two spherical lesions 3 cm in diameter with high iron concentrations – red lesion (5 mg/g) and pink lesion (3 mg/g). The spine is modeled as a white cylindrical tube.

Element	O	C	H	N	P	S	K	Cl	Na	Fe	Density
Normal (%)	71.6	13.9	10.2	3.0	0.3	0.3	0.3	0.2	0.2	0.0	1060 kg/m^3

Table 1. Elemental composition of human liver tissue (obtained from ICRU report 46 [21]).

Element	O	Ca	C	P	N	H	S	Mg	Na	Fe	Density
Normal (%)	43.5	22.5	15.5	10.3	4.2	3.4	0.3	0.2	0.1	0.0	1920 kg/m^3

Table 2. Elemental composition of human skeletal bone (obtained from ICRU report 46 [21]).

2.3 Tomographic reconstruction

NSECT tomography is performed using the translate-rotate configuration similar to first generation CT scanners, by translating the beam horizontally through the entire sample length, then rotating the beam through a fixed angle and repeating the process. The liver phantom is scanned at 8 angles with 20 spatial steps per angle acquired at 1 cm intervals with the 1 cm neutron beam for a total of 160 projections.

Image reconstruction is performed using the Maximum Likelihood Expectation Maximization (MLEM) algorithm implemented for gamma emission computed tomography [22]. The MLEM algorithm is chosen due to its ability to account for low noise conditions in under-sampled systems and account for non-ideal scanning criteria such as non-uniform sampling and presence of attenuation. Images are reconstructed using the counts in the peak corresponding to ^{56}Fe at 847 keV.

2.4 Statistical Analysis

The reconstructed image is analyzed by testing the average pixel value within each reconstructed lesion against the pixel value in the liver background using a z-score test for difference of means. The z-score test is used to determine the statistical significance of detecting each lesion above the liver background. To calculate the mean pixel value and the standard error in the pixel value within the reconstructed lesions, the entire area corresponding to the original simulated lesion is used. Differences with a two-tailed p-value ≤ 0.05 are considered statistically significant. Results of statistical analysis of the reconstructed image are shown in table 3.

2.5 Dose Calculation

Patient dose in NSECT is a combination of neutron and gamma dose effects. The total delivered dose is calculated by measuring the energy deposited in the liver and surrounding tissue in the GEANT4 simulation, and converting it to equivalent dose as described below. The calculation takes into account three parameters to obtain an accurate estimate of dose: (a) Mass of irradiated tissue, (b) Neutron Q-factor, (c) Liver weighting factor. Each of these values is shown in table 4 in the results of dose calculation. The energy deposited in tissue is measured from the GEANT4 simulation in MeV. The energy in MeV is converted to Joules and divided by the mass of irradiated tissue to obtain the absorbed dose. The absorbed dose is then converted to effective dose by multiplying with the neutron quality factor and liver weighting factor. The calculation can be summarized as:

- Total energy deposited in tissue (from cumulative neutron and gamma effects) $\rightarrow$ Measured (MeV)
- Total energy deposited (J) = Total energy deposited (MeV) x 1.6 x 10^{-13} J/MeV
- Absorbed Dose = Total energy deposited / Mass of irradiated tissue
- Effective Dose Equivalent = Absorbed dose x Neutron Q-factor x Liver weighting factor.

The effective dose is calculated for all projections at 1 angle and multiplied by 8 to obtain the total patient dose from the scan. In this study, the dose is calculated separately for the liver and the surrounding abdominal tissue in order to compensate for the difference in irradiated mass within each region, which affects the calculation of effective dose.

3. RESULTS

Figure 3 shows the reconstructed image for the tomographic scan with 8 angles, reconstructed using the iterative MLEM algorithm with 15 iterations. The reconstructed image is displayed without any ad-hoc normalization or correction. As can be seen, pixel intensity is primarily distributed in regions corresponding to regions of iron in the liver. Each iron lesion appears brighter than the liver and abdomen background. The lesion with higher iron concentration (5 mg/g) appears brighter than the lesion with lower concentration (3 mg/g). The mean pixel values within the 3 regions are measured and found to be: (i) 5 mg/g lesion = 110.58, (ii) 3 mg/g lesion = 40.88, (iii) liver background = 14.98. Table 3

shows a summary of the statistical analysis of the reconstructed image using the z-score test for difference of means. The standard error is calculated using the standard deviation of pixel values and number of pixels within the original simulated lesion. Each lesion is detected above the background with p-value ≤ 0.0001 using the 8-angle scanning geometry.
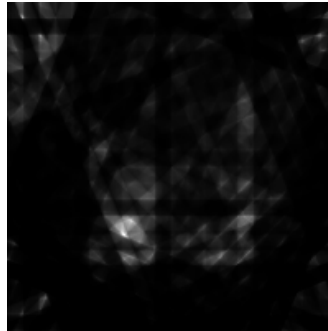

Figure 3. Reconstructed image for the human liver sample. Both lesions are visible above the background and can be detected with p-value ≤ 0.0001.

Region	Mean pixel value	Std. error	z	p-value
5 mg/g	110.58	8.44	11.33	0.0001
3 mg/g	40.88	1.12	23.11	0.0001
Liver BG	14.98	0.04	--	--

Table 3. Summary of statistical analysis of the reconstructed image using a z-score test for difference of means.

Table 4 shows a summary of the dose calculation for the scan. The dose is calculated separately for the liver region and the region corresponding to abdominal tissue by tracking the energy deposited within each individual area. The two regions are treated separately to compensate for the difference in irradiated mass of tissue, which will affect the calculation of effective dose delivered to the organ. For incident neutron energy of 5 MeV, the neutron Q-factor is 10, and the liver weighting factor is 0.05. Using the calculation formula described earlier, the dose delivered to the liver is found to be 0.07 mSv per angle, and dose delivered to the abdomen is found to be 0.02 mSv per angle. The effective dose over the entire mass of illuminated tissue is calculated as a sum of the dose to the liver and abdomen, i.e. 0.09 mSv per angle. The total effective dose delivered to the patient from the NSECT scan with 8 angles using the 6-detector geometry is therefore found to be 0.72 mSv.

Parameter	Liver	Torso
Number of Incident Neutrons	1.07E+08	1.07E+08
Total Energy Deposited (MeV)	3.18E+08	1.43E+08
Total Energy Deposited (J)	5.08E-05	2.29E-05
Mass of Liver (kg)	0.37	0.59
Effective Dose (J/kg) Gy	1.37E-04	3.86E-05
Neutron Q-factor	10	10
Liver RBE	0.05	0.05
Effective Dose Equivalent (1 angle)	0.07 mSv	0.02 mSv
Total Dose Equivalent (8 angles)	0.09 mSv x 8 angles = 0.72 mSv	

Table 4. Effective dose delivered from the 8-angle NSECT tomography scan for the liver.

4. CONCLUSION

This work presents a simulation of the NSECT system for in-vivo diagnosis of non-uniform iron overload in the liver. A simulation of the NSECT system for tomographic acquisition has been designed and used to image non-uniform iron distribution in a liver phantom. An image is reconstructed from an acquisition with only 8 angles over the entire image space, which provides a good example of the severity of under-sampling in NSECT. The image reconstructed using the MLEM algorithm shows a distribution of pixel intensity that agrees with the distribution of iron concentration in the liver phantom. The result demonstrates that NSECT has the ability to image and quantify localized regions of iron concentration in the liver with excellent statistical accuracy and reasonable levels of patient dose. The reconstructed image validates the performance of the tomography technique and demonstrates the efficacy of MLEM in reconstructing images from severely under-sampled acquisitions. Both lesions detected in the image contain clinically relevant concentrations of iron observed in patients with hemochromatosis and transfusional overload. While the size and shapes of the lesions in patients may not be precise or distinct as in the simulation, the simulated model serves to demonstrate proof of principle for detection of non-uniform iron distribution through tomography. The source and detectors designed in the simulation are based on the Van-de-Graaff accelerator and HPGe detectors used in laboratory experiments. The results of this study, therefore, indicate that NSECT has the potential to obtain clinically relevant liver iron measurements using currently available source and detector technology. Patient dose calculated from the NSECT scan is observed to be within reasonable limits compared to other ionizing imaging modalities. For comparison, a typical abdominal radiograph delivers 4 mSv to the patient[23]. The dose analysis performed in this study indicates that it may be possible to increase the neutron flux by as much as a factor of 10 and remain within the dose limits of an abdominal CT exam (10 mSv)[23]. The increased neutron flux can be used to acquire a greater number of angles to improve image resolution and quantification accuracy further.

REFERENCES

[1]   Floyd, C. E., Jr., Bender, J. E., Sharma, A. C., Kapadia, A., Xia, J., Harrawood, B., Tourassi, G. D., Lo, J. Y., Crowell, A. and Howell, C., "Introduction to neutron stimulated emission computed tomography," Phys Med Biol 51(14), 3375-3390 (2006).

[2]   Floyd, C. E., Howell, C. R., Harrawood, B. P., Crowell, A. S., Kapadia, A. J., Macri, R., Xia, J. Q., Pedroni, R., Bowsher, J., Kiser, M. R., Tourassi, G. D., Tornow, W. and Walter, R., "Neutron Stimulated Emission Computed Tomography of Stable Isotopes," in Proceedings of SPIE Medical Imaging, 248-254 (2004).

[3]   Kapadia, A. J., Floyd, C. E., Bender, J. E., Howell, C. R., Crowell, A. S. and Kiser, M. R., "Non-invasive quantification of iron 56-Fe in beef liver using neutron stimulated emission computed tomography," in Proceedings of IEEE Nuclear Science Symposium, Medical Imaging Conference, 2232-2234 (2005).

[4]   Kapadia, A. J., Sharma, A. C., Bender, J. E., Tourassi, G. D., Howell, C. R., Crowell, A. S., Kiser, M. R., Harrawood, B. P. and Floyd, C. E., "Neutron Stimulated Emission Computed Tomography for Diagnosis of Breast Cancer," IEEE Trans Nuc Sci (in press), (2008).

[5]   Kapadia, A. J., Sharma, A. C., Tourassi, G. D., Bender, J. E., Crowell, A. S., Kiser, M. R., Howell, C. R. and Floyd, C. E., "Non-Invasive Estimation of Potassium (39K) in Bovine Liver Using Neutron Stimulated Emission Computed Tomography (NSECT)," in Proceedings of IEEE Nuclear Science Symposium, Medical Imaging Conference, 2076-2078 (2006).

[6]   Powell, L., "Hemochromatosis," in [Harrison's Principles of Internal Medicine], edited by D. Kasper, Fawci, AS, Longo, DL, Braunwald, E, Hauser, SL, Jameson, JL, Vol. 2, pp 2298-2303, McGraw Hill, NY, (2005).

[7]   Chezmar, J. L., Nelson, R. C., Malko, J. A. and Bernardino, M. E., "Hepatic iron overload: diagnosis and quantification by noninvasive imaging," Gastrointest Radiol 15(1), 27-31 (1990).

[8]   Andrasi, E., Farkas, E., Scheibler, H., Reffy, A. and Bezur, L., "Al, Zn, Cu, Mn and Fe levels in brain in Alzheimer's disease," Arch Gerontol Geriatr 21(1), 89-97 (1995).

[9]   Bomboi, G., Marchione, F., Sepe-Monti, M., De Carolis, A., Bianchi, V., Medda, E., Pino, A., Bocca, B., Forte, G., D'Ippolito, C. and Giubilei, F., "Correlation between metal ions and clinical findings in subjects affected by Alzheimer's disease," Ann Ist Super Sanita 41(2), 205-212 (2005).

[10]   Garg, A., V. Singh, et al., "An elemental correlation study in cancerous and normal breast tissue with successive clinical stages by neutron activation analysis," Biological Trace Element Research 46, 185-202 (1994).

[11]   Geraki, K. and Farquharson, M., "Concentrations of Fe, Cu and Zn in breast tissue: a synchrotron XRF study," Phys. Med. Biol 47, 2327-2339 (2002).

[12]   Ng, K. H., Bradley, D.A., Looi, L.M., Seman Mahmood, C., Khalik Wood, A., "Differentiation of elemental composition of normal and malignant breast tissue by instrumental neutron activation analysis," Appl. Radiat. Isot. 44(3), 511-516 (1993).

[13]   Yaman, M., Atici, D., Bakirdere, S. and Akdeniz, I., "Comparison of trace metal concentrations in malign and benign human prostate," J. Med. Chem. 48, 630-634 (2005).

[14]   Civit, T., Houdayer, A. J. and Kennedy, G., "A search for trace elements in some human intracranial tumors by instrumental neutron activation analysis," Biol Trace Elem Res 74(3), 203-210 (2000).

[15]   el-Yazigi, A., Al-Saleh, I. and Al-Mefty, O., "Concentrations of zinc, iron, molybdenum, arsenic, and lithium in cerebrospinal fluid of patients with brain tumors," Clin Chem 32(12), 2187-2190 (1986).

[16]   Yoshida, D., Ikeda, Y. and Nakazawa, S., "Quantitative analysis of copper, zinc and copper/zinc ratio in selected human brain tumors," J Neurooncol 16(2), 109-115 (1993).

[17]   Powell, L. W., "Diagnosis of hemochromatosis," Semin Gastrointest Dis 13(2), 80-88 (2002).

[18]   Powell, L. W., George, D. K., McDonnell, S. M. and Kowdley, K. V., "Diagnosis of hemochromatosis," Ann Intern Med 129(11), 925-931 (1998).

[19]   Kapadia, A. J., Tourassi, G. D., Sharma, A. C., Crowell, A. S., Kiser, M. R. and Howell, C. R., "Experimental detection of iron overload in liver through neutron stimulated emission spectroscopy," Phys Med Biol (in review), (2008).

[20]   Ivanchenko, V. N., "Geant4 toolkit for simulation of HEP experiments," Nuclear Instruments and Methods in Physics Research Section A 502(2-3), 666-668 (2003).

[21]   International Commission on Radiation Units and Measurements, [Photon, electron, proton and neutron interaction data for body tissues.], 46, Bethesda, MD, 1992.

[22]   Lange, K. and Carson, R., "EM reconstruction Algorithms for Emission and Transmission Tomography," Journal of Computer Assisted Tomography 8(2), 306-316 (1984).

[23]   RSNA, [Radiation Exposure in X-ray Examinations], Available at: http://www.radiologyinfo.org, Last Accessed: (2007).

Validation of a GEANT4 Simulation of Neutron Stimulated Emission Computed Tomography

Anuj J. Kapadia[a], Brian P. Harrawood[a], Georgia D. Tourassi[a,b]
[a]Duke Advanced Imaging Laboratories, Duke University Medical Center, Durham, NC 27705;
[b]Department of Medical Physics, Duke University, Durham, NC 27705

ABSTRACT

Neutron stimulated emission computed tomography (NSECT) is being proposed as a non-invasive technique to detect concentrations of elements in the body for diagnosis of liver iron overload. Several experiments have been conducted to investigate NSECT's ability to determine iron concentration in liver tissue and evaluate the accuracy and sensitivity of the system. While these experiments have been successful in demonstrating NSECT's capability of quantifying iron and other tissue elements in-vivo, they have been prohibitively time consuming, often requiring as much as 24 hour acquisitions for accurate quantification. Such extensive scan times limit the use of the experimental system for initial feasibility testing and optimization. As a practical alternative, GEANT4 simulations are being developed to investigate system optimization and aid further progress of the experimental technique. This work presents results of a validation study comparing the results of a GEANT4 simulation with experimental data obtained from a sample of iron. A simulation of the NSECT system is implemented in GEANT4 and used to acquire a spectrum from a simulated iron sample. Scanning is performed with a 7.5 MeV neutron beam to stimulate gamma emission from iron nuclei. The resulting gamma spectrum is acquired and reconstructed using high-purity germanium (HPGe) detectors and analyzed for energy peaks corresponding to iron. The simulated spectrum is compared with a corresponding experimental spectrum acquired with an identical source-detector-sample configuration. Five peaks are detected corresponding to gamma transitions from iron in both spectra with relative errors ranging from 4.5% to 17% for different peaks. The result validates the GEANT4 simulation as a feasible alternative to perform simulated NSECT experiments using only computational resources.

Keywords: Neutron, Spectroscopy, Gamma, Iron-overload, NSECT, Tomography, Simulation, GEANT4.

1. INTRODUCTION

Neutron stimulated emission computed tomography (NSECT) system is being developed as a technique for non-invasive quantification of elements in the human body [1-5]. It uses inelastic scattering interactions between incident neutrons and target element nuclei to determine the element's spatial distribution and concentration in the body.

NSECT uses the following principle. An incident neutron undergoes inelastic scattering with a target atomic nucleus and excites the nucleus to a higher energy level. The excited nucleus spontaneously decays to a lower energy level and emits characteristic gamma radiation with energy unique to the emitting isotope. Measurement of emitted gamma energy and flux can be used to determine the identity and concentration of the emitting element in the sample. A tomographic image of the element distribution can be created by translation and rotation of the sample.

Such quantitative imaging can be applied for diagnosis of several element related disorders in the human body that are characterized by differences in element concentration between normal and diseased tissue. For example, element concentration differences have been observed in liver iron overload [6, 7], Alzheimer's disease [8, 9], and several cancers including breast [10-12], prostate[13] and brain [14-16]. Detection and quantification of elements can be used to diagnose and monitor these disorders in very early stages.

Several experiments have been performed to investigate NSECT's feasibility in detecting elements in biological tissue[3, 5]. While many of these experiments have been largely successful, they have been prohibitively time consuming. For example, a typical scan to detect iron in the liver requires up to 24 hours of data acquisition. Such extensive scan times deem the experimental system impractical for use during initial feasibility testing and system optimization. System optimization involves simultaneous analysis of several variable acquisition parameters such as neutron flux, number of

gamma detectors and size of neutron beam. It is impractical to investigate the effect of each of these variables with the physical experimental system due to the prohibitively long scan times involved. Therefore, GEANT4 simulations are being developed as an alternative for NSECT development and optimization without the need for specialized sources and gamma detection hardware. Before a GEANT4 simulation can be used to perform iron overload detection studies, it is important to validate the simulated model against experimentally acquired data. This study presents results from a validation experiment for a GEANT4 simulation of NSECT using a natural iron sample containing ^{56}Fe.

2. METHODOLOGY

A simulation of a clinical NSECT system has been developed in GEANT4, a Monte-Carlo programming toolkit that models high-energy physics interactions between particles and matter over a broad range of energies[17]. GEANT4 is developed and managed by a worldwide collaboration of over 100 scientists in Europe, Russia, Japan, Canada and the United States. It allows precise modeling of interactions between neutrons and a variety of target nuclei at energies of relevance to NSECT. The GEANT4 object-oriented programming package includes a powerful set of random number generators, physics units and constants, and provides all the tools required for detector simulation including geometry, tracking and detector response management.

2.1 Simulated Model

The simulated model of the NSECT system contains a mono-energetic neutron source, two high-purity germanium (HPGe) gamma-ray detectors, and a sample of natural iron for validation studies. The model is based on the experimental system which uses a Van-de-Graaff accelerator, HPGe gamma detectors and a tomographic gantry for sample positioning[1, 2].

The simulated neutron source is defined as a mono-energetic neutron gun emitting 7.5 MeV neutrons. The gun is placed at an orientation which ensures that every neutron is incident on the target sample. Neutrons at 7.5 MeV are sufficient to excite several energy states in most elements in the body that are of interest to NSECT. For example, a 7.5 MeV neutron can excite carbon at 4.4 MeV, oxygen at 6.1 MeV and several states in iron at 847 keV, 1039 keV, 1238 keV and 1811 keV.

A detector system with two gamma-ray detectors is used in this simulation study. Each of the two gamma detectors is defined as a solid cylinder of HPGe (100% Ge, density= 5.32 g/cm^3) measuring 10 cm in diameter and 9 cm in height and located at ±135 degrees with respect to the incident neutron beam. The ±135 degree locations correspond to regions of maximum gamma emission around the sample from electric quadrupole interactions, which are expected to be dominant at this neutron energy. The detector material is sensitized to record the energy of inelastic scatter gamma-rays that are incident on each detector volume.
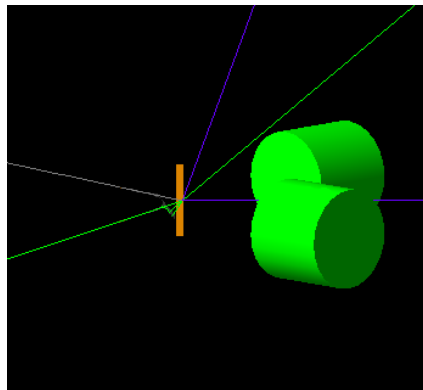

Figure 1. GEANT4 simulation of the NSECT acquisition system. The iron sample is shown in orange with gamma detectors shown as green cylinders. Neutrons enter the system from the right side of the image (blue line). Emitted gamma-rays are shown as green lines while scattered neutrons are seen as blue lines going away from the sample.

The sample in this validation experiment is created as a 3mm thick disc of natural iron containing the three most abundantly found stable isotopes of iron. The circular disc has a 10 cm diameter and 3 mm thickness, natural iron density of 7874 kg/m³, and contains three isotopes of iron in naturally occurring quantities, ^{54}Fe (5.8%), ^{56}Fe (91.75%) and ^{57}Fe (2.45%).

Figure 1 shows the execution of the GEANT4 simulation. The iron sample is shown in orange and gamma detectors are shown as green cylinders. Neutrons enter the system from the right side of the image between the two detectors (depicted by blue lines). Gamma-rays emitted as a result of inelastic scatter are depicted by green lines while scattered neutrons are seen as blue lines going away from the sample. A spectrum is generated from the simulated sample by plotting the gamma counts observed in both detectors vs. the gamma energy.

2.2 Experimental Acquisition

A metallic disc of natural iron is scanned with the laboratory NSECT system, which uses a Van-de-Graaff accelerator source, high-purity germanium gamma-ray detectors, and a tomographic gantry to accommodate the sample[1, 2, 4]. Scanning is performed with a 7.5 MeV neutron beam collimated to 1 cm. Two HPGe gamma-ray detectors (with 0.1% energy resolution) located at ± 135 degrees are used to acquire the emitted gamma-rays. An energy spectrum of the gamma emission is generated with a resolution of approximately 1 keV per detector channel. Background correction is performed using the time-of-flight (TOF) correction technique for NSECT[18], where the background noise spectrum is acquired simultaneously and subtracted from the foreground iron signal. The noise-corrected spectrum from natural iron is used for validation of the NSECT system simulated in GEANT4.

2.3 Spectral Analysis

Spectral analysis is performed by comparing the simulated and experimental spectra using three criteria: (a) Gamma energy peaks in the simulated spectrum must be observed at energies corresponding to prominent excited state transitions in the target nuclei, (b) Locations of peaks in the simulated spectrum must be in agreement with peak locations in the experimental spectrum, and (c) Number of counts in the peaks must be within reasonable limits of each other.

3. RESULTS

Figure 2 and figure 3 show the simulated and experimental spectrum, respectively, from the sample of natural iron. Both spectra show gamma energy peaks for each of the 4 prominent transitions from ^{56}Fe expected at this neutron energy (847 keV, 1039 keV, 1238 keV and 1811 keV), and from one transition in ^{54}Fe (1406 keV). The simulated spectrum shows several peaks corresponding to germanium in the detectors (e.g. 834 keV), which are absent in the experimental spectrum due to TOF background correction.

Figure 4 shows the experimental and simulated spectra normalized and overlaid on one another for comparison. As can be seen, the locations and heights of all five gamma energy peaks from iron are in general agreement with each other. Table 1 shows a summary of the differences observed between the two spectra.

Element	Energy (keV)	Simulated counts (Normalized)	Experimental counts (Normalized)	Difference (%)
^{56}Fe	847 keV	1.000	1.000	0.00%
^{56}Fe	1039 keV	0.098	0.088	11.61%
^{56}Fe	1238 keV	0.281	0.309	9.15%
^{54}Fe	1406 keV	0.037	0.045	16.95%
^{56}Fe	1811 keV	0.083	0.045	4.50%

Table 1. Analysis of the simulated and experimental gamma spectra for the natural iron sample. Peaks for 5 energy transitions in ^{56}Fe and ^{54}Fe are seen in both spectra. The percent difference in the peak at 1406 keV can be attributed to poor statistics due to the low concentration of ^{54}Fe in the sample.

All energy peaks except the peak at 1406 keV are within 15% of the corresponding peak heights in the experimental spectrum. The discrepancy in the 1406 keV peak can be attributed to poor statistics due to the low concentration of the ^{54}Fe isotope in the sample (5.8%). Two energy peaks at 1238 keV and 1811 keV are within 10% of each other. The result suggests that the gamma lines at 847 keV, 1238 keV and 1811 keV may be suitable for quantification experiments.
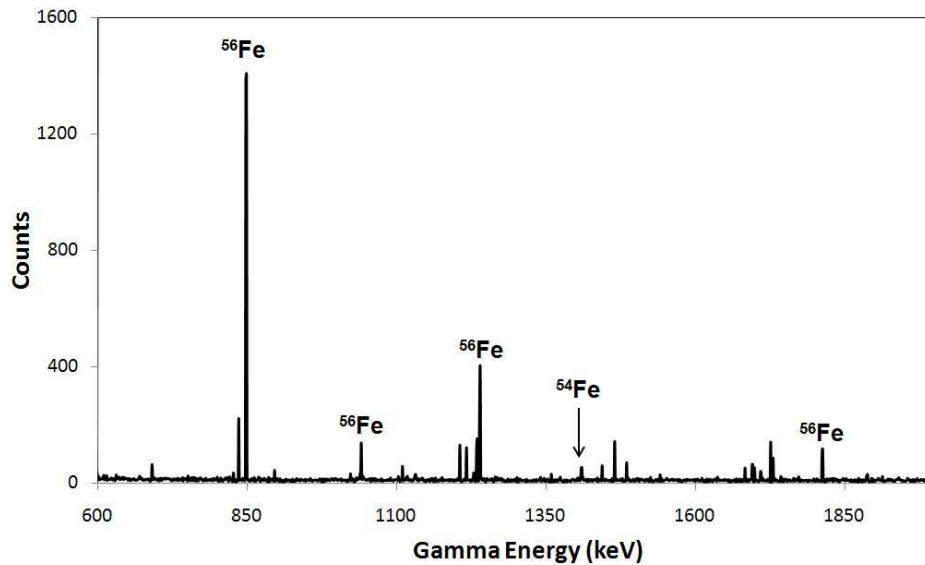
Simulated Spectrum from Iron Sample

Figure 2. Simulated gamma spectrum for a natural iron sample. Energy peaks corresponding to energy transitions from ^{56}Fe can be seen at 847 keV, 1039 keV, 1238 keV and 1811 keV and from ^{54}Fe at 1406 keV. Peaks are also seen for several excited states in germanium, which originate from neutrons scattering onto the HPGe gamma detectors.
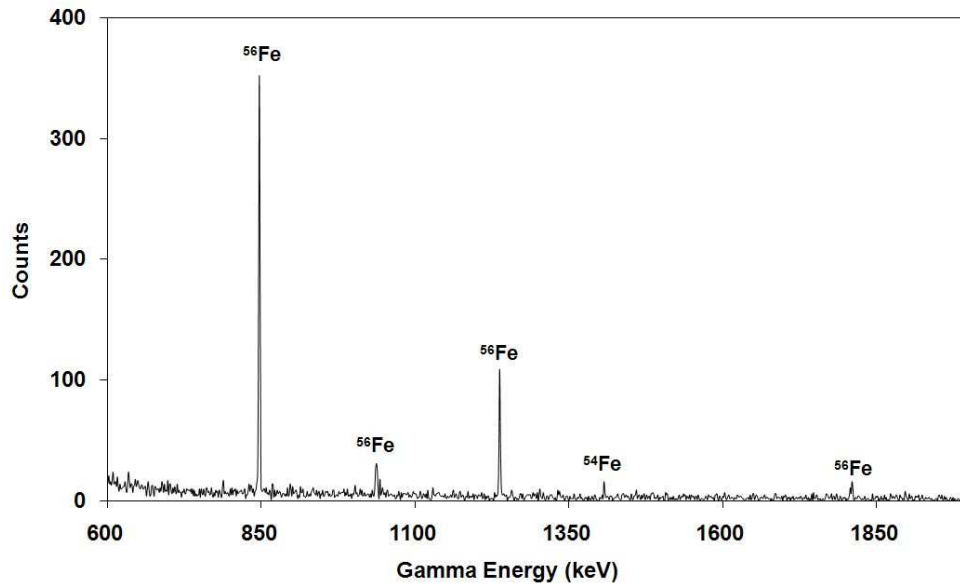
Experimental Spectrum from Iron Sample

Figure 3. Experimental gamma spectrum for the natural iron sample. Energy peaks are seen from ^{56}Fe at 847 keV, 1039 keV, 1238 keV and 1811 keV, and from ^{54}Fe at 1406 keV. Peaks from germanium are absent in this spectrum due to TOF background correction.
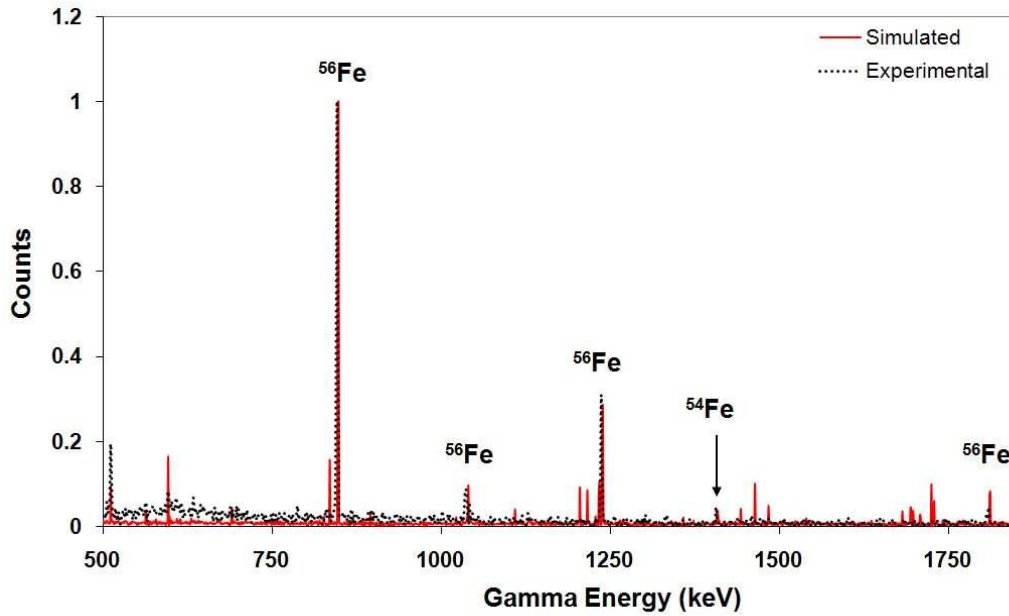
Figure 4. Comparison of simulated and experimental gamma spectra for a natural iron sample. The simulated spectrum is shown as a solid red line, while the experimental spectrum is depicted by an overlaid dotted black line. Energy peaks from all 5 energy transitions in Fe are in excellent agreement with each other. Non-matching energy peaks in the simulated spectrum are due to neutrons scattering onto germanium in the gamma detectors. These peaks are subtracted in the experimental spectrum through TOF background correction.

4. CONCLUSION

This work presents successful validation of a Monte-Carlo simulation of the NSECT system. A simulation of the NSECT system has been designed in GEANT4 and validated using a sample of natural iron. Gamma lines from energy transitions in two isotopes of iron (^{56}Fe and ^{54}Fe) are seen in the simulated and experimental spectra. The energies and counts in the gamma are found to be in excellent agreement with each other, showing errors ranging from 4.5% to 17%. The largest error in the system (17.4% for ^{54}Fe) can be attributed to poor statistics arising from a low isotope concentration in the sample. The result of this study has two important outcomes: (a) It validates the GEANT4 simulation, facilitating its use for future system development and optimization, and (b) It suggests that gamma lines at 847 keV, 1238 keV and 1811 keV may be suitable candidates for investigation in quantification experiments.

REFERENCES

[1]   Floyd, C. E., Jr., Bender, J. E., Sharma, A. C., Kapadia, A., Xia, J., Harrawood, B., Tourassi, G. D., Lo, J. Y., Crowell, A. and Howell, C., "Introduction to neutron stimulated emission computed tomography," Phys Med Biol 51(14), 3375-3390 (2006).

[2]   Floyd, C. E., Howell, C. R., Harrawood, B. P., Crowell, A. S., Kapadia, A. J., Macri, R., Xia, J. Q., Pedroni, R., Bowsher, J., Kiser, M. R., Tourassi, G. D., Tornow, W. and Walter, R., "Neutron Stimulated Emission Computed Tomography of Stable Isotopes," in Proceedings of SPIE Medical Imaging, 248-254 (2004).

[3]   Kapadia, A. J., Floyd, C. E., Bender, J. E., Howell, C. R., Crowell, A. S. and Kiser, M. R., "Non-invasive quantification of iron 56-Fe in beef liver using neutron stimulated emission computed tomography," in Proceedings of IEEE Nuclear Science Symposium, Medical Imaging Conference, 2232-2234 (2005).

[4]   Kapadia, A. J., Sharma, A. C., Bender, J. E., Tourassi, G. D., Howell, C. R., Crowell, A. S., Kiser, M. R., Harrawood, B. P. and Floyd, C. E., "Neutron Stimulated Emission Computed Tomography for Diagnosis of Breast Cancer," IEEE Trans Nuc Sci (in press), (2008).

[5]   Kapadia, A. J., Sharma, A. C., Tourassi, G. D., Bender, J. E., Crowell, A. S., Kiser, M. R., Howell, C. R. and Floyd, C. E., "Non-Invasive Estimation of Potassium (39K) in Bovine Liver Using Neutron Stimulated Emission Computed Tomography (NSECT)," in Proceedings of IEEE Nuclear Science Symposium, Medical Imaging Conference, 2076-2078 (2006).

[6]   Powell, L., "Hemochromatosis," in [Harrison's Principles of Internal Medicine], edited by D. Kasper, Fawci, AS, Longo, DL, Braunwald, E, Hauser, SL, Jameson, JL, Vol. 2, pp 2298-2303, McGraw Hill, NY, (2005).

[7]   Chezmar, J. L., Nelson, R. C., Malko, J. A. and Bernardino, M. E., "Hepatic iron overload: diagnosis and quantification by noninvasive imaging," Gastrointest Radiol 15(1), 27-31 (1990).

[8]   Andrasi, E., Farkas, E., Scheibler, H., Reffy, A. and Bezur, L., "Al, Zn, Cu, Mn and Fe levels in brain in Alzheimer's disease," Arch Gerontol Geriatr 21(1), 89-97 (1995).

[9]   Bomboi, G., Marchione, F., Sepe-Monti, M., De Carolis, A., Bianchi, V., Medda, E., Pino, A., Bocca, B., Forte, G., D'Ippolito, C. and Giubilei, F., "Correlation between metal ions and clinical findings in subjects affected by Alzheimer's disease," Ann Ist Super Sanita 41(2), 205-212 (2005).

[10]   Garg, A., V. Singh, et al., "An elemental correlation study in cancerous and normal breast tissue with successive clinical stages by neutron activation analysis," Biological Trace Element Research 46, 185-202 (1994).

[11]   Geraki, K. and Farquharson, M., "Concentrations of Fe, Cu and Zn in breast tissue: a synchrotron XRF study," Phys. Med. Biol 47, 2327-2339 (2002).

[12]   Ng, K. H., Bradley, D.A., Looi, L.M., Seman Mahmood, C., Khalik Wood, A., "Differentiation of elemental composition of normal and malignant breast tissue by instrumental neutron activation analysis," Appl. Radiat. Isot. 44(3), 511-516 (1993).

[13]   Yaman, M., Atici, D., Bakirdere, S. and Akdeniz, I., "Comparison of trace metal concentrations in malign and benign human prostate," J. Med. Chem. 48, 630-634 (2005).

[14]   Civit, T., Houdayer, A. J. and Kennedy, G., "A search for trace elements in some human intracranial tumors by instrumental neutron activation analysis," Biol Trace Elem Res 74(3), 203-210 (2000).

[15]   el-Yazigi, A., Al-Saleh, I. and Al-Mefty, O., "Concentrations of zinc, iron, molybdenum, arsenic, and lithium in cerebrospinal fluid of patients with brain tumors," Clin Chem 32(12), 2187-2190 (1986).

[16]   Yoshida, D., Ikeda, Y. and Nakazawa, S., "Quantitative analysis of copper, zinc and copper/zinc ratio in selected human brain tumors," J Neurooncol 16(2), 109-115 (1993).

[17]   Ivanchenko, V. N., "Geant4 toolkit for simulation of HEP experiments," Nuclear Instruments and Methods in Physics Research Section A 502(2-3), 666-668 (2003).

[18]   Floyd, C. E., Sharma, A. C., Bender, J. E., Kapadia, A. J., Xia, J. Q., Harrawood, B. P., Tourassi, G. D., Lo, J. Y., Kiser, M. R., Crowell, A. S., Pedroni, R. S., Macri, R. A., Tajima, S. and Howell, C. R., "Neutron Stimulated Emission Computed Tomography: Background Corrections," Nuclear Instruments and Methods in Physics Research Section B 254, 329 - 336 (2007).